Author/s:
Gibson, Bernard Thomas

Title:
Nonlinear acoustic metamaterial for attenuation of low-frequency structure-borne sound in multi-storey timber buildings

Date:
2021

Persistent Link:
https://hdl.handle.net/11343/299797

Nonlinear acoustic metamaterial for attenuation of low-frequency structure-borne sound in multi-storey timber buildings

Bernard Thomas Gibson

ORCID ID: 0000-0002-7934-7538

Doctor of Philosophy

March 2022

The ARC Training Centre for Advanced
Manufacturing of Prefabricated Housing

Department of Infrastructure Engineering

Melbourne School of Engineering and
Information Technology

The University of Melbourne

Submitted in partial fulfilment of the requirements for
the degree of Doctor of Philosophy (Engineering)

Abstract

Construction of multi-storey timber buildings up to eight storeys in height has seen significant growth in recent years due to advancements in timber engineering and associated revisions in construction codes around the world. Despite achieving high standards of acoustic insulation for mid to high frequencies, effective attenuation of frequencies in the 20 – 120 Hz range has remained a longstanding unresolved challenge for multi-storey timber buildings. Propagation of unwanted noise into neighbouring rooms occurs mainly in the form of structure-borne vibrations that ultimately radiate sound into the air. To solve this issue, a successful approach would need to rapidly attenuate broadband low-frequency vibrations in timber building structures without interfering with existing structural capacity or adding large amounts of additional mass. It would also need to be seamlessly integrated within the restricted confines of practical structures.

To tackle this problem, floors are identified as the most significant source of unwanted low-frequency noise due to footfall impacts. Therefore, while the principles underlying the studied designs apply to walls, ceilings and other elements in timber structures, attenuation of impact-induced vibration in floors is identified as the most promising target for improving low-frequency sound insulation in timber buildings.

Born out of a thoroughgoing characterisation of the problem and analysis of the limitations of existing methods, this research investigates the potential for a highly nonlinear vibro-impact-based acoustic metamaterial to attenuate 20 – 120 Hz structure-borne impact sound in lightweight timber floors. The proposed system is investigated experimentally and numerically using a developed and validated hybrid finite element (FE)/rigid body dynamic model, which is shown to be capable of efficiently simulating large metamaterial structures while accounting for the effects of detailed internal resonator parameters.

The proposed nonlinear vibro-impact metamaterial system is found to be capable of rapidly attenuating impact-induced structure-borne sound in the frequency range of interest. This is demonstrated in a small-scale experimental prototype beam and a full-scale numerical model of a timber floor structure. The system adds only a relatively small amount of mass to the timber floor structure (i.e., the host structure) and does not interfere with the structural performance (e.g., strength or stiffness) of the host structure. The results also show that alternative geometric configurations will be necessary if the system is to fit within the confines of a real timber floor. Through parametric modelling using the validated FE model, parameters contributing to increased nonlinearity in the vibration response are found to improve attenuation.

These results demonstrate a potential new approach for dealing with a longstanding issue in multi-storey timber buildings. This is a significant step towards the development and implementation of the proposed solution that would bring about a necessary and significant improvement in building occupant comfort. The results show that it is possible to overcome the limitations of existing approaches using highly nonlinear local resonance effects.

Further research is recommended to assess the potential for alternative geometric configurations to achieve similar results in a practical form factor that will fit within the confines of a real timber floor structure. To achieve the development of a practical solution, this work will need to be extended to consider internal structural effects and resonator placement. The capacity of this type of system to attenuate broadband low-frequency vibration opens the door for a wide range of possible designs capable of

attenuating unwanted broadband vibration in building structures (including those caused by footfall impacts, vibrating machinery, wind, and earthquakes), bridges, pipelines, and aircraft.

Declaration

This is to certify that;

i. the report comprises only my original work,

ii. due acknowledgement has been made in the text to all other material used,

iii. the thesis is fewer than 100,000 words in length, exclusive of tables, maps, bibliographies, and appendices

Bernard Gibson

March 2022

Preface

This thesis is the end result of a long journey with no clear beginning, or perhaps, many beginnings. The topic itself grew from an industry request to investigate noise attenuating, lateral load-bearing intertenancy connections in multi-storey timber buildings. The literature led to the much broader problem of low-frequency structure-borne sound, which has remained an open research problem in timber buildings for over five decades. I'm not sure if it was sheer determination or just plain hubris that ultimately led me to nonlinear metamaterials.

The fields of nonlinear dynamics in general, and nonlinear metamaterials specifically, are highly specialised fields that have remained in the realm of fundamental research to a much larger extent than their linear counterparts. This is due to an extraordinary complexity in observed phenomena that have confounded many of the most powerful standards of analysis. So, to write a thesis on work that attempts to harness some small aspect of that complexity for practical application in a highly practical field like civil construction presents a challenge – firstly, in finding approaches that can generate practically useful results and secondly, in constructing descriptions that are accessible to the field for which it is intended. The goals of this work have been directed towards those purposes.

Most of the work presented in this thesis was originally developed for publication as a series of research papers. To that end, many hours were spent drafting chapters to achieve concise yet comprehensive descriptions of the work, and I am hopeful that that work has paid off in some small way. I am very grateful to my supervisors for their generous editorial assistance and technical guidance along the way. Having said that, while much assistance was received, the writing, modelling and experimental work are my own.

During the development of this work, results from my ongoing investigations suggested that some designs might have the potential for development as a commercial product. A provisional patent application covering certain aspects of the system was therefore prepared and submitted[1]. In the meantime, the submission of papers for publication was put on hold to avoid making disclosures that might jeopardise that process. For that reason, the papers that form the basis for the main body of this thesis are currently unsubmitted. It remains to be seen whether that work will bear fruit as further investigations relating to the development of a full-scale system are needed to confirm its potential.

This project would not have happened without the generous financial assistance of Forrest and Wood Products Australia (FWPA) and The ARC Training Centre for Advanced Manufacturing of Prefabricated Housing (ARC CAMP-H) (Grant ID: IC150100023).

A great many people must be thanked for making this project possible - so many, in fact, that the whole next section is filled with them. But here, I will just mention how grateful I am to live in a society that has afforded me such an extraordinary opportunity to learn and explore so deeply into some tiny fragment of this amazing world.

Bernie Gibson

Melbourne, 16 March 2022

---

[1] Provisional patent application number 2020902689.

Acknowledgements

Throughout the development of this research and the writing of this thesis, I have received a great deal of support and assistance from many people.

I would like to thank my supervisor, Professor Tuan Ngo, for his willingness to back me on this challenging and unconventional path and for his wise guidance that made it possible to find a way to get there in the end.

To my supervisor, Dr Tuan Nguyen, whose tireless support, and advice was so timely and so critical to the success of this project, for his encouragement through tough times, his integrity and friendship.

To Dr David Heath for his fearless insistence in the early days on letting this project evolve according to its own logic and his extraordinary generosity in sticking with me for all this time, even when it was no longer his job.

To Dr Benoit Belleville for his invaluable input with preparing publications and his support throughout this project. To Dr Sina Sinae for his valued support and guidance with modelling and papers. To Dr Tu Le for his generous assistance and additional computing power when it was most needed.

To Dr Steven Linforth for his advice and assistance with high-speed photography. To Dr Rackel San Nicolas and Laura Jukes for kindly sharing their valuable lab space for so long. To Dr Chris Lafferty and Dr Paolo Lavisci at FWPA for their support and assistance with a project for which the returns will likely be longer term than usual.

To Professor James Friend for awakening my love of research, supporting me to follow it and giving me the confidence to take roads less travelled.

To George Barzak for his dogged determination to produce perfect parts despite the toughest of conditions. You are a humble giant.

To Fraser Paxton for his friendship, support, and endless encouragement to believe in myself. Without him, this crazy adventure would never have happened. To Jose Alfano for starting a revolution the day he walked into our office and made the suggestion and for fighting so hard for us to make this possible. And to Hermann for helping to dissolve so many illusions.

To Irene for sharing her home, friendship, and wisdom all these years and for helping to make this possible.

To Mum, Dad, and Lan, for their love, support, and endless generosity that have all made for a very fortunate life. It will never be possible to truly express my gratitude in words. And to Michael, for joining us for the final stages and bringing even more joy and laughter to our lives.

Finally, to my beautiful, wonderful wife, Megs, whose extraordinary patience through so many hours of nonlinear trials and tribulations has made this possible, for her sacrifice, her generosity, and her fantastic dancing.

Contents

Table of figures

List of tables

Chapter 1. Introduction

1.1 Background

In recent decades, changes to building codes worldwide have simplified approval requirements for the construction of multi-storey timber buildings up to 25 metres in height. This has led to a significant increase in the use of timber for multi-storey construction and an increasing interest in research relating to building performance and safety. As a result, it is now possible to engineer multi-storey buildings with world-class levels of acoustic insulation for mid to high frequencies. However, for low frequencies, between 20 and 120 Hz, acoustic insulation has remained an unresolved issue that seriously affects occupant comfort [1, 2]. Figure 1.1 shows two examples of multi-storey timber buildings constructed in recent years.

Figure 1.1 Examples of recently built multi-storey timber apartment buildings in (a) Kajstaden, Sweden and (b) San Diego, California

The most significant mode of low-frequency noise propagation in timber buildings is in the form of structure-borne vibrations resulting from footfall impacts. Footfall impacts excite low frequencies more efficiently in timber floors because they are generally lighter and less stiff than steel and concrete floors. Lower mass leads to less inertial resistance to impact forces and lower stiffness results in less elastic resistance to resulting resonant vibrations. Low-frequency resonant modes are therefore excited more efficiently and vibrate with larger amplitude in response to footfall impacts [3]. Combined, these factors lead to structures that vibrate with a high concentration of energy at frequencies below 120 Hz. Being the largest contributor to the low-frequency sound insulation problem in timber buildings, impact-induced 20 – 120 Hz vibration in floors is therefore focused on in this thesis for its potential to effect positive change.

Acoustic requirements in building codes for multi-storey buildings, including the National Construction Code of Australia (NCC), were primarily developed for concrete and steel constructions and are widely recognised as insufficient for timber buildings [4]. This is largely because they ignore frequencies below 100 Hz. Timber buildings can therefore satisfy current building codes while exhibiting significantly lower perceived acoustic performance than concrete buildings. This is evidenced by widely reported high levels of occupant dissatisfaction [5].

Technologies have been developed to help attenuate structure-borne sound, but their effectiveness is limited at the lowest frequencies. In particular, practical floating floor systems can provide acceptable attenuation down to approximately 120 Hz, and resilient ceiling mounts can be effective down to approximately 60 Hz. However, below the limits of their effectiveness, both floating floors and resilient ceilings can have a detrimental effect due to unwanted resonances, which can lead to an amplification of low frequencies [4, 6]. The difficulty lies in the high levels of stiffness and mass required to reflect low-frequency vibrations and the long distances needed to damp long wavelengths. This has remained an unresolved issue in the academic literature for over five decades [7-10].

An alternative approach for vibration attenuation, employing locally resonant substructures attached to a vibrating host structure, has received significant research attention in recent years. In its simplest form, a single tuned mass damper can efficiently attenuate a very narrow frequency band. With the addition of multiple local resonators, extraordinary effects can be achieved, including negative effective structural properties such as mass density and bulk modulus. Such structures have been referred to as acoustic metamaterials, and these effects have been shown to be useful for the attenuation of targeted low-frequency ranges [11-14]. A key challenge for this approach lies in the achievement of sufficiently broad attenuation bands for practical applications. In linear systems, the mass of resonators governs the breadth of the attenuated frequency band. Resonator mass is, therefore, a limiting factor. A range of approaches for overcoming this limitation is investigated in this thesis.

Several characteristics are important for a system to have the potential to be applied to the problem in a real timber floor system. These include the following:

- The system must be capable of significantly attenuating vibration in the 20 – 120 Hz frequency range.
- Attenuation must be rapid for transient signals.
- The system should add minimal additional weight to the existing host structure.
- It must be effective for small-amplitude vibrations (< 0.1 mm)
- It must not interfere with or limit the structural performance of the host structure.

These characteristics are discussed in more detail in Chapters 2 and 3.

Born of a detailed analysis of the literature on existing attenuation methods and an exploration of techniques from other fields, this research identifies and investigates a novel approach for attenuating low-frequency structure-borne sound in multi-storey timber buildings. The approach employs a system of highly nonlinear, vibro-impact-based resonators to absorb, counteract and dissipate low-frequency vibration energy from the floor structure in a broad range of frequencies (20 – 120 Hz). The system attaches to the host structure in a way that does not limit or interfere with the structure's strength or stiffness. This type of system has been shown to achieve deep attenuation across a very broad band of low frequencies for small-amplitude vibrations using minimal additional mass [15, 16]. In addition to this, vibro-impact oscillators have been shown to be particularly effective for rapid attenuation of transient vibration [17, 18] – a combination of characteristics that makes this type of system uniquely suited as a potential solution to the problem at hand.

To investigate this system: First, several small-scale prototype beam configurations are fabricated and experimentally tested. Then, a numerical model is developed and experimentally validated to efficiently simulate this class of systems. Finally, that model is used to investigate the potential for the approach to be applied to a full-scale structural section of timber floor.

1.2 Research strategy

1.2.1 Research aim

This research aims to identify and investigate a potential solution to attenuate low-frequency structure-borne sound transmission between tenancies in multi-storey timber buildings to achieve occupant comfort.

1.2.2 Research objectives

The research objectives are as follows:

- To characterise the effects of low-frequency impact sound transmission on building occupants and the limitations of existing attenuation approaches.
- To identify a potential alternative approach by which low-frequency structure-borne sound can be effectively attenuated in timber buildings.
- To analyse the effects of parameters that may affect the selected system's performance with respect to its practical applicability to the problem.
- To draw conclusions about the potential applicability of the new approach for solving the stated problem.

1.2.3 Originality of research contribution

The original contributions of this work fall into the following three main categories:

1. The identification of a novel approach for attenuating 20 – 120 Hz structure-borne sound in multi-storey timber buildings based on a detailed analysis of the problem, including:
    a. identification of floors as the most important contributor to the problem
    b. the dynamics of timber floors, noise sources and their interactions,
    c. the capabilities and limitations of existing solutions,
    d. the requirements for a more effective solution, and
    e. the potential for alternative approaches from different fields to meet those requirements.
2. An analysis (both experimental and numerical) of the dynamical response of a potential solution in which the effects of parameters affecting the system's potential for practical application in timber floors are assessed.
3. The development of a technique for efficiently simulating multi-resonator systems with vibro-impacting components.

Previous work on attenuating low frequencies in lightweight floors has focused on a wide range of approaches. The limitations of these are analysed in the literature review. Only a small amount of previous work has investigated the potential for linear metamaterials to attenuate vibrations in floors, and none has investigated nonlinear metamaterials.

The practical demands of the problem include the following key criteria: 1.) wideband attenuation (20 – 120 Hz) of small-amplitude vibrations (< 0.1 mm), 2.) a need for rapid attenuation of transient wave packets, 3.) a need for the system to fit within the confined physical space a timber floor structure, and 4.) a need to keep mass to a minimum. Nonlinear metamaterials broadly, and vibro-impact-based designs specifically, lend themselves to meeting these criteria. The approach selected for investigation has previously been investigated in the context of fundamental research using small-scale prototypes and highly simplified semi-analytical models. However, no work has focused on the applicability of this approach to a real-world problem; and no work has modelled the system's internal dynamics in a way that reveals the effects of parameters essential for the design of real physical systems.

The dynamics of a vibro-impact-based, nonlinear, multi-resonator system presents a unique set of challenges for modelling. In particular, the need to simulate a large number (on the order of hundreds of sub per second) of low-velocity (< 10m/s)[2] impacts at multiple locations within a large structure necessitates a model that can capture transient wavefronts originating from relatively closely spaced locations and exciting a broad range of frequencies. Standard finite element methods offer high accuracy and flexibility but engender impractically long solution times when modelling both rapid sequences of highly nonlinear impacts and high-frequency responses in a large structure. Alternatively,

---

[2] See Chapter 4 for definition of low-velocity impacts

methods for solving systems of nonlinear partial differential equations of motion that approximate the dynamics of such systems offer savings in solution time but require significant simplifications of physical geometry. This limits their ability to assist in the design of real physical systems.

The approach taken in this research is to develop a hybrid model comprising a two-dimensional finite element structure that employs linear, Euler-Bernoulli beam elements and a rigid body resonator component. This enables a highly simplified yet accurate simulation of low-velocity impacts arising from the dynamics of a realistic representation of the physical system. The result is a model that captures the internal dynamics of a multi-resonator metamaterial beam in a fraction of the time of a standard finite element approach. This enables a detailed numerical investigation of parametric effects that afford insights into the potential for the system to be applied in timber floors.

In previous work, the system selected for investigation achieved broadband attenuation by forming an attenuation band between two linear bandgaps caused by nonlinearity in the response. Resonant frequencies of internal substructures determined the upper and lower frequency bounds of the attenuation band, and the degree of nonlinearity determined the depth of the attenuation. The degree of nonlinearity was, in turn, determined by the amplitude of the response. Problematic vibrations, responsible for noise transmission in timber floors in the 20 – 120 Hz range, can exhibit amplitudes smaller than 0.1 mm. Therefore, investigations in this thesis focus on the mechanisms by which the nonlinearity can be increased for small-amplitude vibrations. Both experimental and numerical analyses are carried out in which parameters that could have a potential effect in this area are varied. No previous work has investigated the effects of these parameters in this type of nonlinear resonator.

1.2.4 Scope and limitations

The focus of this work is to develop a multi-resonator system approach for the attenuation of low-frequency structure-borne sound in a timber floor system with a view to improving sound insulation performance in timber buildings. While the ultimate goal of the research is to improve the structure-borne sound performance of timber buildings, the highly nonlinear nature of the investigated resonator system combined with the complexity involved in modelling the structural-acoustic performance of timber floors necessitated a carefully focused approach. The modelling presented in this thesis is, therefore, designed to investigate vibration reduction in a simplified structure that can be achieved by applying specific treatments. It does not seek to predict sound radiation due to fluid-structure interaction, nor does it attempt to simulate the intricacies of real floor structures and their flanking pathways. Further to this, and for the same reason, the model limits itself to two-dimensional linear beam elements. This simplified objective eliminates significant complexity while maintaining an ability to meaningfully assess the effects of highly nonlinear resonator designs on the transverse vibration of structures that approximate the mass and stiffness of real floor sections. The underlying assumption upon which this simplification is based is that the vibration response of a narrow section of the floor structure itself is a reasonable predictor of the sound power radiated to the air of adjacent rooms via both direct and flanking pathways. While limiting the certainty of predictions, this assumption is considered reasonable as a basis for valuable insights into the effectiveness of design variations. These constraints were considered necessary to enable the development of a practically achievable model that offered valuable insights in the time available.

The work is directed towards practical outcomes that might ultimately be useful for assisting with floor design in the construction industry. It therefore focuses on improvements in the attenuation of transverse vibration of beams in the 20 – 120 Hz frequency range. While previous research relating to the investigated approach considers the mathematics of complex nonlinear dynamics and chaotic behaviour, those analyses are considered beyond the scope of this work. Similarly, metamaterial analysis techniques directed towards the generation of band structures for systems of infinite extent are also considered beyond the scope of this work as they have limited value for finite, nonlinear, low-frequency systems.

The work is multi-disciplinary by necessity since it seeks to investigate approaches from disparate fields, evaluate them for their potential application to the problem, and investigate them in the context of civil construction. Previous research is, therefore, considered in this context. Related fields may be touched on in the literature but not comprehensively covered if they do not directly relate to a potential practical application to the problem. Where possible, the author has sought to direct the reader to more detailed information on specific topics.

1.3 Summary of chapters

This section summarises the structure of the remainder of this thesis with a brief outline of the content of each chapter. A flow chart showing the sequence of the chapters and their key contributions is shown in Figure 1.2.

Chapter 2 comprises a literature review which is divided into two main parts: the first attends to previous work undertaken in the realm of low-frequency structure-borne sound attenuation in timber floors. It considers the effects of low-frequency impact sound transmission on building occupants and describes the limitations associated with existing methods of attenuation and the work done to overcome these. The second part appraises research on acoustic metamaterials broadly before focusing on nonlinear, vibro-impact-

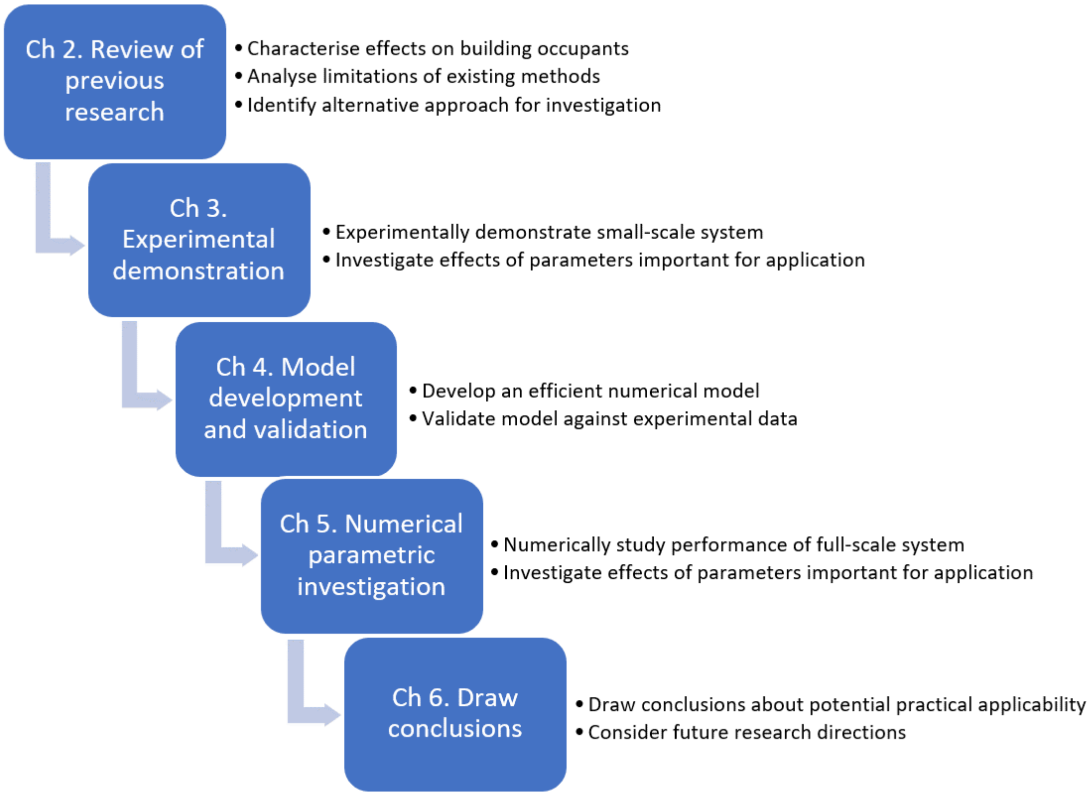

Figure 1.2 Flow chart showing the sequence of the chapters that follow with a summary of their key contributions

based metamaterials specifically. All work is considered in relation to its potential application for the attenuation of low-frequency structure-borne sound. The section describes limitations associated with linear metamaterial approaches for sound attenuation in lightweight floors and approaches for overcoming these limitations. Finally, techniques employing nonlinearity that offer significant advantages for practical application are described.

Chapter 3 describes an experimental investigation into the attenuation effects of the developed vibro-impact-based nonlinear resonators attached to a host beam – referred to in combination as a 'metabeam'. Several five-resonator metabeam configurations are tested. The response of each configuration is compared with that of a corresponding reference beam in which lumped masses replace the nonlinear resonators to ensure that measured attenuation effects are due to the dynamic activity of resonators and not simply to the addition of mass. Three key resonator parameters are investigated, including impact driving amplitude, impact gap size and magnetic spring stiffness. These parameters are considered critical to the generation of nonlinearity for low amplitude vibrations. Time series, frequency spectra and log-scale attenuation characteristics are assessed, and parameter combinations that produce high levels of attenuation across the frequency range of interest are identified.

Chapter 4 describes the development and validation of a numerical model for transient simulation of a multi-resonator, nonlinear metamaterial beam. The approach implements a hybrid model comprising a two-dimensional finite element structure that employs linear, Euler-Bernoulli beam elements and a rigid body resonator component. This enables a highly simplified yet accurate simulation of low-velocity impacts. To validate the model, a combination of experimental data from previous research, a high-resolution finite element model developed in COMSOL, and experimental data from Chapter 3 are used. The model is progressively built up and validated in a step-by-step process until the whole structure of the system is implemented. The model shows a high level of correlation with experimental results for the highest input levels. It is therefore considered acceptable for use in the study conducted in the next chapter, where responses to higher input levels are investigated.

Using the model developed in Chapter 4, Chapter 5 describes a numerical analysis of a full-scale 6 m long by 600 mm wide structural section of timber floor. Effects of the mass, rotational inertia, and height of resonator assemblies are investigated as well as the mass of the suspended resonator magnet and the stiffness of the magnetic spring. These parameters are considered important for their effects on model scaling and the degree of nonlinearity generated in the response. The results show a promising level of attenuation covering several resonant modes across the frequency range of interest and suggest that further work is needed to examine the effects of different boundary conditions, model scaling and geometric configurations.

In Chapter 6, the work is reviewed, conclusions are drawn, and future work is considered. To achieve the goal of implementing a functional system for timber floors, future work might explore alternative geometric resonator configurations that enable high performing resonators to fit within the confines of a practical floor structure. It is concluded that, with further development, the investigated system has the potential to serve as an effective method for attenuating low-frequency structure-borne sound in timber buildings.

Chapter 2. Literature review

2.1 Introduction

In recent years, advances in timber prefabrication, combined with an associated evolution in building codes, have led to a significant expansion of multi-storey timber construction. This has intensified the need for improved inter-tenancy acoustic insulation. A challenge for timber buildings lies in their propensity to propagate low-frequency (20 – 120 Hz) structure-borne sound. Being lighter and less stiff than steel and concrete, timber structures tend to offer less inertial and elastic resistance to impact forces. Effective for higher frequencies, existing sound insulation treatments provide inadequate attenuation in the 20 – 120 Hz range. This research, therefore, seeks new approaches in fields far removed from traditional construction. In acoustic metamaterials, previously impossible properties, such as infinite or negative mass density, stiffness, or bulk modulus, have been achieved, opening new possibilities for wave attenuation. This chapter reviews multi-storey timber construction technologies from the perspective of impact sound insulation performance. It provides an overview of the acoustic challenges specific to timber structures, examines the effectiveness and limitations of existing technologies and considers new developments in acoustic metamaterials that may help overcome the most difficult challenges.

Achieving satisfactory acoustic insulation in multi-storey timber buildings has been recognised as a challenging issue for over five decades – particularly for low-frequency (20 – 120 Hz) vibrations that are propagated through the structure of the building (structure-borne sound) as a result of footfall impacts [7-10]. Even at a mildly elevated walking pace, a 70 kg person can produce disturbing levels of sound transmission (see

Figure 2.1) [2, 6, 19]. Combined with a tendency to exhibit lower resonant frequencies, the result is a high concentration of audible vibration at frequencies below 120 Hz.

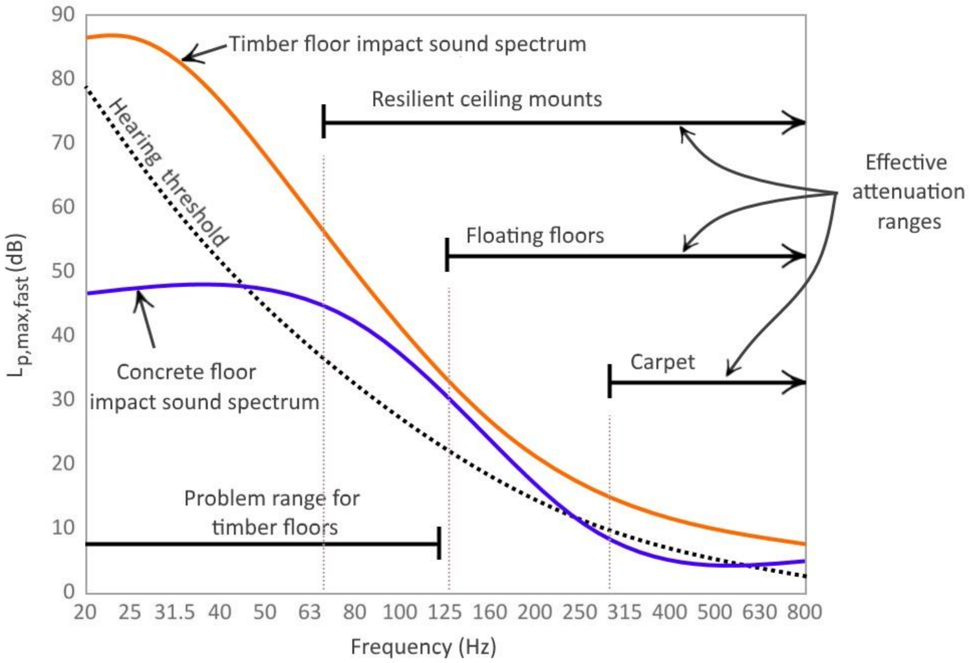

Figure 2.1 Indicative footfall impact-induced frequency spectra produced by a 70 kg man walking in socks at 115 paces per minute for timber and concrete floors, human hearing threshold and effective attenuation frequency ranges for different attenuation technologies. The timber floor was a joisted timber construction with layers of parquet, plasterboard and particle board on top, glulam structural beams and a structurally decoupled ceiling assembly. Based on data from [2, 6, 19]

Building codes for multi-storey buildings generally ignore these frequencies. In the steel and concrete buildings for which codes were developed, they have little effect on occupants' acoustic comfort. For timber buildings, however, ignoring these frequencies leads to major discrepancies between sound transmission ratings and occupant comfort ratings. In fact, by including sub-100 Hz frequencies for impact sound measurements, the calculated transmission rating for a timber building has been shown to increase by 14 – 25 dB [2]. Table 2.1 shows the implications of this finding according to the conservative end of the data presented in that study. This means that timber buildings, rated as acoustically high performing by existing building codes, may not pass even basic standards when frequencies below 100 Hz are considered.

Table 2.1 Sound transmission ratings calculated for timber and concrete floors based on the inclusion of different low-frequency ranges [3]. Higher impact transmission rating reflects poorer sound insulation performance

Lowest frequency included in calculation	Impact transmission rating ($L_{n,T,w}$)	
	Concrete floor	Timber floor
100 Hz	47dB	44dB
50 Hz	48dB	49dB
25 Hz	48dB	54dB
20 Hz	48dB	58dB

Effects of structure-borne sound transmission on occupant comfort are discussed in more detail in Section 2.4. Existing technologies for attenuating timber structure-borne sound have been shown to be inadequate at the lowest frequencies. Floating floor layers can provide good attenuation down to approximately 120 Hz [4]. Resilient ceiling mounts can be effective down to approximately 60 Hz [6]. The difficulty lies in the high levels of stiffness and/or mass required to resist low-frequency vibration inputs, the comparatively low levels of local stiffness required to create impedance discontinuities that reflect low frequencies and the long distances required to damp long wavelengths. This is discussed in more detail in Section 2.5.

In light of these difficulties, this review considers developments in acoustic metamaterials for possible new ways to attenuate low-frequency floor vibrations. Originating in photonic and electronic solid-state physics research, acoustic metamaterials employ dynamic substructures to absorb or redirect wave energy. Behaviours that are impossible in standard materials, such as negative stiffness and mass density, have been used to manipulate wave energy in a wide variety of new ways. Applications of acoustic metamaterials for attenuation of 20 – 120 Hz structure-borne sound are considered in Section 2.6.

This chapter provides a broad overview of issues relating to structure-borne sound transmission in timber buildings. It seeks to give the reader an understanding of the principles that make low-frequency attenuation so important and so difficult to solve. For more comprehensive reviews of literature relating to timber as a material, construction methods and studies that have investigated specific potential solutions, the reader is referred to Ramage et al. (2017) [20], Forssén et al. (2008) [21] and Caniato et al. (2017) [1].

2.2 Multi-story timber acoustics

In this section, consideration is given to the physical mechanisms by which structure-borne sound is excited and propagated through timber buildings. Structure-borne sound is defined as energy propagated as vibrations in the acoustic frequency range (16 Hz –16 kHz) through structural elements of a building [20]. A significant amount of the sound transferred between adjacent rooms is structure-borne. To understand the context in which this contributes to sound transmission in timber buildings, it is of value to consider the following points:

- Footfall induced impacts are the major source of structure-borne sound in timber buildings [1, 21]. Even impacts produced by a slightly elevated walking pace can produce disturbing levels of sound transmission (Figure 2.1) [3, 22, 23].
- Most of the vibration energy induced by footfall impacts on timber floors tends to be in the 20 – 120 Hz frequency range (Figure 2.1) [3].
- Existing sound attenuation measures provide increasingly inadequate attenuation for progressively lower frequencies as they approach 20 Hz (Figure 2.1 and Section 2.5).

- Floating floor systems employing resilient, viscoelastic and particle damping materials for floor topping sub-layers are ineffective (and often actually detrimental) below about 120 Hz unless impractically large cross-sections are used (Section 2.5.4).
- Resilient ceiling mounts become increasingly ineffective below about 60 Hz (Figure 2.1 and Section 2.5.5).
- Active and semi-active damping approaches can be effective for steady-state but significantly less so for transient (impact-induced), low-frequency structure-borne sound (Section 2.5.3).
- Previous reviews have recognised the need for further research on new solutions for low-frequency structure-borne sound transmission in timber buildings [1, 20, 21].

2.2.1 Characteristics of impact sound propagation in structures

To affect building occupants with unwanted sound, vibrations must travel through the building structure until they reach surfaces that are in direct contact with the air of the receiving room. Energy is imparted at the point of impact in the form of a physical deflection, resisted by the structure's inertia (i.e., the mass of material accelerated by the deflection) and elastic stiffness to set it vibrating. In response to an impact excitation, the system will initially exhibit a large vibratory spike. The transient frequencies that initially travel through the structure are governed by the time history of the impact force interaction. It will be seen in section 2.2.4 that, for frequencies below the so-called 'critical frequency' (which will generally include the 20 – 120 Hz range), this initial front of transient waves will not radiate any sound into the air. The system will then vibrate with a spectrum of modal resonant frequencies that are governed by the dimensions of the floor assembly (including those for the entire assembly, as well as spans between individual elements). It is these resonant bending waves that are responsible for the sound radiated into the room. Their amplitude will diminish over a short period of time, according to the damping in the system.

The fundamental frequency is generally governed by the longest span direction. Unique fundamental modes are also associated with other spans within the system (e.g., the span of the subfloor layer between two joists). Aside from the fundamental modes, each span will exhibit a range of higher natural vibration modes. Timber floor systems are commonly designed to exhibit fundamental natural frequencies of between about 8 and 15 Hz. Below 8 Hz, floor vibrations are found to be disturbing to humans (particularly in the range of 4 – 8 Hz) [24]. Natural frequencies above 15 Hz are impractical to achieve in long-span timber floors without excessively deep cross-sections.

2.2.2 Propagation through timber joisted floor systems

The excitation force from a footfall impact has been shown to last for approximately 30 – 100 ms [25]. Bard et al. [26] showed that the energy imparted to the structure during that time depends on footwear, gait frequency, the mass of the walker, and floor coverings. The position of the impact on the floor also influences the energy transmitted to the structure. In general, mid-span impacts, both along and between beams, produce the largest deflections [27-29]. The vibratory energy will then radiate out from the point of impact into the structure. Mass discontinuities in the structure (for example, at junctions between the floor top layer and the joists) affect the transmission of energy. At these locations, some energy is reflected (due to impedance mismatch), some transfers into the connecting element, and some continues along the original member [30, 31]. Reflections increase the distance energy travels before reaching adjacent tenancies, thereby increasing the degree to which it is damped. Importantly, these reflections are also responsible for generating the resonant bending vibrations that cause sound to be radiated into the air (see section 2.2.4).

Energy travelling along the floor's top layer will be partially transferred to each intersecting joist. All energy will continue to travel through the structure until it is either radiated to the air or converted to heat through friction associated with damping. Joists, therefore, act as energy channels. The implication of this is that vibration energy will tend to travel more efficiently towards wall junctions in the direction parallel to the floor joists [32]. Beyond this, the energy will propagate into the floor and walls of the receiving room. The sound that is heard by inhabitants in the receiving room is that which is radiated to the air by resonant vibrations in the wall and floor surfaces that have been excited.

2.2.3 The effect of acoustic bridging across cavity wall-floor junctions

Wall junctions represent another mass discontinuity, where some vibration energy is reflected, some is transmitted into the wall, and some is propagated onward. In the case of continuous flooring or structurally connected floor plates, vibration energy will be propagated across the wall junction into the adjacent room by these material bridges. The amount of energy propagated will be a function of the damping coefficient, mass, stiffness, and geometry of the material bridge(s).

In low-rise timber structures, acoustic bridging can be avoided via structural discontinuity. In taller buildings, structural inter-connection becomes increasingly important for the transfer of wind- and earthquake-induced lateral loads. It is therefore important to understand the impact of acoustic bridging in this context.

Only a limited amount of research has assessed the effect of acoustic bridging across cavity wall-floor junctions in timber buildings. Nightingale & Halliwell [33] showed that the addition of a continuous OSB subfloor across a previously discontinuous cavity wall junction (Figure 2.2) led to a 10 – 15 dB reduction in insulation class effectiveness

(FIIC[3]). However, the addition of an engineered floating floor over the continuous OSB layer improved the impact sound insulation rating by 18 dB. The implication of this is that *lateral* sound transfer *with* structural continuity was no worse than the *vertical* transfer through a fully insulated floor. Structurally continuous floor systems, therefore, do not represent a more significant sound insulation problem than existing vertical insulation systems.

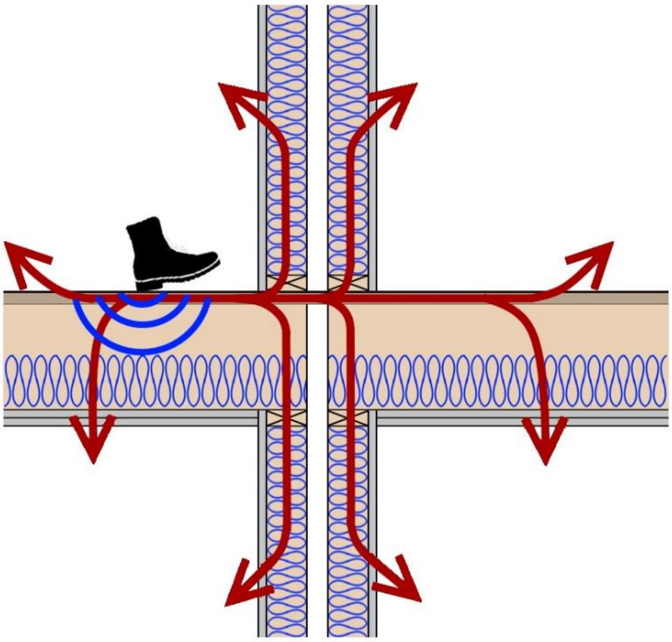

Figure 2.2 Footfall impact-induced structure-borne sound pathways for a multi-story timber wall and floor junction. with a cavity wall and continuous top floor layer

2.2.4 Sound radiation from vibrating structures

The radiation of sound into the air from vibrating building surfaces is dominated by bending waves in the structure. Relative to shear and longitudinal waves, bending waves produce much larger structural motion perpendicular to the vibrating surface and

---

[3] FIIC (field impact insulation class) is the impact sound insulation unit for field measurements used in Canada and the U.S. They are calculated in accordance with ASTM E989 and do not include frequencies below 100Hz. They are related to ISO 717-2-based calculations according to the following equations: $L'_{n,w} = 110 - \text{FIIC}$ and $L_{n,w} = 110 - \text{IIC}$ respectively.

therefore generate much larger pressure variations in the air. Two types of bending wave are to be differentiated with respect to sound radiation: *forced* bending waves are transient travelling waves that result from an applied excitation force, and *resonant* bending waves are standing waves that result from reflections at structural boundaries.

The bending wave speed (c_B) in a plate is frequency-dependent and varies according to the following relation:

$$c_B = 2\pi\left(\frac{B\omega^2}{m}\right)^{\frac{1}{4}} \tag{2.1}$$

where B is the flexural stiffness per unit width, m is the plate mass per unit area, and ω is the angular vibration frequency. The frequency at which the bending wave speed equals the wave speed in air is referred to as the critical frequency, which is given by:

$$f_c = \frac{c^2}{2\pi}\sqrt{\frac{m}{B}} \tag{2.2}$$

where c is the speed of sound in air.

Bending wave frequencies above the critical frequency are radiated into the air from the whole floor plate and with high efficiency. However, frequencies below the critical frequency are radiated with decreasing efficiency for decreasing frequencies. There are two main reasons for this. Firstly, *resonant* waves in this range couple less efficiently with the air due to self-cancelling effects around modal node lines. On either side of a nodal line, the plate surface moves in opposite directions, therefore causing a cancellation of sound pressures in that region. Secondly, *transient* waves below the critical frequency do not radiate sound at all because, due to their wave speed being slower than that in air, they can only excite airborne waves that travel parallel to the plate's surface. This produces a near field acoustic effect only, with no radiation of sound into the room.

The efficiency with which structural bending waves radiated sound into the air is referred to as the radiation efficiency. As has already been seen, the radiation efficiency is close to unity for frequencies above the critical frequency. Conversely, it is low and frequency-dependent for frequencies below the critical frequency. The radiation efficiency (σ) can be used to calculate the sound power (P) radiated to the air according to the following relation:

$$P = P_{forced} + \ P_{resonant} = \rho c S \langle \tilde{v}^2 \rangle \sigma_{forced} + \rho c S \langle \tilde{v}^2 \rangle \sigma_{resonant} \qquad (2.3)$$

where P_{forced} and $P_{resonant}$ are the power radiated due to forced and resonant vibrations, ρ and c are the density of air and speed of sound in air, S is the surface area of the plate, $\tilde{v}$ is the mean square surface velocity perpendicular to the plate's surface, the brackets indicate spatial averaging over the surface, and σ_{forced} and $\sigma_{resonant}$ are the radiation efficiencies for forced and resonant vibrations. A derivation of any of the various methods by which radiation efficiency can be calculated is beyond the scope of this review. For more detailed descriptions, the reader is referred to [34] for a broad overview for simply supported plates and [35] for consideration of the effects of other boundary conditions.

2.3 Codes and standards for impact sound insulation

This section summarises Australian and international codes and standards relevant to impact sound insulation measurement and prediction in buildings. Codes cover the following areas:

- Methods for generating and measuring impact sound in both field and laboratory settings

- Methods for evaluating data collected via standard measurement procedures
- Methods for predicting impact sound performance for building elements
- Maximum acceptable levels of impact sound transmission

2.3.1 Standard methods for *measuring* impact sound insulation

The current international standards for the generation and measurement of impact sound include ISO 16283-2:2020 for field measurements and ISO 10140-3:2021 for laboratory-based measurements. In Australia, AS ISO 140, a standard based on a predecessor to the ISO standards, is still in use. For field measurements, the current code is AS ISO 140.7:2006, and for laboratory measurements, it is 140.8:2006.

Procedures in those standards involve the generation of impacts using a standardised tapping machine placed at multiple locations on the floor of the source room and the measurement of the resulting sound in the source room using a calibrated sound level meter or calibrated microphone connected to an analyser. Figure 2.3 shows a schematic of the basic setup. The tapping machine is a device with five hammers, each weighing 500 g that are sequentially dropped from a height of 40 mm in a 2 Hz cycle for a total impact rate of 10 Hz. For lightweight floors, a modified standard tapping machine is specified in ISO 10140-5. The modification involves the addition of a resilient surface onto the face of the hammers so that lower frequencies are excited more effectively [36] (this is not required in Australian standards because frequencies below 100 Hz are ignored). The procedures are directed towards small to medium rooms (10 – 250 m^2) and, depending on the jurisdiction, account for frequencies in the range of 50 – 5000Hz. Measurements are usually made in one-third octave bands.

The positioning of microphones depends on the frequency range being measured. For higher frequencies for which a diffuse sound field can be assumed (above about 100 Hz

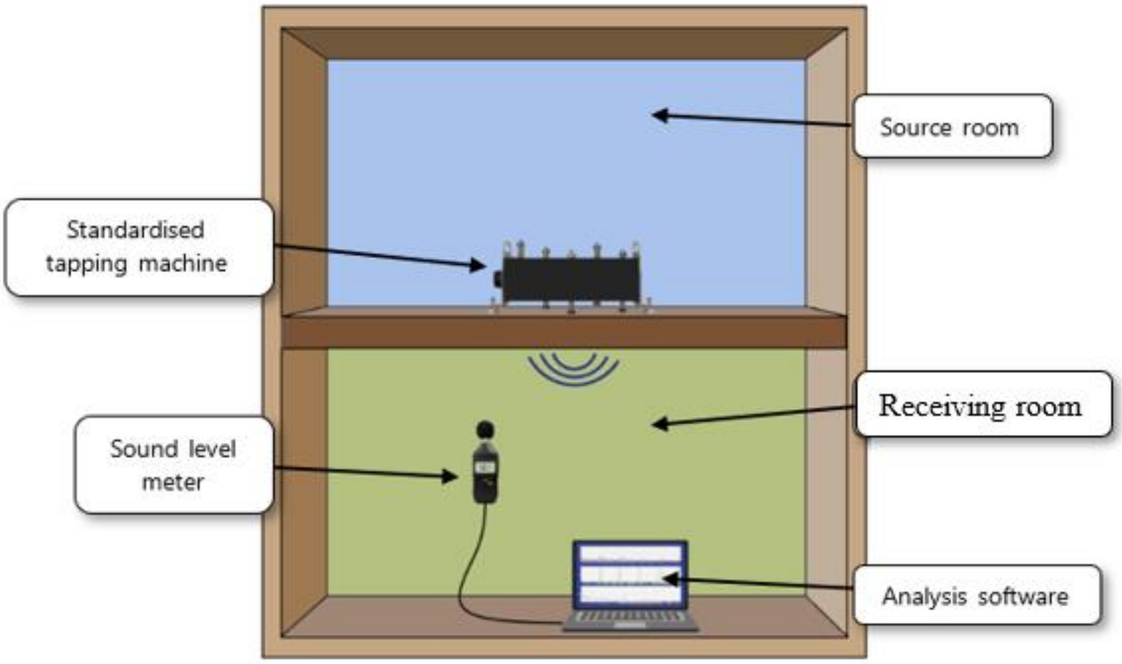

Figure 2.3 Schematic of a basic setup for the measurement of the impact sound performance of a timber floor. The standardised tapping machine is placed at a number of locations on the floor of the source room. Sound level measurements are made in the receiving room at a number of locations which depend on the frequency range being measured.

as a general guide), the average of multiple readings taken at locations around the centre of the room can be used. For low frequencies, fewer modes are present, and large variations in sound pressure can occur around nodal lines through central regions of the receiving room. Microphone positions closer to the corners are therefore specified. The standards also include methods employing a rubber ball as an input source. The rubber ball excites lower frequencies more effectively and better approximates a real footfall [37]; however, at present, no standard exists for calculating single number impact ratings based on rubber ball measurements.

2.3.2 Standard methods for *evaluating* impact sound insulation

Measurement data collected according to standards described in the previous section must be interpreted in a way that provides a consistent estimate of the building's performance with respect to occupant comfort. To do this, a single number rating is usually calculated. Standard methods for evaluating impact sound transmission data in buildings are given in ISO 717:2020. Variations of these methods, in various historical forms, have been adopted into the codes of a wide range of countries. In Australia, the relevant standard is AS ISO 717:2004. However, the optional use of the low-frequency spectrum adaptation term was removed from the Australian Building Code in 2016 at the request of industry. The implications of this, with regard to occupant comfort in timber buildings, are discussed in section 2.4.1.

The general approach of these methods involves evaluating a set of one-third octave band[4] recorded sound pressure levels (L'_i) against a standard curve covering a frequency distribution from 100 to 3125 Hz. The apostrophe indicates in-field measurements, as opposed to those made in a laboratory. In-field measurements tend to be affected by flanking sound which can be controlled in the laboratory. Recorded levels can be ‘normalised’ to account for the presence of absorption surfaces (L'_n), ‘standardised’ to account for reverberation time ($L'_{n,T}$) in the receiving room and ‘weighted’ to account for human sensitivity to different frequencies ($L'_{n,T,w}$).

The standard curve against which recorded levels are evaluated was designed based on data collected from concrete floors, and the results of these calculations have been shown to correlate well with sound intensity as perceived by building occupants [23]. However, as timber came to be increasingly used in the construction of multi-storey buildings, it became apparent that the lower frequency impact response of these structures was leading to a mismatch between the calculated values and the perception of occupants.

To account for this discrepancy, a low-frequency spectrum adaptation ($C_{I,50\text{–}2500}$) term was introduced, which accounts for frequencies between 50 and 100 Hz. The subscript

---

[4] A one-third octave band sound pressure level is the mean sound pressure for a frequency range covering one-third of an octave.

'I' represents the particular frequency weighting curve used in the calculation, and the subscript '50-2500' indicates the frequency range considered for the calculation. Use of this term was made mandatory in Sweden in 1999 and has remained in ISO 717 (including AS ISO 717) as an optional step in calculations. A significant amount of research has gone into understanding the degree to which calculated single number impact sound ratings correlate with occupant perceptions. This research formed the basis for the introduction of the low-frequency spectrum adaptation terms now included in the international standard and will be discussed in section 2.4.1.

2.3.3 Standard methods for *predicting* impact sound insulation

Methods for predicting impact sound insulation between rooms in buildings are provided in ISO 12354-2:2017. Methods are given for predicting single number impact sound insulation performance using equations that account for contributions from the main floor element, floating floor assemblies, and suspended ceilings, as well as effects from flanking transmission. The standard supersedes ISO 15712-2:2005. The main purpose of the revision was to accommodate lightweight building elements and the low frequencies that become important because of them. The new standard still covers frequencies down to 100 Hz but adds a provision (Annexe E) for including frequencies down to 50 Hz [38-40].

In ISO 12354-2:2017, the normalised impact sound insulation rating for a floor system (L'_n) is calculated according to the following equation:

$$L'_n = 10\lg\left(10^{\frac{L_{n,d}}{10}} + \sum_{j=1}^{n} 10^{\frac{L_{n,ij}}{10}}\right) \qquad (2.4)$$

where $L_{n,d}$ represents the contribution from direct transmission through the floor and is calculated by summing the effects of the bare floor structure ($L_{n,situ}$), the floating floor

(ΔL_{situ}), and any additional (ceiling) linings added to the underside of the bare structure ($\Delta L_{d,situ}$) as follows:

$$L_{n,d} = L_{n,situ} - \Delta L_{situ} - \Delta L_{d,situ} \tag{2.5}$$

and each $L_{n,ij}$ term represents the flanking transmission from the separating element) to the flanking element j calculated as follows:

$$L_{n,ij} = L_{n,situ} - \Delta L_{situ} + \frac{R_{i,situ} + R_{j,situ}}{2} - \Delta R_{j,situ} - \overline{\Delta D_{v,ij,situ}} - 10lg\sqrt{\frac{s_i}{s_j}} \tag{2.6}$$

where $R_{i,situ}$ and $R_{j,situ}$ are the airborne sound reduction indices for elements i and j, respectively, $\Delta R_{j,situ}$ is the change in sound reduction index for element j due to additional linings, $\overline{\Delta D_{v,ij,situ}}$ is the mean vibration insulation in the junction between elements i and j and s_i and s_j are the surface areas of element i in the source room and j in the receiving room, respectively. While some equations and input data for common homogenous elements (e.g., monolithic concrete slabs) are provided in the standard, application of this methodology for lightweight timber floors relies heavily on experimentally recorded data for each individual element.

In Annexe E of the standard, information is given on alternative measurement and calculation methods that can be used for predictions in the low-frequency range. These methods are necessitated by the large spatial variation in low-frequency sound pressure levels and the inadequacy of standard methods for measuring or estimating low-frequency vibration reduction at junctions between elements. Alternative standards that account for these issues are suggested for the low-frequency range.

2.3.4 Code requirements for impact sound insulation in different countries

As was discussed earlier, Australian regulations for the calculation of impact sound insulation ratings neither require nor advise the use of a low-frequency spectrum adaptation term. The frequency range that must be included in measurements is 100 – 3150 Hz. The impact sound insulation rating requirement for inter-tenancy partitions in Australian residential buildings is 62dB. The same requirements exist in the U.K. Of 21 other countries in Europe, 19 employ more stringent requirements ranging between 48 and 60 dB and two countries use less stringent requirements (Spain: $L'_{n,T,w} \leq 65$ dB, Italy: $L'_{n,T,w} \leq 63$ dB). The average impact insulation requirement among all European countries is $L_{n,T,w} \leq 56.6$ dB [41]. Table 2.2 shows a list of requirements for European countries.

Table 2.2 Impact sound insulation requirements for European Countries [41]

Country	Descriptor	Multi-storey housing Req. (dB)	Row housing Req. (dB)
Austria	$L'_{n,T,w}$	≤ 48	≤ 43
Belgium	$L'_{n,T,w}$	≤ 58	≤ 50
Czech Rep.	$L'_{n,w}$	≤ 58	≤ 53
Denmark	$L'_{n,w}$	≤ 53	≤ 53
Estonia	$L'_{n,w}$	≤ 53	≤ 53
Finland	$L'_{n,w}$	≤ 53	≤ 53
France	$L'_{n,T,w}$	≤ 58	≤ 58
Germany	$L'_{n,w}$	≤ 53	≤ 48
Hungary	$L'_{n,w}$	≤ 55	≤ 45
Iceland	$L'_{n,w}$	≤ 58	≤ 53
Ireland	$L'_{n,T,w}$	≤ 62	$None$
Italy	$L'_{n,w}$	≤ 63	≤ 63
Latvia	$L'_{n,w}$	≤ 54	≤ 54
Lithuania	$L'_{n,w}$	≤ 53	≤ 53
Norway	$L'_{n,w}$	≤ 53	≤ 53
Poland	$L'_{n,w}$	≤ 58	≤ 53
Portugal	$L'_{n,w}$	≤ 60	≤ 60
Slovakia	$L'_{n,w}$	≤ 58	≤ 58
Slovenia	$L'_{n,w}$	≤ 58	≤ 58
Spain	$L'_{n,T,w}$	≤ 65	≤ 65
Sweden	$L'_{n,w}+C_{I,50\text{-}2500}$	≤ 56	≤ 56
Switzerland	$L'_{n,T,w}+C_I$	≤ 53	≤ 50
U.K.	$L'_{n,T,w}$	≤ 62	$\leq None$

The Canadian building code does not enforce any direct limitation on impact sound transmission levels; however, it recommends that floors achieve an IIC rating of $\geq$ 55 dB (this is approximately equivalent to $L_{n,T,w} \leq$ 55 dB[5]). Also, as of 2015, the Canadian building code requires that flanking sound transmission be accounted for in the calculation of airborne sound transmission ratings. This means that inter-tenancy partitions must now either achieve an airborne sound transmission class (STC) rating of at least 47 dB as measured in accordance with ASTM E413 and E336 or an STC rating of 50 dB in combination with conforming adjoining constructions [42].

In the U.S., the International Code Council-developed International Building Code has been adopted as a base code standard in most jurisdictions. For impact insulation, the code specifies a minimum IIC rating of 50 dB for lab-tested and 45 dB (approximately equivalent to $L_{n,T,w} \leq$ 60 dB and 65 dB respectively) for field-tested assemblies. Testing is to be carried out in accordance with ASTM E492 [43].

2.4 Sound transmission levels and occupant annoyance

To understand the effectiveness of code requirements for ensuring reasonable levels of occupant comfort, it is necessary to assess the relationship between single number insulation performance ratings and occupant perceptions of acoustic performance. A number of socio-acoustic surveys have shown that a very high percentage of people consider acoustic separation between dwellings important [44-46]. Other studies have shown that occupants find footfall noise, in particular, significantly more disturbing than other sources of noise [22, 23] and that impact sound is considerably more annoying in timber buildings than in concrete buildings [47]. However, estimating the correlation

---

[5] See footnote to section 2.2.3 for information about conversion between rating systems

between impact sound transmission levels and occupant annoyance is complicated by several factors.

Our perception of sound depends on the relative intensities of the frequencies it contains (its frequency spectrum). The frequency spectrum produced by an impact will depend on the material, mass and velocity of the impacting object, the type of floor system, its surface hardness, and the qualities of the room into which the sound is radiated. Added to this, the sound level parameter used for comparison is calculated using only a subset of the frequencies contained in the sound (see section 2.3.2). This means that a floor's transmission rating will not only depend on its physical characteristics but also the algorithm used for its calculation. Several studies have investigated the correlation between algorithms used to calculate the impact sound transmission rating and annoyance, with varying conclusions as to which is best. However, as was discussed in the introduction, it has been shown that algorithms that account for low frequencies tend to exhibit a higher correlation with occupant ratings for timber floors [2, 5, 8, 10, 23, 48-50]. This is discussed in more detail later in this section.

Consider, for example, the impact frequency spectra shown in Figure 2.1. These were produced by a 70 kg man, walking in socks at 115 paces/min (an elevated but natural walking pace). Firstly, the shapes of the spectra are affected by footwear. The same person walking in shoes produced lower levels of frequencies below 200 Hz for both concrete and timber floors. Secondly, the transmission rating calculated for those floors using the standard frequency weighting curve and a frequency range of 100 – 2500 Hz was 47 dB for the concrete floor and 44 dB for the timber floor. By including frequencies down to 20 Hz, little effect was had on the concrete floor's transmission rating (increased from 47 dB to 48 dB). However, the timber floor's rating increased from 44 dB to 58 dB (Table

2.1). Further, by using a low-frequency weighting curve that has been shown to more accurately reflect occupant comfort ratings [47, 51], that same timber floor's rating increased to 65 dB [3].

Clearly, a number of factors must be considered when attempting to predict occupant annoyance levels based on impact sound transmission levels. To compare measured sound pressure levels with occupant comfort, Rindel, Løvstad & Klæboe [52] analysed measurements and socio-acoustic survey responses for 600 homes in Norway. Statistically derived dose-response curves were fitted to the data to estimate the relationship between noise levels and the cumulative proportions of occupants experiencing annoyance up to particular levels (Figure 2.4). In the paper, the curve for 'slightly annoyed' was inverted to express the number of people 'satisfied'. The results show that the estimated percentage of satisfied people drops from 85% to 52% as the sound pressure level increases from 45 dB to 55 dB using measurements that include

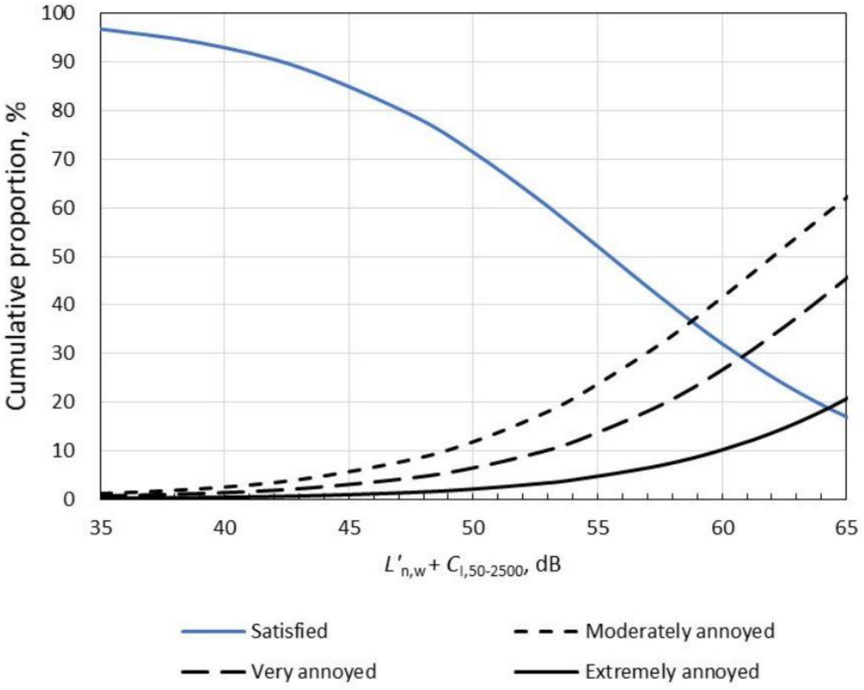

Figure 2.4 Proportion of satisfied occupants and cumulative proportion of annoyed occupants as function of the weighted impact sound pressure level including the low-frequency spectrum adaptation term [52]

frequencies down to 50 Hz. Recall that in Australia, the sound pressure level resulting from structure-borne sound can be as high as 62 dB for measurements ignoring frequencies below 100 Hz. Then, from Table 2.1, it is evident that this is approximately equivalent to 67 dB.

2.4.1 Importance of low frequencies for evaluating impact sound insulation

As has already been mentioned, to predict occupant comfort levels based on impact insulation performance, it is essential to understand the effect of low frequencies on the correlation between single number ratings and occupant reports. A significant amount of research has gone into understanding the degree to which calculated single number impact sound ratings correlate with occupant perceptions. Bodlund (1985) [10] analysed impact sound pressure measurements from 22 different buildings and interviewed over 400 occupants in order to investigate correlations between subjective impressions and single number ratings based on 23 different reference curves. It was found that, by including frequencies down to 50 Hz, correlations were improved by between approximately 2 and 13%. The existing ISO standard curve produced a correlation of 74%, and when extended down to 50 Hz, that increased to 76%. The best correlation (87%) was achieved with a curve having a 1 dB positive gradient between 50 and 1000 Hz followed by a flat gradient up to 3150Hz. A correlation of 84% was also achieved with a flat curve extending between 50 and 3150 Hz.

Hagberg (2010) [48] revisited the data analysed by Bodlund and recognised that the inclusion of horizontal insulation measurements might have decreased the accuracy of curves suggested for the calculation of vertical insulation ratings. By using only vertical measurements from Boland’s data set and then collecting new data from a further ten buildings, the study determined that the best correlation was achieved with a reference curve that had a steep positive gradient between 50 and 100 Hz and a zero gradient thereafter. The correlation achieved with that method was 87%.

More recently, two extensive European projects have specifically investigated the importance of including low-frequency measurements down to 20 Hz for accurately reflecting occupant perceptions of impact sound. Both studies concluded that significantly improved correlations could be achieved by including frequencies in this range [22, 50]. Ljunggren, Simmons & Hagberg [22] showed that the correlation of single number ratings with occupant perceptions was increased by 42% when frequencies between 20 and 50 Hz were included. In that study, occupants also rated footstep noise from neighbours as more than twice as annoying as any other noise source. Reporting findings from the Acuwood project, Hagberg et al. [50] also concluded that frequencies down to 20 Hz should be included in the calculation of single number ratings for timber buildings.

A more detailed study of human perception of frequencies between 20 and 50 Hz was undertaken by Öqvist, Ljunggren & Johnsson [2]. In one study, a binaural listening test in which twenty-four subjects were presented with a series of recordings of footfall induced timber floor impact sounds was carried out. Each recording contained the same impact sound but with different lower frequency cut-off points. Subjects were asked to report differences in perceived annoyance between the pairs of recordings. The results showed that even the 20 – 25 Hz frequency range affected annoyance levels for a significant number of subjects (45% reported a difference). Almost 90% of subjects reported an increased annoyance rating when frequencies down to 20 Hz were added to recordings that contained only frequencies above 50 Hz.

While conclusions from these studies have varied with respect to the exact nature of the reference curve that should be used, a general consensus exists regarding the importance of including frequencies down to 20 Hz if calculated impact sound insulation ratings are to accurately reflect occupant experience. The fact that calculations including frequencies down to 20 Hz correlate more strongly with subjective assessments makes it clear that this range has a significant effect on how occupants perceive impact sound in timber buildings.

2.5 Current approaches for structural-acoustic attenuation

2.5.1 Increasing stiffness and mass

By limiting the degree to which an element deflects in response to an input, vibration energy can effectively be rejected by reflecting it back to the source. For example, if the source were a footfall impact, this would represent a slight increase in the jolt experienced by the person as their foot hits the floor. This limits the amount of energy transmitted into the structure. To achieve this, either the stiffness or the mass of the floor structure must be increased. To increase stiffness, larger structural cross-sections can be employed, which have the adverse effect of increasing the floor-to-floor height in multi-story buildings. Alternatively, stiffer materials (with higher elastic modulus) can be employed. One method that has been used to increase both mass and stiffness of timber floors has been through the structural integration of a layer of concrete with the upper timber floor layer [53]. Acoustic performance of these composite systems has been shown to be effective for frequencies above 100 Hz. However, their performance at lower frequencies has been shown to be inferior to that of a solid concrete floor [6, 54].

2.5.2 Damping

The degree to which energy is dissipated as it propagates through a structure is referred to as damping. Damping is a result of friction which causes vibration energy to be converted to heat. Friction can occur at different scales within the structure:

- Friction between molecules or microstructures within a material is referred to as material damping
- Friction between structural elements is referred to as structural or friction damping.

By increasing the degree of damping in the pathway, vibration energy can be dissipated as heat. This is referred to as passive damping. Three broad approaches can be taken to increase the damping in a structural-acoustic pathway:

- One way is to introduce viscoelastic materials with high damping coefficients into the structural load path. The downside of this approach is that the presence of the damping material in the load path tends to decrease the stiffness of the structure. It has been shown that viscoelastic materials are ineffective (and sometimes even detrimental) for damping frequencies below 120 Hz unless very large cross-sections are employed [55]. Another factor to be considered for viscoelastic material selection is the effect of static compression load on vibration performance. Ljunggren & Ågren (2013) [56] showed that resilient layers tested were more effective in the upper levels of a building where the loads were smaller. Schiavi et al. (2011) [57] investigated this effect in detail for porous resilient materials and proposed an empirical relation between density and airflow resistivity.
- A second approach is to apply damping layers externally to the structure. This can be achieved with the application of an unconstrained layer of damping material to the vibrating structure's surface so that energy is dissipated through cycles of extension

and contraction of the damping material. The added layer may alternatively be constrained by a second, higher stiffness layer added to its outer surface. This leads to energy dissipation through cyclic shear strain in the damping material. Constrained layers can reduce the amount of material that needs to be added, which can be significant for unconstrained layers. This approach avoids the problems associated with decreased structural stiffness but is limited in the depth of attenuation that can be achieved [58].

- A third approach is to attach a damped resonant assembly to the structure in the form of a tuned mass damper. In this case, the structure's response is counteracted by out-of-phase oscillations of the attached mass. For a specific tuned resonance frequency, a relatively large amplitude response in the mass can be damped efficiently. This approach avoids problems associated with decreased structural stiffness but is limited in the width of the frequency band it can attenuate.
- A fourth approach is to increase the distance the sound must travel to reach the receiving destination. In this case, the increased damping will be a function of the damping coefficient of the material used and the length of the element. This approach has obvious implications for the space required by the finished structure.

While not strictly related to structure-borne sound attenuation, another form of damping found to have a significant effect on sound transmission through timber floors is the addition of an absorbent, fibrous material into the internal floor cavity [27, 59, 60]. In this case, the material has a damping effect on the resonance of the air in the cavity, thereby decreasing the degree to which airborne sound in the cavity excites the ceiling assembly, which in turn radiates sound into the receiving room.

2.5.3 Active and semi-active vibration control

Active control of structure-borne sound is an approach that involves the superposition of out-of-phase waveforms onto existing structure-borne vibrations to produce a cancelling effect. This type of approach has been developed, for example, for noise control applications in vehicles in the form of engine mounts. These mounts integrate sensors and embedded control systems that monitor and analyse steady-state engine vibration inputs to produce out-of-phase outputs [61].

Active control systems offer the potential for low-frequency vibration attenuation. This is because they avoid the key physical issues associated with large wavelengths and passive materials. Instead of trying to ‘stop’ vibrations from passing, they add their own vibrations to the system. Thus, they can evade the need for large mass, high stiffness, or high damping. However, the key difficulty for active systems in the context of structure-borne sound lies in the need to deal with transient waveforms. To be effective, active systems need to adapt to the information contained in the target wave. It is therefore infeasible for them to respond to the first cycle in a transient waveform and very difficult to respond effectively to the residual vibrations that follow [62].

Another challenge for active control systems is in applying sufficient force to counteract existing vibrations. Initial attempts used an ‘in-line’ approach whereby the actuator was situated in the structural pathway. A disadvantage of this approach was that the mount was exposed to static as well as dynamic loads, leading to large, heavy actuators being required. More recently, approaches have been developed which decouple the actuator from the static load path using a parallel arrangement shown in Figure 2.5. This can significantly decrease the structural requirements for the device and, therefore, its weight [63]. Other difficulties associated with active control systems include a susceptibility to dynamic instability, the need for a considerable power source.

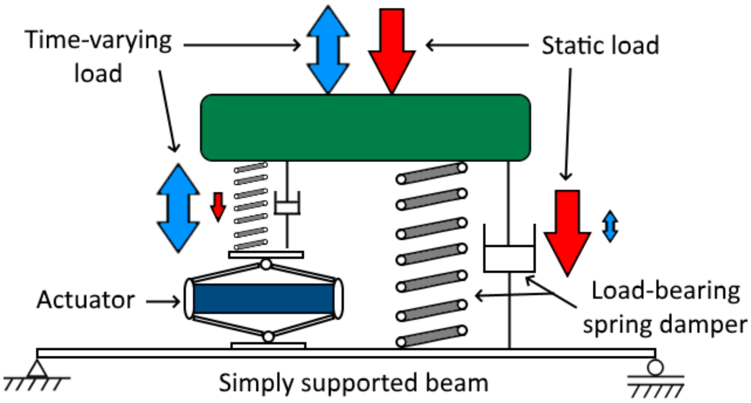

Figure 2.5 Active vibration control system using a static load actuator bypass concept presented by Kraus et al. [52].

An alternative approach that avoids both these issues is referred to as semi-active damping. In semi-active damping systems, damping is achieved by active control of the *stiffness* of passive dampers. This approach has the advantage of dramatically reducing power requirements and improving dynamic stability. A wide range of semi-active damping approaches has been developed. These include the use of magnetorheological fluids with magnetically controlled viscosity, ‘stiffness dampers’ which actively control resistance to the flow of a hydraulic damping fluid and piezoelectric dampers, which operate by active control of the stiffness of piezoelectric materials [64].

2.5.4 Floating floor systems

Floating floor systems are vibration isolation systems placed over the top of existing floors. They comprise a stiff (usually heavy) upper layer over the top of a material or materials that provide both resilience and damping. The sound attenuation achieved by a floating floor can be estimated by treating the system as a mass-spring using the following relation [30]:

$$\Delta L = 30log\frac{f}{f^0}\ \ (dB) \tag{2.7}$$

where, the resonance frequency, f_0, is given by:

$$f_0 = \frac{1}{2\pi}\sqrt{\frac{s'}{m'}}\ (Hz) \tag{2.8}$$

where s' is the dynamic stiffness of the resilient layer and m' is the mass per unit area of the floating slab [65]. The effectiveness of the system for a particular frequency is therefore dependent on its natural frequency. As an undamped mass-spring, the system can be said to perform as a low-pass filter wherein frequencies below the natural frequency are allowed to pass with little attenuation. Using this relation, it can be shown that a 6 dB reduction for a 20 Hz vibration requires either a layer of concrete approximately 160mm thick or a high-performance, resilient layer over 300mm thick. While this relation correlates well with experimental data, Schiavi [66] suggests that it may slightly overestimate the improvement for frequencies close to the floor's fundamental frequency, particularly for floors with low levels of damping. However, for floors with moderate levels of damping, predictions were shown to be in reasonable agreement with experimental data. An alternative empirical formulation was suggested by Schiavi, et al. [67] in which the floating floor is treated as a damped mass-spring system:

$$\Delta L = [37.5 - 33\zeta] log \frac{f}{f^0}\ (dB) \tag{2.9}$$

where ζ is the damping ratio of the resilient material. The concept of a floating floor as a damped mass-spring system is illustrated in Figure 2.6.

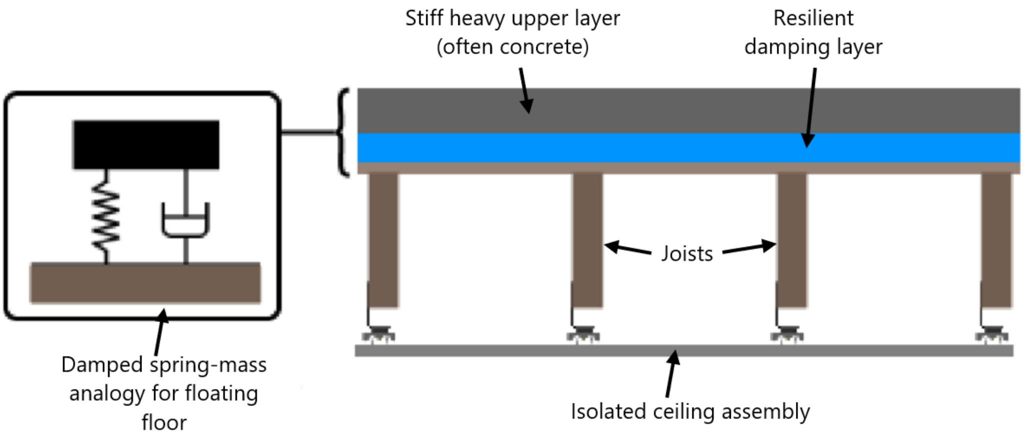

Figure 2.6 Floating floor system conceptualised as a damped mass-spring system.

A wide variety of materials have been investigated for both the floating slab and resilient layers. Effective materials for floating slabs include double layers of OSB, plywood and concrete [32, 68]. Effective, resilient under-layers include various forms of viscoelastic foam, expanded rubber, recycled cotton, sand, sawdust, and granulated rubber [69-73]. Caniato et al. [72] showed that an important concern for resilient layer selection arises due to long term compressive creep. Materials with compressive creep higher than 20% were shown to deteriorate in their insulating performance by more than 3 dB over time.

Sand, sawdust, and granulated rubber represent a form of damping known as particle damping. This approach achieves energy dissipation via friction as particles move against each other. Chung et al. [71] achieved reasonable results down to 50 Hz using an 85 mm layer of 80% sand and 20% sawdust between two layers of plywood separated by timber battens over an LVL joist structure. The ceiling assembly comprised two layers of high-density plasterboard attached via light gauge steel battens and resilient clips. Occupants rated the floor as superior to a reference concrete slab for impact sounds made by a tapping machine but not for actual footfall impacts. It has been shown that in order to achieve damping of frequencies down to 20 Hz with this approach, impractically heavy particles are required, which in turn necessitate large amplitude vibrations for the damping mechanism to be activated [74].

One particular application of particle damping, which integrated several other attenuation mechanisms to achieve good performance down to 50 Hz, was reported by Medved' et al. (2014) [60]. In that instance, a sand-gravel filled, OSB floating floor was mounted on rubber pads over an open joisted floor system. The floor itself was also partially filled with a sand-gravel mix, and the rest of the cavity was filled with mineral wool. The high performance of that system was largely attributed to the use of small (45 x 45 mm) rubber pads instead of continuous lines or whole layers of resilient material. This 'point elastic' support system has also been shown to be effective for floating floors over CLT floors [75], and glulam beam joisted floors [56]. It should be noted that compressive creep, while not considered in those studies, may negatively affect the performance of systems due to the fact that some rubber materials, when used in the form of pads as opposed to continuous layers, have been shown to exhibit deteriorating performance over time [72].

2.5.5 Resiliently mounted ceilings

Resiliently mounted ceiling systems employ resilient connectors that allow relative movement between the vibrating main structure and the ceiling. The effect of this is to lower the resonance frequency of the ceiling assembly, thereby creating an impedance mismatch. This causes incident waves to be partially reflected back into the structure [76]. Resilient ceilings have become widely used for the attenuation of vertical structure-borne sound transmission in multi-story timber buildings. A wide range of mount types is available, including resilient hooks, springs, channels, pads, and a variety of clips. A common general approach combines a steel interface for connection to the underside of the floor structure, some form of resilient interlayer and a steel furring channel for connection to the ceiling material. An example of such a system is shown in Figure 2.7.

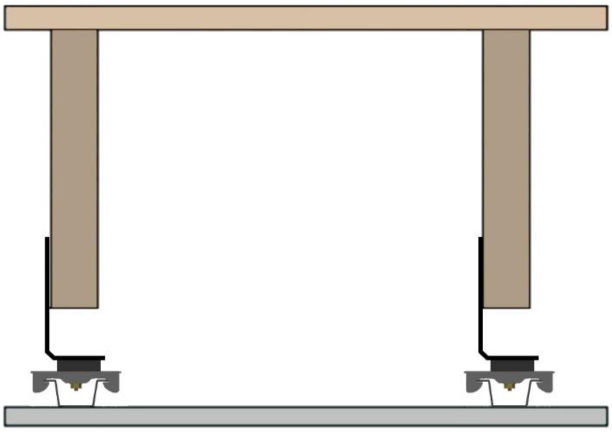

Figure 2.7 Example of a resilient ceiling mount system employing metal clips attached to rubber mounts.

Nightingale et al. [32] performed an extensive regime of measurements of air- and structure-borne transmission through intertenancy wall and floor systems for a range of different timber-based designs. They showed that resiliently mounted ceilings improved impact sound transmission ratings by 12 dB. However, this measure was based on calculations that ignored frequencies below 100 Hz. In a more detailed investigation of frequency spectra, Sipari [6] showed that a resiliently mounted ceiling improved sound attenuation for frequencies above 60 Hz but had a negative effect on performance for frequencies below 50 Hz when compared with a directly fixed ceiling system.

2.6 New approaches for low-frequency attenuation

2.6.1 Introduction

It has been demonstrated that traditional methods of attenuation for 20 – 120 Hz structure-borne sound are limited by the large amounts of mass, stiffness, or distance required to either reflect or damp long wavelengths. In this section, a new approach to the engineering of structures is discussed wherein locally resonant substructures, designed into larger host structures, can be used to induce dynamic responses that would otherwise be unachievable in standard materials. This class of materials is referred to as acoustic metamaterials [11-14]. The term metamaterial was originally used in solid-state physics to describe materials with specifically designed internal structures that changed the way electromagnetic waves passed through them [13]. With the application of the same principles to vibroacoustic waves in larger-scale structures, effective properties such as infinite or negative mass density or bulk modulus have been demonstrated in the laboratory [77, 78]. This has opened the door to a wide range of new possibilities in the design of materials for the manipulation of sound waves such as acoustic lenses, waveguides, cloaking and attenuation.

Broadly speaking, metamaterial analysis employs mathematical descriptions of macro-structures containing locally resonant substructures that enable their treatment as homogeneous materials for the purposes of engineering design. The purpose of this section is to provide the reader with a broad understanding of the principles, issues, and potential applications of acoustic metamaterials in the context of structure-borne sound attenuation in timber floors. To that end, the author has attempted to keep technical details to a minimum to make the information accessible to the non-acoustician. For more in-depth introductions relating to technical details, historical developments and non-attenuation related applications of acoustic metamaterials, the reader is referred to [11, 14].

2.6.2 Vibroacoustic attenuation in linear acoustic metamaterials

Of the many potential applications of acoustic metamaterials, the attenuation of low frequencies has been among the most widely studied. Using periodic arrays of locally resonant structures designed to interact with those frequencies, researchers have been able to demonstrate attenuation that was previously not possible with classical material properties. In these structures, frequency ranges in which wave propagation is possible (pass bands) and those in which it is not (stop bands or bandgaps) form ‘acoustic band structures’ that resemble quantum mechanical, electronic band structures. Such materials are referred to as ‘spectral gap materials’ [79]. Some of the theory behind these concepts is discussed in Section 2.6.3: *Acoustic band structure and spectral gap materials*. It is found that the bandgaps in these structures appear in frequency ranges where ‘effective’ mass density or stiffness become negative. These concepts, and some key research into potential solutions that have employed them, are considered in Sections 2.6.3.1: *Negative effective mass density* and 2.6.3.2:*Negative effective modulus*.

Further, it is found that the width of attenuation bands can be predicted by a consideration of the resonator-to-structure mass ratio and resonant modes within the system. Analyses that have investigated these relationships and some of their implications are discussed in Section 2.6.3.3: *Attenuation bandwidth*. Finally, boundary effects become increasingly important for low frequencies in finite systems. Continuum analysis techniques, shown to be well suited to addressing boundary effects, have revealed a range of insights into the behaviour of finite systems. These techniques, and some insights that have been derived, are discussed in Section 2.6.3.4: *Continuum-based analysis*.

2.6.3 Acoustic band structure and spectral gap materials

A key property of acoustic metamaterials is their potential to exhibit frequency ranges in which no vibration modes can propagate for any wavelength (and, therefore, its inverse, wavenumber). These frequency ranges are known as bandgaps. Conversely, ranges in which waves *can* propagate are referred to as passbands. The distribution of bandgaps and passbands for an acoustic metamaterial can be attained by plotting the relationship between frequency and wavenumber for each vibration mode in the system. These are called dispersion curves, and the set of dispersion curves is referred to as the acoustic band structure (Figure 2.8 (a)).

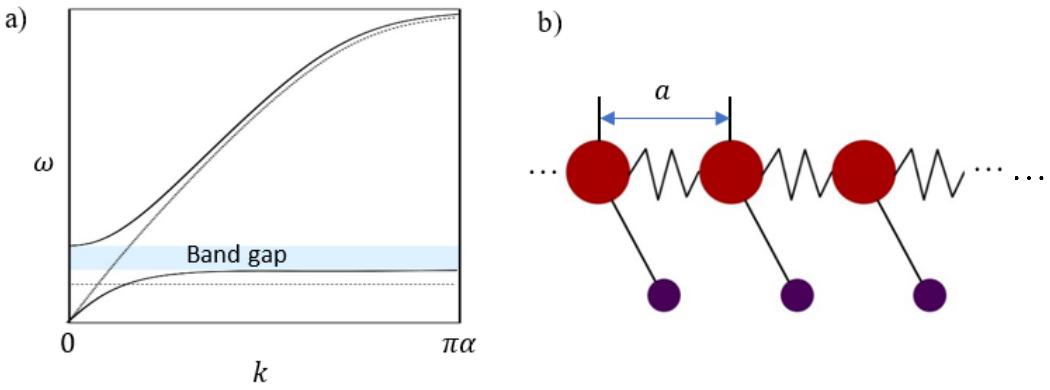

Figure 2.8 (a) Acoustic band structure for a one-dimensional acoustic metamaterial with unit cells containing two degrees of freedom. Dotted lines show dispersion curves for the spring-mass and the pendulum when they are decoupled. Solid lines show dispersion curves for the coupled system. The bandgap is shown in blue. (b) a segment of the 2-dof acoustic metamaterial. Adapted from [80].

In a non-dispersive system, the curves are linear, and their gradient shows that the wave (phase) speed is constant, independent of frequency,

$$\omega = ck \tag{2.10}$$

where ω, c and k are the angular frequency, wave speed and wavenumber, respectively. The wave speed is governed by the stiffness (shear modulus for a shear wave) and density of the material as follows,

$$c = \sqrt{G/\rho} \tag{2.11}$$

where G and ρ are the shear modulus and mass density, respectively. However, if the material contains internal variations, local resonances or nonlinearities, wave speed may vary with frequency, thereby making the dispersion curve nonlinear. In some instances, this can lead to frequency ranges into which no dispersion curve enters for any wavenumber, thus opening a bandgap. Such a gap is shown in blue in Figure 2.8Figure 2.8 (a). Dispersive materials in which bandgaps appear are referred to as spectral gap materials [79].

A significant amount of attention has been given to spectral gap materials that contain periodic variations but no locally resonant substructures. These are referred to as phononic crystals. In phononic crystals, negative interference patterns caused by reflections between periodic material phases or geometric structures produce an attenuation effect referred to as Bragg scattering [13]. A limitation of this effect is that it requires the dimensions of periodic unit cells to be in the order of the wavelengths to be attenuated. In timber floor structures, wavelengths for 20 – 120 Hz vibrations can range from approximately 3 to 10 m, thus limiting the potential of Bragg scattering for attenuating this frequency range.

In acoustic metamaterials, periodicity has been shown to be unnecessary [81], and bandgaps are produced by oscillations in locally resonant substructures interacting with target waves in the larger structure. Here, it is the natural frequency of the resonant substructures that must be similar to that of the target waves, as opposed to their dimensions. Since the natural frequency of a spring-mass resonator can be tuned by altering its mass and/or its stiffness, resonator systems can be designed to manipulate wavelengths much larger than the physical dimensions of the units themselves. In the following section, the connection between the appearance of bandgaps in locally resonant systems and a dynamic phenomenon known as negative mass density is discussed.

2.6.3.1 Negative effective mass density

As was mentioned in the previous section, in a non-dispersive material, wave speed is independent of frequency. In dispersive materials, that is not the case. An implication of this is that the traditional relationships between stiffness, mass density, frequency, and wavelength (discussed in the previous section), no longer hold for wave propagation at the macro-level. It is possible, however, to derive expressions for ‘effective’ or ‘dynamic’ stiffness and mass density which describe the macro-behaviour of a locally resonant structure *as if* it were homogeneous. To do so, it is necessary to account for internal dynamic effects which make these *effective parameters* frequency-dependent.

To illustrate the concept of a vibrating system that exhibits negative effective mass density, Figure 2.9 shows a two degree of freedom system comprising a host structure of mass, m_{host} driven by a sinusoidal input force, $\boldsymbol{F}$ with a resonator of mass, m_{res} attached internally via a spring of stiffness, k_{spring}.

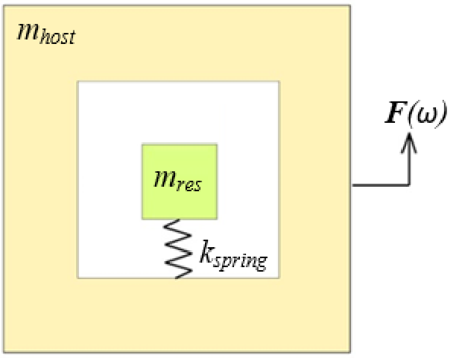

Figure 2.9 Composite block with three material phases under harmonic excitation

When the host structure is driven by a sinusoidal input force, F with angular frequency, ω, the system's inertial resistance to that force (i.e., its *effective* mass (M_{eff})) will be influenced by the relative motion of the internal resonator. It can be shown that this influence is governed by the mass of the resonator (m_{res}) and the ratio of the driving frequency (ω) to the natural frequency of the resonator (ω_0) according to the following equation:

$$M_{eff} = m_{host} + \frac{m_{res}}{1 - \omega^2/\omega_0^2} \tag{12}$$

where $\omega_0 = \sqrt{k_{spring}/m_{res}}$. The relationship between M_{eff} and ω is illustrated in Figure 2.10. As the frequency approaches the resonant frequency of the oscillator (ω_0), the effective mass tends to infinity. At that point, a 180° phase change occurs, the effective mass becomes negative, and m_3 starts to resonate out of phase with the main structure. It is this response that is associated with negative mass density-induced bandgaps.

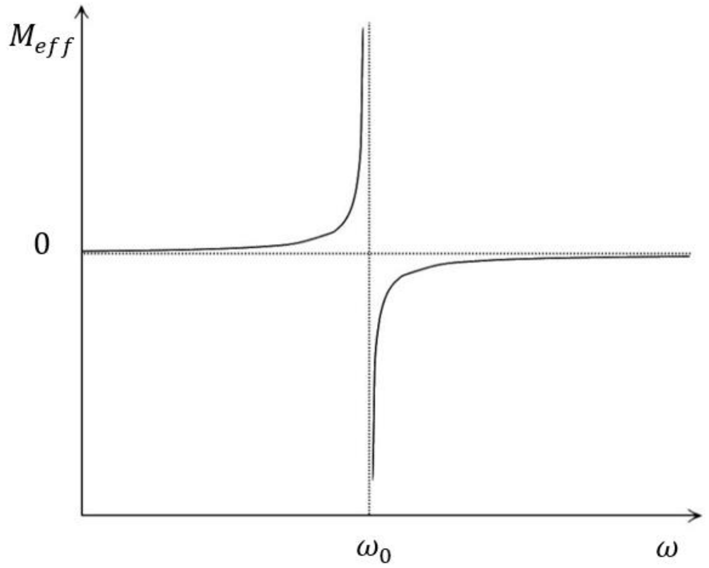

Figure 2.10 Trend line for effective mass against frequency for the mass-in-mass system

The use of locally resonant inclusions for the absorption of acoustic waves in a metamaterial structure was first demonstrated by Liu et al. [82]. In that study, a three-dimensional lattice of silicone rubber-coated lead sphere unit cells, embedded in an epoxy matrix (Figure 2.11), was shown to attenuate wavelengths two orders of magnitude larger than the unit cell dimensions. The level of attenuation exceeded the limit predicted by the mass density law for acoustic transmission.

Investigations into the attenuation mechanism followed. Goffaux et al. (2002) [83] simplified Liu et al.'s [82] concept to a 2-dimensional array to show that the observed resonant behaviour closely resembled that of Fano interference, a well-known interference pattern observed in atomic physics. This suggested that the attenuation mechanism could be understood in the context of self-cancellation effects. Liu et al. [84] derived expressions for effective mass densities of two- and three-dimensional locally resonant metamaterials and showed that bandgaps appeared in frequency ranges for

Figure 2.11 Illustration of three-dimensional lattice of locally resonant silicone rubber coated lead spheres presented in Liu et al. [82]

which the effective mass density was negative. A number of studies have since investigated the tendency of the effect to occur for frequencies at which the motion of the resonators is out-of-phase with the vibrating matrix [84-86].

Other studies have investigated a range of structures comprising arrays of locally resonant sub-structures, including plates with attached resonators [87, 88], mass-decorated membranes [89-94], rigid grids with resonant mass inclusions [95] and rods with periodic spring-mass resonators [96].

2.6.3.2 Negative effective modulus

As has already been discussed, the parameters governing elastic wave propagation are the mass density and stiffness (modulus) of a material. As with negative mass density, it has also been shown that bandgaps tend to appear in structures that exhibit frequency ranges in which the effective *stiffness* becomes negative. Frequency-dependent effective moduli in dispersive materials are now discussed. For longitudinal and transverse elastic waves, Young’s and shear modulus apply, respectively. For pressure waves in fluids, bulk modulus applies. As was illustrated for dynamic mass density, a similar analysis procedure can be performed to derive the dynamic modulus for sub-structure configurations that produce frequency dependency in that domain [97].

Fang et al. (2006) [78] studied ultrasonic acoustic wave propagation through a pipe with a series of Helmholtz resonators attached along its length. The system was shown to exhibit negative effective bulk modulus and an associated bandgap in a narrow frequency range close to its resonance frequency. Similarly, Hyeon et al. (2009) [98] studied low-frequency acoustic wave propagation through a pipe with a series of holes along its length, which was shown to exhibit a negative effective bulk modulus for frequencies in the range of 0 – 450 Hz. In that range, acoustic wave amplitudes were shown to decay to near zero within a meter of pipe length.

In relation to structure-borne attenuation, Huang & Sun (2011) [99] investigated a locally resonant mechanism comprising springs, masses and trusses designed to exhibit a frequency-dependent effective Young's modulus. It was shown that at a certain threshold input frequency, the modulus became negative before tending to (negative) infinity as the resonance frequency was approached. A bandgap was shown to coincide with the frequency range in which the effective modulus was negative. Sugino et al. [100] showed that a bandgap governed by dynamic stiffness could be produced using electromechanical coupling with resonant circuits. To do so, they added piezoelectric layers to the upper and lower surfaces of a beam and connected them to a series of shunted resonating electrical circuits. This bandgap was shown to be independent of the mass ratio but could be merged with the local resonance-based bandgap in the presence of damping. The result was an increase in bandgap width without an increase in required mass [97]. In the next section, factors affecting bandgap width are considered in more detail.

2.6.3.3 Attenuation bandwidth

An important aspect of metamaterial design for structure-borne sound attenuation is the bandwidth of the frequency attenuation. In locally resonant metamaterials with resonators tuned to a single frequency, it has been shown that the normalized attenuated frequency range (γ), can be approximated as:

$$\gamma = \frac{f_{high} - f_{low}}{f_{low}} = \sqrt{1 + \frac{m_{res}}{m_{host}}} - 1 \qquad (2.13)$$

where f_{high} *and* f_{low} are the upper and lower bounds of the bandgap, respectively, m_{res} is the mass of added resonators and m_{host} is the mass of the bare host structure [101]. A version of this relationship was first derived by Wang et al. [102] for a one-dimensional beam with attached spring-masses. Peng & Pai [88] then extended it to two-dimensional plates, and Sugino et al. generalized it for one, two, and three-dimensional systems [101]. From this equation, it can be seen that the bandgap width increases with the square root of the mass ratio. Therefore, using a linear, single frequency, tuned local resonator array, even to achieve a normalized bandgap of $\gamma = 1$ (equivalent to a single octave), would require a mass ratio of three. To achieve a bandgap that spans a 20 – 120 Hz frequency range ($\gamma = 5$), the total resonator mass would need to be approximately thirty-five times that of the bare floor structure. This is clearly an issue for these types of systems; however, it will be shown in sections 2.6.4 and 2.6.5 that several approaches for reducing this mass have shown significant potential.

More recently, Banerjee et al. (2016) [103] investigated a Fourier transform-based methodology for the determination of the width of the attenuation band in locally resonant metamaterials. It was found that the bandwidth was not only governed by the ratio of resonator mass to structure mass but also by the ratio of the natural frequency of resonating units to that of the structure. This suggests a new parameter that may be optimized in order to maximize the attenuation bandwidth.

2.6.3.4 Continuum-based analysis

Most mathematical analyses have simplified the problem of analysing metamaterial systems using a lumped mass approach. This works on the assumption of an infinite one- or two-dimensional periodic array of identical units and enables the study to focus on just a single unit [104]. While the lumped mass approach enables theoretical insights to be garnered from simplified systems, it has the disadvantage that it does not easily account for boundary condition effects. This is of particular importance in the analysis of very low frequencies. Pai, Peng & Jiang [105] showed that, in the case of low frequencies, the wave profile of the vibration is determined by the boundary conditions of the system. Their presence in the analysis is therefore essential for accurate modelling. The study also showed that in these situations, the location of individual vibration absorbers becomes important.

Instead of a lumped mass infinite structure, Sugino et al. [106] undertook an analysis using a continuum model for a one-dimensional finite beam which was then generalized to two-dimensional plates in [101]. One of the results derived from this investigation has already been discussed in relation to equation (2.13). Several other useful observations were made in that study:

- There is an optimal number of resonators that will produce the widest possible bandgap for a given weight addition, which depends on the frequency neighbourhood being targeted. The optimal number decreases with decreasing frequency.

- Bandgaps can be generated in non-uniform structures by distributing local resonators such that their mass distribution matches that of the bare structure.
- Variation between resonant frequencies of resonators decreases the width of the bandgap. A standard deviation relative to the target frequency of 0.05 roughly halved the bandwidth, and a relative standard deviation of 0.1 eliminated the bandgap altogether.
- Uniformity of resonator placement within the structure is not necessary for bandgap generation.

2.6.4 Potential methods for resonator weight reduction

In the previous section, it was shown that a large amount of mass is required to attenuate low frequencies in wide bandgaps using linear, low degree of freedom systems. This indicates that an approach that reduces that requirement is needed for local resonance to be practical as a solution for real floor systems.

2.6.4.1 Multiple tuned resonator arrays

In linear, locally resonant systems, resonator/structure mass ratio varies with the square of the bandgap width. This suggests that by dividing the target frequency range into several smaller ranges, separately tuned resonator arrays could be employed to target each sub-range. Huang & Sun [107] studied a system of mass-in-mass units from an energy transfer perspective and found that the mechanism of wave attenuation was based on the temporary transfer of energy from the larger structure to the locally resonant units for frequencies close to the resonant frequency of the resonators. The study also showed that for a pulse comprising a range of frequencies, several resonator arrays, each consisting of different resonant frequencies, could be employed to attenuate the pulse. The attenuation effect of a series of four tuned resonator arrays, which created four separate but overlapping stopbands, can be seen in Figure 2.12.

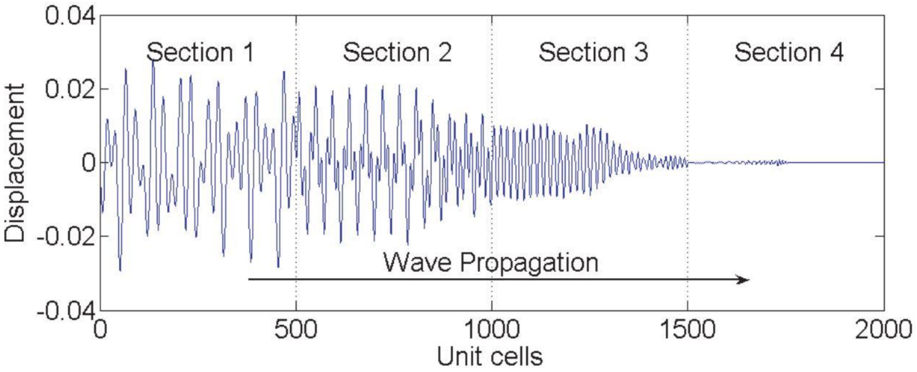

Figure 2.12 Snapshot of wave propagation in a metamaterial studied by Huang & Sun [107]; each section consists of a specifically selected stopband targeted by a tuned locally resonant array.

Pai, Peng & Jiang [105] also studied a multi-frequency vibration absorber (Figure 2.13) and showed that a stopband was opened on the high side of the tuned frequency of each locally resonant array.

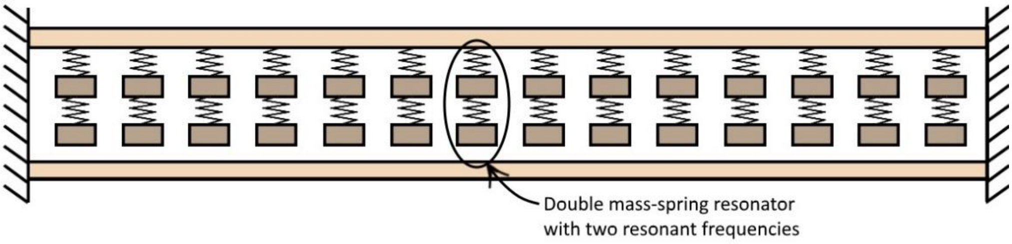

Figure 2.13 Multi-frequency vibration absorber metamaterial studied by Pai, Peng & Jiang [105].

Zhu et al. [108] found that undesirable passbands tended to form in a Timoshenko beam with multiple tuned embedded resonators due to dynamic interaction between them. To control this, a chiral elastic beam structure with embedded resonators was studied, and it was found that individual stopbands could be tuned to overlap, thus creating a single broad stopband.

2.6.4.2 Inertial amplification

Another approach that has been investigated is the use of inertial amplification. This employs structural geometries that amplify the motion of resonators in response to input vibrations. This leads to an increase in the effective inertia of the vibrating system and thus, a decrease in mass requirements. Yilmaz, Hulbert & Kikuchi [109] were the first to propose the use of inertial amplification for locally resonant systems and showed that the approach could be used to generate much wider bandgaps at low frequencies than would be possible with simple locally resonant inclusions. An example of an inertial amplification lattice structure is shown in Figure 2.14.

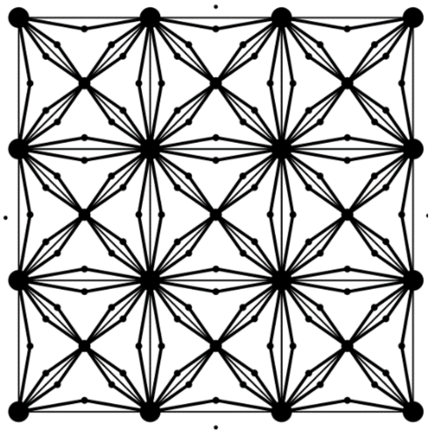

Figure 2.14 Geometry for an inertial amplification structure proposed by Yilmaz & Hulbert [110]. The small angles between pairs of connectors amplify the motion of the small, suspended masses in relation to relative motion between the large masses. The study was carried out parametrically, with mass and static stiffness held constant. All other dimensions were expressed relative to those. Manufactured dimensions would depend on the frequency range being targeted.

This work was followed up by a number of other studies over the next decade, which investigated the effects of different geometries on the nature of the bandgaps produced [110-113]. Aside from generating wider bandgaps with the same amount of mass, it was also shown that the shape of the attenuation curves tended to be smoother with fewer resonance peaks than with simple locally resonant inclusions [110]. Frandsen et al. [114] proposed an approach that applied the principle of inertial amplification to a geometry that allowed resonators to be added to a structure without interfering with the structure (Figure 2.15). With this configuration, wide and deep bandgaps were produced compared to standard local resonator systems for longitudinal waves. An attempt to extend the approach to transverse waves using the same geometry was made by Li & Li [115]. However, for transverse waves, amplification structures must extend a significant distance perpendicular to the base structure (θ >> 45° in Figure 2.15), thereby limiting the practicality of this approach.

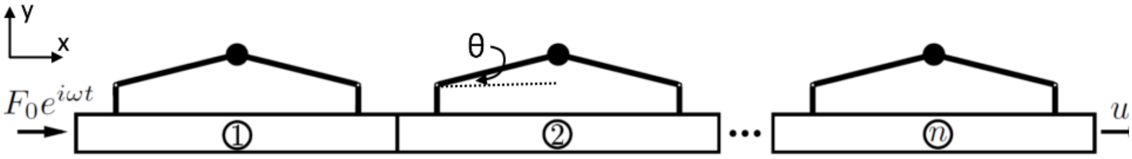

Figure 2.15 One-dimensional inertial amplification lattice for transverse wave attenuation [114]

Based on design concepts presented by Yilmaz et al. [110], (Figure 2.14), Schmied et al. [116] modelled and tested an integrated inertial amplification geometry that inserted resonators into an inertially amplifying webbing design for a beam (Figure 2.16). The load-bearing frame was modelled, fabricated, and tested and showed that the width of the bandgap increased for a given mass addition, but the complexity of the geometry led to poor analytical predictions. Xiao et al. [117] investigated the use of beam-like resonator attachments to generate overlapping locally resonant and Bragg-induced bandgaps, which increased the bandwidth for a given weight. A similar effect was produced in [118] using mass-spring resonators attached to a plate.

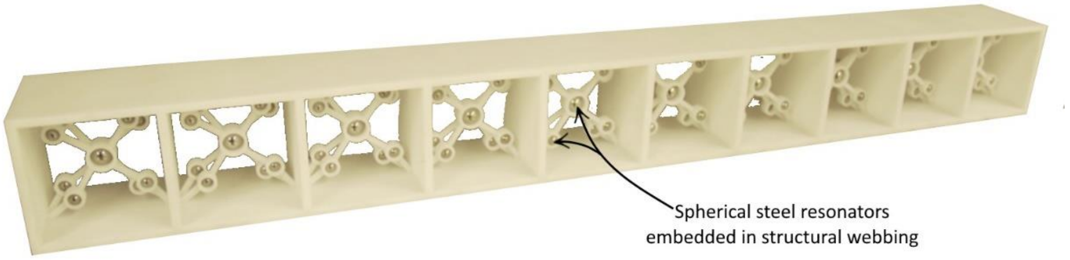

Figure 2.16 3-D printed prototype of an inertial amplification beam structure with structurally integrated resonators [116]

In a study of three-dimensional auxetic micro-lattices, Krödel et al. [119] found that it was the addition of locally resonant masses that led to the appearance of bandgaps rather than the auxeticity of the structure. In terms of the ratio of bandgap width to mass, the best performing structure was a non-auxetic honeycomb with the masses located so as to maximize their inertial amplification.

More recently, Al'ba'ba'a et al. [120] undertook a closed-form analysis of wave dispersion behaviour and dynamic response in both infinite and finite inertially amplified acoustic metamaterials. The derived framework revealed insights into the effects of inertial amplification on bandgap formation and an associated onset of unique anti-resonances, as well as bandgap width. Conditions needed to obtain both bandgap widening and narrowing were identified. Using insights derived from the analysis, it was shown theoretically that a metamaterial configuration employing local inerters in place of local resonators could generate dispersion behaviour identical to that of a locally resonant metamaterial.

Only a small amount of research has investigated the application of metamaterials for real floor systems. So far, to the authors' knowledge, none has been applied to timber structures. Mitchell [121] modelled a concrete slab with an array of locally resonant lead spheres and predicted that a significant amount of input energy would be attenuated. In a follow-up experimental study based on these designs, Kettenbeil & Ravichandran [122] showed that the maximum strain experienced by the concrete matrix was attenuated by 72%. Based on designs from [88], Zhong et al. [123] numerically investigated the efficiency of an I-girder with attached local resonators and showed that the width of bandgaps could be increased by increasing both the resonator mass and damping.

2.6.5 Nonlinear acoustic metamaterials

Work in relation to local resonance described thus far has focused on linear mechanisms for bandgap generation. A related area of research that has shown great promise for increasing the bandwidth of attenuated frequencies involves the addition of nonlinearity into the vibration response of local resonators [74, 124-128]. Nonlinearity is often considered undesirable in engineering design due to the complexity it adds to design and analysis procedures and the often unpredictable chaotic behaviour that it can engender. However, it also has the potential to open up possibilities for harnessing wide-ranging beneficial dynamic behaviours. A nonlinear resonator does not exhibit the same preferential response to specific resonance frequencies as do linear resonators. This has the effect of widening the bandwidth of the frequencies it can attenuate.

Nonlinearity can be added to a system in a range of ways, including through the use of nonlinear springs, magnetic force interactions, nonlinear damping elements, and nonlinear material and geometric properties. A common approach for modelling nonlinear force-displacement relationships is with the addition of a cubic nonlinear term into the linear equations of motion. This effectively converts the linear force-displacement term (commonly known as Hooke's law) to a cubic function. Oscillators employing cubic nonlinearity in this way are known as duffing oscillators [129]. Discontinuous motion, often in the form of internal impacts, can also be used to introduce high levels of nonlinearity. This can cause a resonator responding to low frequencies to excite higher frequencies within the structure, leading to enhanced energy dissipation through damping [130-133] and represents a specific example of a broader tendency in nonlinear systems toward an amplitude-dependent broadening of the bandwidth of response interactions. Such broadening can occur due to sub- and super-harmonic resonance, period multiplication and chaotic behaviour.

Related to the development of research into multi-resonator nonlinear systems, a significant body of work has investigated the design and behaviour of individual nonlinear resonators and their interactions with vibrating structures. This includes research into nonlinear energy sinks [134], nonlinear tuned mass dampers [135], magnetorheological dampers [136], and friction dampers [137]. This work developed out of a need to improve upon the frequency sensitivity and robustness of linear tuned mass dampers. In particular, significant attention has been directed towards the nonlinear energy sink (NES). A NES is a damped oscillator with internal nonlinearity that induces an irreversible energy flow from the main structure into the resonator, where it can be dissipated via damping [134]. This energy flow is variously referred to as nonlinear energy pumping or targeted energy transfer. A full description of work on nonlinear energy sinks is beyond the scope of this review, and only a selection of key articles relevant to the work in this thesis is presented here. For a broad overview of previous work, the reader is referred to [134, 138] and for a more comprehensive treatment of the subject, see [139].

Vakakis [140] analysed energy pumping in an impulsively excited two-DOF system with nonlinear attachments and formulated an envelope modulation-based criterion for energy pumping. This principle was then extended to a multi-DOF linear chain with nonlinear attachments. Gourdon et al. [141] experimentally demonstrated energy pumping from a small-scale prototype building structure to a nonlinear energy sink via 1:1 resonance coupling associated with the generation of quasiperiodic vibrations. Starosvetsky et al. [142] investigated response regimes in a linear oscillator with an attached NES with piecewise quadratic damping and showed that the same amount of energy was transferred from the oscillator as a linear tuned mass damper but in a broader range of frequencies and with the elimination of previously problematic dangerous periodic regimes.

Georgiadis et al. [143] extended the NES concept to flexible systems by investigating an NES attached to a linear flexible beam and showed that up to 87% of shock energy could be locally dissipated.

One method commonly employed for inducing nonlinearity in an NES is through the addition of internal impacts. Such a design is referred to as a vibro-impact NES (VI-NES). Vakakis et al. Georgiadis et al. [17] showed that an NES design employing clearance nonlinearities was able to rapidly absorb a significant portion of the energy in the initial stage of a shock loading response. Lee et al. [18] found that the most efficient mechanism for targeted energy transfer in a VI-NES connected to a single DOF linear oscillator is through the excitation of highly energetic vibro-impact orbits, and further that the VI-NES can more rapidly absorb and dissipate the initial transient energy front arising from a shock input than an NES with smooth nonlinearity. Nucera et al. [144] demonstrated the potential of VI-NESs to mitigate a building's response to seismic excitation and showed that vibro-impacts redistribute energy from lower to higher modes in the primary linear (host) structure whereby amplitudes are decreased, and energy can be dissipated more rapidly via damping. Li et al. [145] investigated chaotic behaviour in a system comprising a linear oscillator with an attached VI-NES and found that irregular and desynchronized impacts were responsible for the development of chaotic activity in different response regimes.

Wave propagation in periodic chains of nonlinear oscillators has been investigated by a number of researchers [128, 131, 146-149]. Vakakis [149] studied an infinite chain of nonlinear oscillators with a forced cyclic input and found localised, non-localised and chaotic motions to be possible. In chaotic motion, complex, aperiodic behaviours are found to be governed by deterministic laws that are highly sensitive to initial conditions.

In localised motions, the system displays large amplitude motion in localised regions while the broader system exhibits much smaller amplitudes. This differs from energy pumping in that it does not constitute a flow of energy from the structure via damping.

Narisetti et al. [146] developed a novel perturbation analysis approach to investigate amplitude-dependent dispersion properties of a chain of nonlinear resonators and demonstrated the possibility of amplitude-dependent frequency isolation. Fang et al. [147] investigated 1D diatomic and tetratomic nonlinear chains containing damped nonlinear oscillators and demonstrated broadband wave attenuation with period-doubling leading to chaotic behaviour which was significantly affected by the level of damping. Banerjee et al. [131] modelled a chain of nonlinear oscillators with internal vibro-impacting oscillators and found that a five-unit chain could decrease vibration in the system by as much as 50 dB in an attenuation band that increased in width with the number of units. Fang et al. [128] theoretically and experimentally demonstrated acoustic limitation in a similarly broadening attenuation band using a nonlinear chain which also comprised internal vibro-impact oscillators

Resonators in many of the systems discussed above are arranged in such a way that they form part of the structural pathway (i.e., they are structurally embedded within the host structure). Their stiffness is therefore limited by that of the springs connecting their unit cells. This limits their potential in structural applications. A much smaller body of research has focused on nonlinear metamaterials that employ *non-structural* resonators. Khajehtourian [150] theoretically investigated longitudinal wave propagation in a thin rod with internally attached spring-mass resonators and showed that nonlinearity increased with amplitude with the potential for bandgaps to merge due to the degree of nonlinearity. The source of nonlinearity in that study was due to large elastic deformations of the rod, while the attached local resonators were linear. Zhou et al. [127] investigated low-frequency attenuation performance in an Euler-Bernoulli beam with a series of attached nonlinear, high-static-low-dynamic stiffness resonators. In that study, the effective mass ratio was increased by inertial amplification to achieve a widening of the low-frequency bandgap.

Fang et al. [15] reported on a metamaterial for the attenuation of transverse bending waves, which employed multiple, nonlinear resonator attachments orthogonally attached to a lightweight beam. In that configuration, the resonators took the form of cantilevered assemblies which left the structural pathway of the host beam unaffected (Figure 2.17). Resonators comprised nonlinear magnetic springs coupled with vibro-impact oscillators. It was shown that very broadband, low-frequency attenuation of transverse waves could be achieved in a lightweight beam.

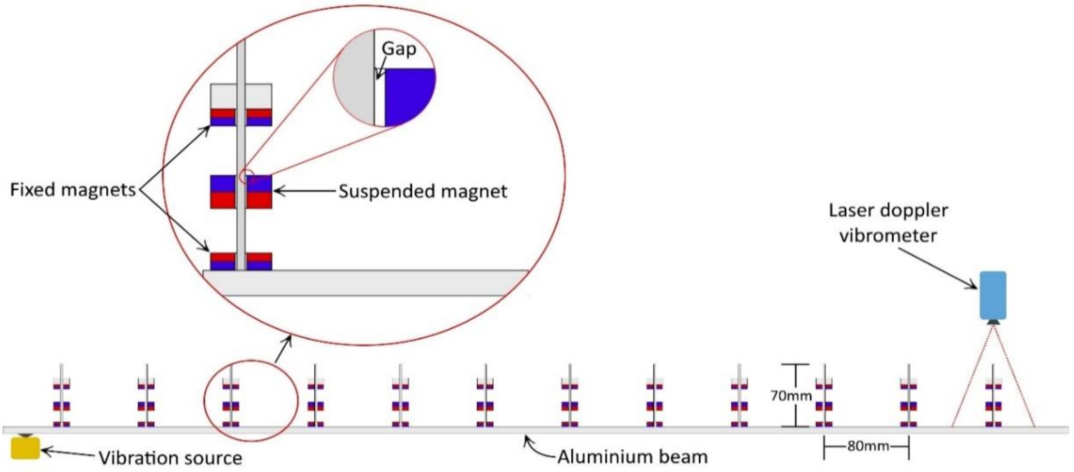

Figure 2.17 Nonlinear locally resonant acoustic meta-beam. In 2-d plate form, this approach reduced the weight requirement for a fixed bandgap width by a factor of thirty-nine [15].

The design achieved a normalized attenuation band of 39 (see equation (2.13)) with a resonator/structure mass ratio of only 0.85 – that is an attenuation band approximately two orders of magnitude larger than a linear system with the same mass ratio. The relative depth of attenuation was shown to correlate with the amplitude of beam vibration, which in turn correlated with the nonlinearity of the response. Attenuation of up to 20 dB was achieved across the whole attenuation band for higher input levels (corresponding to a mean response amplitude response of approximately 0.08 mm). The upper and lower limits of the attenuated frequency band were shown to coincide with the natural frequencies of the nonlinear spring and vibrating cantilevered attachment, respectively. This has been referred to as 'bridging-coupling' in reference to the tendency for two linear bandgaps to apparently 'couple' across a broad intervening frequency band in the presence of highly nonlinear or chaotic behaviour [151].

Another design that employed bridging-coupling with a nonlinear mechanical spring coupled to a vibro-impact oscillator was studied by Sheng et al. [16]. The system was studied using a model similar to that reported in [15]. Effects of excitation amplitude, nonlinear stiffness coefficients, linear internal resonant frequencies, oscillator mass and beam thickness were investigated. Increasing the resonant frequency of the strut was found to have the largest effect on attenuation in the 0 – 400 Hz range. All other parameters were shown to have some effect, and optimal values were identified for the studied system.

2.6.6 Acoustic metamaterials for timber floors

For electromagnetic metamaterial design, internal structures must be similar to or smaller in size than the wavelengths to be manipulated. This has necessitated the fabrication of very small-scale structures, which are often difficult to manufacture. For acoustic metamaterials, the structures tend to be much larger and, therefore, often easier to manufacture. When considering the potential application of acoustic metamaterials for vibration attenuation in timber floor systems, several interrelated issues must be considered. These relate to affordability, manufacturability, buildability, and robustness.

To be affordable, mass-manufacturability of components using readily available, low-cost materials and existing manufacturing processes is essential. Material quantities and precision tolerances must be minimized. While these issues fall in the realm of manufacturing design, they warrant consideration from researchers in the early stages when selecting potential approaches to explore. To be compatible with timber prefabrication technologies, proposed systems need to minimize onsite labour. This might be achieved via the design of modules to be installed onsite. In that case, buildability – i.e., the ease with which the system can be installed – needs to be considered. Alternatively, perhaps preferably, factory integration with existing floor prefabrication systems may be possible. In that case, the metamaterial system would represent an additional component or components to be incorporated into the overall manufacturing process.

Robustness is an issue that relates to the system's ability to continue to perform effectively for a long period of time. This implies an ability to withstand forces and accelerations likely to be encountered during transport and installation. It will also need to be robust against changes in temperature and humidity as well as those associated with creep and other slow changes that may affect performance. This is important for systems that rely on the accurate tuning of resonance frequencies for effectiveness.

There is no obvious reason why these issues should not be able to be solved. However, it remains to be seen whether an approach can be found that will enable the successful development of a robust, lightweight system capable of attenuating broadband low-frequency ranges.

2.7 Research gap

This review has shown that a long-recognised research need for improved low-frequency structure-borne sound attenuation in multi-storey timber buildings remains an open research problem. Many approaches have been investigated previously but they have been found to be inadequate for frequencies between 20 and 120 Hz as discussed in previous sections. The potential for linear metamaterials to attenuate any type of floor vibration has only been addressed in a small amount of previous work, and that work focused on high-frequency blast waves in a concrete floor [121, 122]. No previous work has investigated nonlinear metamaterials for any type of floor, and none has investigated any type of metamaterial to attenuate low-frequency structure-borne sound in lightweight structures. In the following chapters, attenuation systems based on concepts of nonlinear metamaterials will be studied. No previous work has investigated the applicability of these concepts to a real-world problem such as noise attenuation in timber structures; no work has investigated the transient response of such system or prototypes on the scale of a structural floor system, and no work has attempted to model their internal dynamics in a way that reveals the effects of parameters essential for the design of real physical systems.

2.8 Conclusions

Multi-story timber construction has made significant strides in recent years. Developments in engineered structural timber products and fire protection strategies have led to changes in building codes, making timber a simpler and more affordable option than it was decades ago.

Acoustic issues with timber structures have attracted significant research interest, and developments have enabled high acoustic performance in many respects. Double-clad cavity walls, floating floor systems and resilient ceiling mounts are effective for attenuating both air- and structure-borne sound at higher frequencies. However, low-frequency structure-borne sound has remained a difficult problem to solve. This is due to the physics of long-wavelength vibrations and the material and structural properties required to stop them. The problem has remained largely hidden from industry by the fact that most building codes ignore frequencies below 100 Hz. Timber buildings are therefore passing building code requirements when, in fact, they are falling short of the occupant comfort levels the codes were originally designed for.

This review has presented a broad overview of the issues relating to acoustic insulation in multi-story timber buildings. Background information about timber building acoustics has been presented and footfall impact-induced floor vibration has been identified as the primary source of unwanted noise. Research covering existing methods of attenuation, including various applications of mass, stiffness, and resonance, have been reviewed, and their shortcomings with respect to the attenuation of low frequencies have been discussed. The effect of noise exposure on building occupants was also considered. Finally, metamaterial approaches to structure-borne sound attenuation have been reviewed with an overview of the mechanisms by which bandgaps in the frequency response of a structure can be generated. In particular, the potential of metamaterials that employ nonlinearity to increase the bandwidth of attenuated frequencies is investigated. These are shown to be capable of achieving bandwidths up to two orders of magnitude larger than those achieved by linear metamaterials using only a small amount of additional mass.

A major challenge for acoustic metamaterials in this context is to design systems that are both robust to changing conditions and practically manufacturable. Systems need to be capable of attenuating broad frequency spectra without susceptibility to problems associated with detuning and with a minimal additional weight penalty. This represents an important challenge for future research.

Chapter 3. Experimental investigation of a five-resonator beam

3.1 Introduction

This chapter focuses on the development of a nonlinear vibro-impact-based metamaterial system that is being investigated for its potential to attenuate low-frequency structure-borne sound in lightweight building structures. The approach employs nonlinear resonators designed to absorb low-frequency energy from the main structure and convert it to high frequencies via a vibro-impact-based coupling. To investigate the performance of the system, the developed nonlinear resonators are mounted on an aluminium cantilevered beam, and vibration tests are conducted. Experimental measurement of vibrating multi-resonator beams shows significant broadband attenuation of transverse vibration in the low-frequency range, superior to that obtained by the addition of non-resonant mass alone. The effects of several resonator design parameters are investigated, and characteristics of higher-performing configurations are identified. In this study, the best attenuation performance for the full, low-frequency range of interest (20 – 120 Hz) was 8.41 dB. The results demonstrate that the proposed nonlinear, vibro-impact metamaterial design has the potential to improve structure-borne sound performance in buildings.

Low-frequency (20 – 120 Hz) structure-borne sound transmission in lightweight building structures (particularly timber buildings) has presented a significant challenge for noise control engineers for over five decades [1, 7, 10, 19, 50, 152, 153]. In Chapter 2, previous work investigating the dynamics of this problem and potential methods for solving it was presented. Existing systems for attenuating structure-borne sound in these structures have been shown to be ineffective, and sometimes even detrimental, for 20 – 120 Hz frequencies unless very large or heavy cross-sections are employed [1, 154, 155]. Floating floor solutions and resiliently mounted ceilings, which act as low-pass vibration filters, require combinations of large mass and low dynamic stiffness that are impractical for effective attenuation of 20 – 120 Hz frequencies [4, 30, 55, 65, 156-158]. The primary source of problematic sound radiation from vibrating floors is in transverse bending waves. This study seeks an alternative approach to attenuate broadband, low-frequency bending waves in lightweight floor structures as an indicator for improvement in structure-borne sound performance. The novel solution overcomes practical limitations of mass and stiffness by integrating localised, nonlinear resonators that passively absorb, cancel, and disperse low-frequency vibration energy from the host structure.

Much research has been directed towards using linear, locally resonant sub-structures for the passive absorption and cancellation of specific wavelengths in lightweight structures [77, 82, 84, 88, 90, 107, 117, 121, 159-167]. This work is summarised in Chapter 2. By incorporating multiple locally resonant inclusions (often referred to as resonators in the context of the systems discussed in this thesis), frequency bandgaps within which no waves are propagated can be induced. These assemblies are referred to as locally resonant acoustic metamaterials [11, 14, 82]. An important feature of these structures is their amenability to low-frequency attenuation due to the fact that locally resonant sub-structures with low mass can be designed to resonate at, and therefore attenuate, very low frequencies [160, 168, 169].

For practical structural applications, it is necessary to differentiate between two broad acoustic metamaterial design strategies. In the first strategy, the locally resonant inclusions form part of the structural pathway, thereby limiting structural capacity [82, 170]. In the second strategy, the inclusions are attached to the structure as resonant appendages, such that they play no structural role. This makes it possible to design attenuating structures without limiting structural capacity [105, 108, 114, 116, 171-173]. Another important concern for the design of these systems is with the width of bandgaps induced by the locally resonant inclusions. Broadband attenuation is highly desirable for improving the acoustic performance of lightweight structures. In Chapter 2, it was shown that the width of the bandgap in linear, locally resonant acoustic metamaterials is limited by the mass of local resonators relative to that of the host structure (see (2.13). Attempts have been made to overcome this limitation by, for example, merging multiple linear bandgaps [105, 108, 174], amplifying the effective inertia of resonators [109-111, 114, 116, 120, 175] and adding damping into the resonator response [164, 176-178]. However, for low frequencies, the large amount of additional mass still required to induce a wide bandgap remains a significant limitation for linear metamaterial structures.

To increase attenuation bandwidth without the need for large amounts of additional mass, the addition of nonlinearity into the vibration response of local resonators can significantly improve attenuation performance [74, 124-128]. The response of a nonlinear resonator is not limited to a specific resonance frequency in the same way as a linear resonator [124, 148]. This widens the frequency band it can potentially attenuate. In addition to this, the design of discontinuities into the vibration response, often using small clearances between components to induce internal impacts, can cause a resonator responding to low frequencies to excite higher frequencies within the structure [130-133, 179]. This constitutes what can be seen as an energy flow from low to high frequencies that can be much more rapidly dissipated via conventional material damping effects.

A significant amount of research has investigated wave propagation in periodic chains of nonlinear oscillators [103, 128, 131, 147, 148, 179, 180]. A more detailed summary of this work is presented in Chapter 2. In a periodic chain, resonators form part of the structural pathway (i.e., they are structurally embedded within the host structures), thereby limiting their potential in structural applications for improving the acoustic performance of lightweight systems. They are therefore considered outside the scope of this study. Only a very small amount of research has reported on nonlinear metamaterials employing non-structural resonators. Khajehtourian [181] examined longitudinal waves in a thin rod containing a series of spring-mass resonators with large elastic deformations inducing nonlinearity. Zhou et al. [127] investigated low-frequency attenuation in a beam with nonlinear, high-static-low-dynamic stiffness resonators attached.

A different approach employing multiple, nonlinear resonator attachments was reported by Fang et al. [15]. In that work, resonators comprised tuned cantilevers, orthogonally attached along the length of the host beam. Each cantilever supported a nonlinear magnetic spring with a coupled vibro-impact oscillator. With that configuration, broadband, low-frequency attenuation of transverse waves was achieved. Attenuation depth and nonlinearity both increased with the magnitude of the white noise input. The attenuated frequency band was shown to cover frequencies between two linear bandgaps – the first being associated with the laterally oscillating cantilevers and the second with the magnetic springs. This phenomenon was investigated further in [151] and referred to as ‘bridging-coupling’ in reference to the tendency for nonlinearity in the system’s response to cause two linear bandgaps to apparently ‘couple’ to form a wide attenuation band.

A similar design employing a nonlinear mechanical spring coupled with a vibro-impact oscillator was studied by Sheng et al. [16] using a model similar to that reported in [15]. The resonant frequency of the strut was found to have the largest effect on attenuation. However, the size of that effect could be explained by the relationship between that frequency and the upper bound of the frequency range of interest. As the frequency was increased, it approached the upper bound, thus increasing the portion of the frequency range covered by the attenuation band. Mean attenuation was therefore increased by broadening the attenuation band rather than deepening the attenuation. Other parameters tested included the excitation amplitude, nonlinear stiffness coefficients for spring and impact oscillation, linear resonant frequencies for strut and spring oscillation, oscillator mass and beam thickness were investigated.

Motivated by the metamaterial design in [15], this chapter reports on an experimental investigation that focuses on the effects of internal resonator parameters that relate to impact forces in the impact-oscillator. In [15], the impact-oscillator was identified as the largest source of nonlinearity. In this study, mechanisms by which that nonlinearity might be increased for small transverse vibration amplitudes in the host beam are investigated. The design incorporates a nonlinear magnetic spring coupled with a vibro-impact oscillator, and the effects of three key parameters (impact driving amplitude, impact gap and spring stiffness) on the attenuation performance of the nonlinear acoustic metamaterial are tested as part of a broader investigation into the underlying workings of this emerging area for improving structural-acoustic performance in lightweight buildings. The impact driving amplitude (IDA) is defined as the amplitude of lateral strut oscillation at the point of contact with the impacting resonator magnet. This varies with the distance from the base of the strut and is therefore controlled by varying the location of the contact. Both spring stiffness and impact gap also affect the peak forces driving the resonator to impact with the strut. The developed nonlinear resonators are mounted on a cantilevered aluminium beam, and vibration tests are conducted to examine the system's attenuation of transverse vibration in the 20 – 120 Hz frequency range. An aluminium cantilever is selected for use in this study for the degree of experimental control it affords over more complex structures and heterogeneous materials for which the system is ultimately being developed.

The rest of this chapter is organised as follows. The design of the nonlinear resonators is presented in the next section. Section 3.3 presents the experimental setup used in this study. Section 3.4 provides results and discussion on the performance of the proposed vibro-impact metamaterial design. Finally, conclusions are drawn in Section 3.5.

3.2 Design of nonlinear vibro-impact metamaterial

Figure 3.1 (a) illustrates the proposed application of nonlinear resonators for improving the acoustic performance of lightweight structures. An example of a resonator assembly is shown in Figure 3.1 (b). Each assembly comprises a 100mm long, 3.18mm diameter, 316 stainless steel cylindrical strut with two separated but magnetically aligned N42 neodymium ring magnets rigidly fixed along its length. Between the fixed magnets, a third, pole-reversed magnet is suspended and free to slide on the strut. Each strut is orthogonally attached to the beam via a threaded connection. The fixed magnets have an outer diameter of 7.5 mm, inner diameter of 2.5 mm and thickness of 3 mm. The suspended magnet resonator comprises three identical magnets held together as a single unit.

To illustrate the flow of energy within the system, consider a series of resonators attached to a vibrating, lightweight beam structure, as shown in Figure 3.1 (a). At the initiation of a structure-borne impact event, vertical translation, and rotation of the beam/strut junction

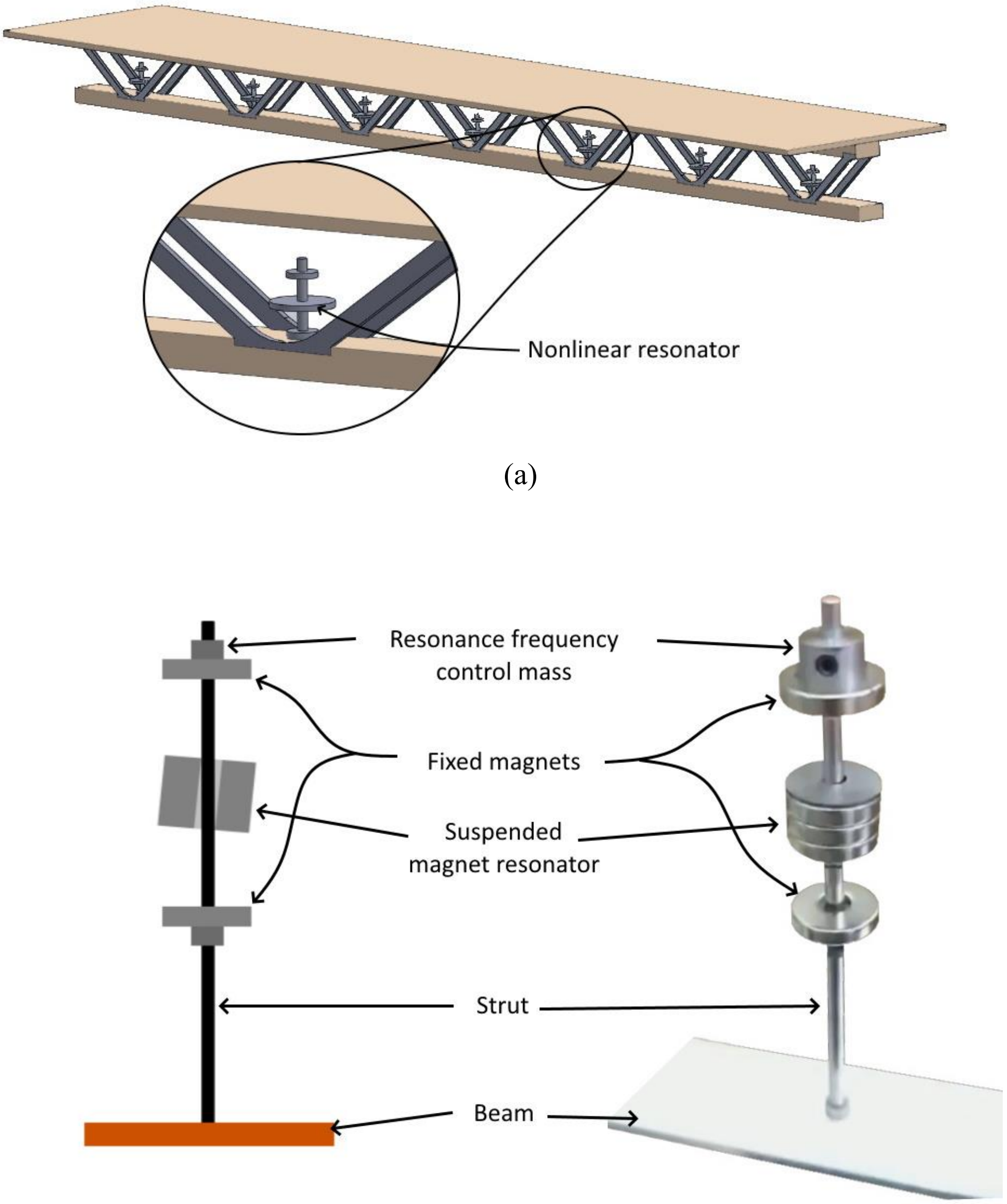

(a)

(b)

Figure 3.1 (a) The proposed application of nonlinear resonators for improving building acoustic performance; (b) Schematic and actual prototype of a nonlinear resonator investigated in this study.

impart energy into low-frequency, vertical oscillations of the magnetic resonator and lateral oscillations of the strut. The magnetic resonator also moves laterally, in unison with the oscillating strut until the magnetic torque holding it in place is overcome by the strut's acceleration. The nature and magnitude of this torque are discussed in detail below. Given sufficient excitation, the resonator, therefore, separates from the strut to become fully airborne, at which point it is acted on by magnetic forces alone.

Subsequent interactions between resonator and strut are characterised by highly nonlinear impact events. Each impact excites vibrations in the strut, imparting energy into high-frequency, transverse oscillations. The highest frequencies excited are determined by the contact duration of the impact event, which, in turn, is determined by the hardness of the impacting materials. Harder materials induce shorter contact durations which excite higher frequencies. A small percentage of the energy in each strut oscillation is dissipated by material damping. Energy in higher frequencies is dissipated more quickly due to the higher number of oscillations in any given period of time. A principal goal of the system's operation is, therefore, to impart as much energy into high-frequency strut oscillations as possible via impacts from the magnetic resonator. It is this aspect of the system's operation that this study focuses on.

Due to a tendency of the interacting magnetic fields to align the poles of the magnets, a magnetic torque acts on the suspended magnetic resonator such that it is rotated away from the orthogonal position until it makes contact with the strut (see Figure 3.2). This torque varies with the angle of rotation and can be approximated by considering the suspended magnet as a dimensionless magnetic dipole using the following relation:

$$|\boldsymbol{\tau}| = |\boldsymbol{m} \times \boldsymbol{B}| = |\boldsymbol{m}||\boldsymbol{B}| \sin\theta \tag{3.1}$$

where $\boldsymbol{\tau}$ is the torque acting on the suspended resonator magnet, $\boldsymbol{m}$ is its magnetization in units of NmT^{-1} (newton-metres per tesla), $\boldsymbol{B}$ is the magnetic field from the fixed magnets in units of T (tesla), and θ is the angle of rotation of the resonator magnet from orthogonal (i.e., the angle between the directions of the fields). The strength of this torque is, therefore, zero when the resonator magnet is orthogonally aligned (i.e., when the poles are perfectly opposed) and increases as the magnet rotates towards the strut. Note that the dimensionless dipole approximation requires that the magnetic field from the fixed magnets is constant across the volume occupied by the free magnet. This is a reasonable approximation for the region between two magnetically aligned permanent magnets.

Figure 3.2 shows a cross-section view of a suspended magnetic resonator in contact with a strut. At the onset of a vibration input, the resonator moves in unison with the cantilever’s lateral motions. The angle at which it rests against the strut is governed by the size of the gap between the two bodies and the thickness of the free magnet. This can

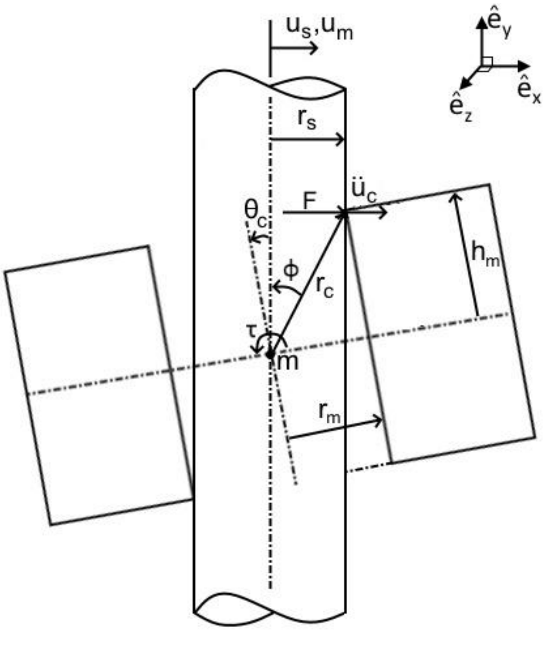

Figure 3.2 Cross-section view of interaction between strut and magnetic resonator prior to separation. u_s and u_m are the displacements of the strut and resonator centre of gravity (CG) respectively (these are identical prior to separation). r_s and r_m are the radii of the strut and resonator respectively, r_c is the distance of the contact point from the resonator CG, h_m is half the thickness of the resonator, ϕ is the angle of $\boldsymbol{r}_c$ from vertical, θ_c is the angle of rotation, from vertical, of the resonator when at rest, F is the magnitude of the force applied to the resonator by the strut, $\ddot{u}_c$ the lateral acceleration of the resonator contact point, τ is the magnetic torque applied about the resonator CG and m is the mass of the resonator which is represented in the equations of motion as a lumped mass located at the resonator CG

be calculated as the angle through which the line connecting the resonator CG and the contact point rotates between the orthogonal and resting positions.

$$\theta_c = \phi_o - \phi_c = \sin^{-1}(r_m/r_c) - \sin^{-1}(r_s/r_c), \qquad \left(r_c = \sqrt{r_m^2 + h_m^2}\right) \tag{3.2}$$

where, θ_c is the resting angle, φ_o and φ_c are the angles between the line connecting the resonator CG and the contact point when the resonator is in the orthogonal and resting positions, respectively, r_s and r_m are the radii of the strut and the hole in the magnetic resonator, respectively and r_c is the distance from the CG of the resonator to the contact point (see Figure 3.2).

This angle (θ_c) is important because it governs the threshold torque that must be overcome by the lateral acceleration of the strut to initiate vibro-impact-induced energy dissipation. It also governs the maximum strength of the torque that drives the impacts. If the angle is too large, small floor vibrations, though still problematic, will fail to initiate vibro-impact action. If the angle is too small, the magnetic torque remains too small to rotationally accelerate the free magnet sufficiently for effective high-frequency excitation of the strut.

The size of the impact gap was controlled by varying the hole diameter in laser-cut steel rings that were adhered to the top and bottom surfaces of the resonator magnets. During vibration, it was the inner edges of those rings that made contact with the strut. Two impact gap sizes were tested: 0.57 mm (referred to as the large gap (L-G) condition) and 0.17 mm (referred to as the small gap (S-G) condition) as presented in Figure 3.3.

Prior to separation, since there is no angular acceleration, the acceleration of the resonator's centre of mass ($\ddot{\boldsymbol{u}}_m$) is equal to that at the contact point ($\ddot{\boldsymbol{u}}_c$). Therefore, the

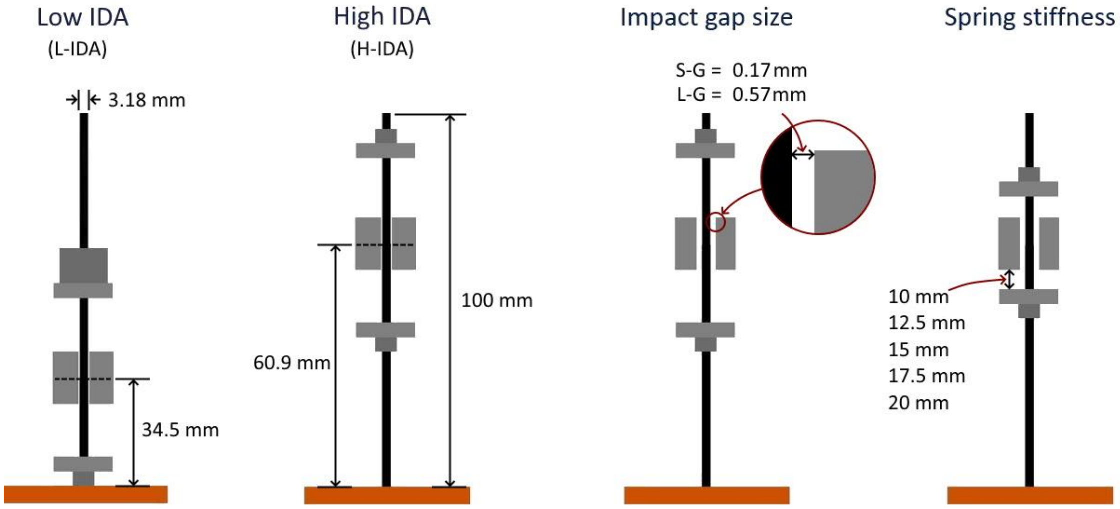

Figure 3.3 An illustration of varied resonator configuration parameters: low/high impact driving amplitude (IDA), small/large impact gap (S-G = 0.17 and L-G = 0.57 mm) and spring stiffness (governed by spring gap range of 10-20 mm, varied at 2.5 mm intervals).

force applied to the resonator due to its inertial resistance to linear acceleration is given by:

$$\boldsymbol{F} = m\ddot{\boldsymbol{u}}_c = m\ddot{u}_c\hat{\boldsymbol{e}}_x \tag{3.3}$$

and the torque which acts about its centre of mass is given by:

$$\boldsymbol{T} = \boldsymbol{r}_c \times \boldsymbol{F} = r_c\big(\cos(\phi)\,\hat{\boldsymbol{e}}_y + \sin(\phi)\,\hat{\boldsymbol{e}}_x\big) \times m\ddot{u}_c\hat{\boldsymbol{e}}_x = m\ddot{u}_c r_c\cos(\phi)\,\hat{\boldsymbol{e}}_z \tag{3.4}$$

where $\boldsymbol{F}$ is the inertial reaction force at the point of contact due to the acceleration ($\ddot{\boldsymbol{u}}_c$), m is the mass of the magnetic resonator, $\boldsymbol{T}$ is the resulting torque applied to the resonator about its centre of mass, $\boldsymbol{r}_c$ is the vector from the CG of the resonator to the contact point and $\phi = \sin^{-1}(r_s/r_c)$ is the angle of $\boldsymbol{r}_c$ from vertical (see Figure 3.2). Here, $\hat{\boldsymbol{e}}_i$ is used to denote the unit vector in the i direction.

Therefore, the magnitude of the acceleration necessary to induce separation of the resonator from the strut is given as:

$$\ddot{u}_{c(threshold)} = \tau_c/(mr_c\cos(\phi)) \tag{3.5}$$

where τ_c is the magnitude of the magnetic torque acting on the resonator when at rest.

This result was used to select the range of impact gap sizes to be tested. Simulation of the elastic structure estimated acceleration at the point of contact between the strut and resonator for input levels approximating those for the experimental setup. Equation (3.5) was then used to calculate the desired range of angles and, finally, the dimensions of the resonator relative to those of the strut. The small and large impact gap sizes that have been selected are expected to result in strut-resonator separation at low and medium input levels, respectively.

Another important factor governing the degree to which vibro-impact interactions are excited is the height of the impact locations above the base of the strut. This is because the amplitude of the strut's fundamental mode shape increases with the distance from its base. Therefore, by moving the suspended magnet closer to the top of the strut, the impact driving amplitude (IDA) is effectively increased. To compensate for the effect this has on the natural frequency of the strut's lateral motion, the mass of the retainer used to hold the upper magnet in place is set so that the natural frequencies are the same for both high and low IDA conditions.

Finally, by altering the distance between the fixed magnets, the linearized natural frequency of the magnetic spring can be controlled. This is important because previous research has shown that this frequency governs the lower end of the attenuated frequency band [151]. Each fixed magnet pair is therefore separated by a carefully measured distance which is varied in 5 mm increments from 29 mm to 49 mm. This results in a gap between the resonator surfaces and the fixed magnets of between 10 and 20 mm. For this study, spring stiffness variations are therefore referenced by the size of this gap, and the full range of tested spring stiffnesses corresponds to gaps of 10, 12.5, 15, 17.5 and 20 mm (see Figure 3.3).

Based on the underlying mechanisms of the nonlinear resonators presented above, three governing parameters for resonator configurations, including impact driving amplitude (IDA) factor, impact gap size factor and spring stiffness factor, are experimentally investigated in the following sections.

3.3 Experimental program

In order to investigate the effects of selected design parameters on the proposed nonlinear metamaterial (the IDA, the impact gap size, and the spring stiffness), a series of experiments was carried out in which aluminium cantilever beams with attached resonators (so-called metabeams) were vibrated at one end as shown in Figure 3.4.

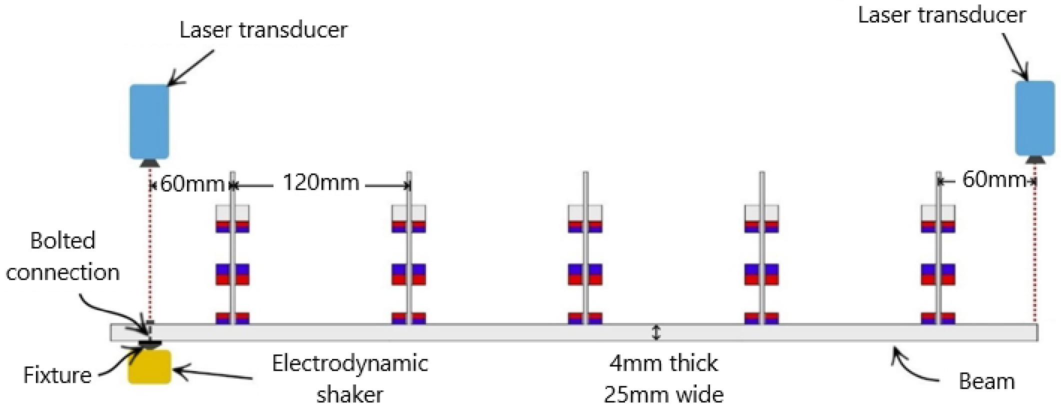

Figure 3.4 Experimental metabeam setup for five-resonator beam.

Each experimental beam comprised a 600 x 25 x 4 mm aluminium base beam with five resonator assemblies attached at 120 mm spacings, as shown in Figure 3.4. The vibration source was an electrodynamic shaker fabricated from a modified subwoofer speaker connected to an amplifier. The signal source was a pink noise, 0-200 Hz frequency band .wav file generated by the software, Room EQ Wizard v5.19. For the experiments, the file was played by a digital audio player connected to the amplifier input. The beam was bolted to an aluminium fixture which was rigidly attached to the top surface of the shaker armature. Vertical displacement was measured at each end of the beam to determine the attenuation performance for a range of resonator configurations, as shown in Figure 3.3. Synchronised, 2.5 kHz sampling-rate laser transducers were positioned above each end of the metabeam to measure vertical displacement. Each measurement comprised 20,000 samples recorded at 400 μs intervals. By measuring the beam's displacement at the input point, fine control of the amplitude and frequency of input is possible.

For each metabeam (MB) configuration (see Table 3.1), a reference beam (RB) for which the mass of each resonator was replaced with an equivalent lumped mass was also tested (see Figure 3.5). Reference beams, therefore, had equivalent mass, mass distribution and stiffness to the corresponding experimental metabeams but no internal, localised resonance effects. As a result, reference beams can be used to benchmark the performance of the proposed nonlinear acoustic metamaterials. Table 3.1 presents a summary of the metabeams (with the corresponding design parameters) examined in this study.

Table 3.1 Summary of experimental metabeam configurations tested in this study.

Design parameters	Conditions/Values
Impact Driving Amplitude (IDA) factor	[Low IDA, High IDA] (see Figure 3.3)
Impact gap size factor	[0.17 mm (S-G); 0.57 mm (L-G)]
Spring stiffness factor	Corresponding to spring gap sizes of [10.0, 12.5, 15.0, 17.5, 20.0] mm

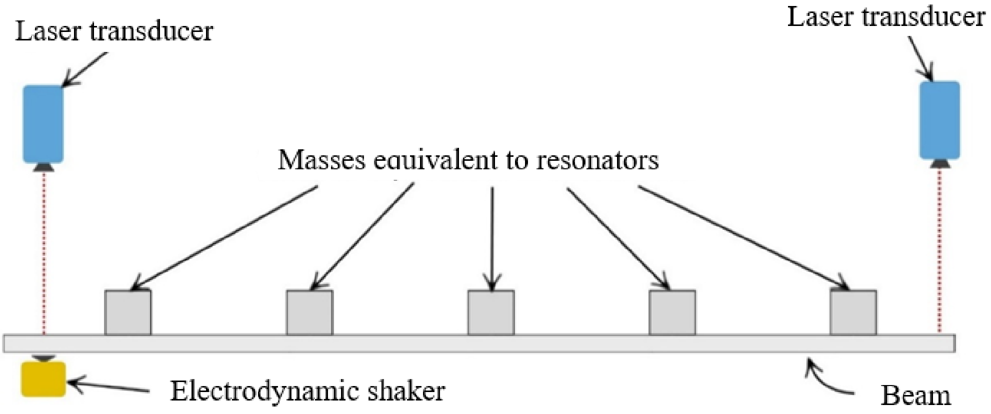

Figure 3.5 Reference beam with equivalent lumped masses replacing the mass of each resonator.

Each configuration was measured for five different input magnitudes. Those were controlled via the amplifier output level, which was indicated by an in-built digital readout. Amplifier output levels of -20, -25, -30, -35 and -40 dB were used for each configuration measurement. Those corresponded to RMS vibration response amplitudes at the input end of the reference beam of 0.167, 0.096, 0.055, 0.031, and 0.009 mm respectively. Subsequent modelling (see Chapter 4) has shown that those response amplitudes correspond to mean (RMS) input forces of 670, 386, 222, 124, and 37 N respectively. For readability, the amplifier output levels quoted above are used to identify the individual input levels in this chapter.

To eliminate interference from external vibration, an arrangement of masses, resilient rubber pads and elastic cords was constructed to isolate the transducers and the elastically supported prototype beam end from vibration noise induced by the shaker and from the environment. A schematic of the vibration isolation apparatus is shown in Figure 3.6, and a photo of the actual assembly is shown in Figure 3.7.

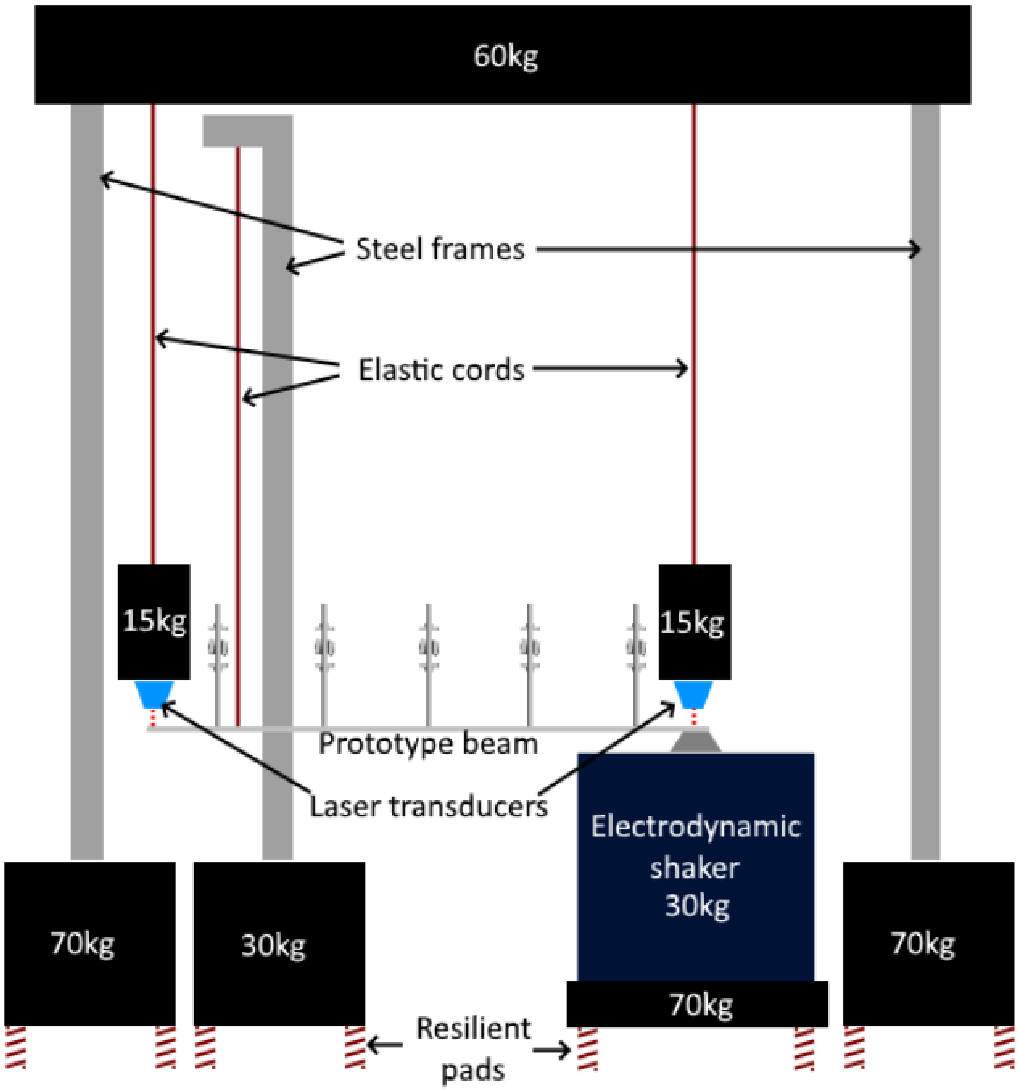

Figure 3.6 Schematic showing the arrangement of components used to isolate the laser transducers and the elastic cords used to support the free end of the prototype cantilever beam.

In the setup, the electrodynamic shaker box is filled with sand and mounted on a 70 kg steel block which is, in turn, mounted on four resilient rubber pads (60 x 60 mm base x 100 mm high). The laser transducers are mounted on 15 kg steel masses suspended from long elastic cords and supported by soft foam damping pads. The elastic cords are attached to a frame which is also mounted on a 70 kg steel mount which is, in turn, mounted on rubber pads. The foam damping pads shown in the photo of Figure 3.7 are used to reduce tiny motions of the transducer mounts caused by air movement. The natural frequency for vertical motion of these plates is measured to be approximately 3 Hz. The

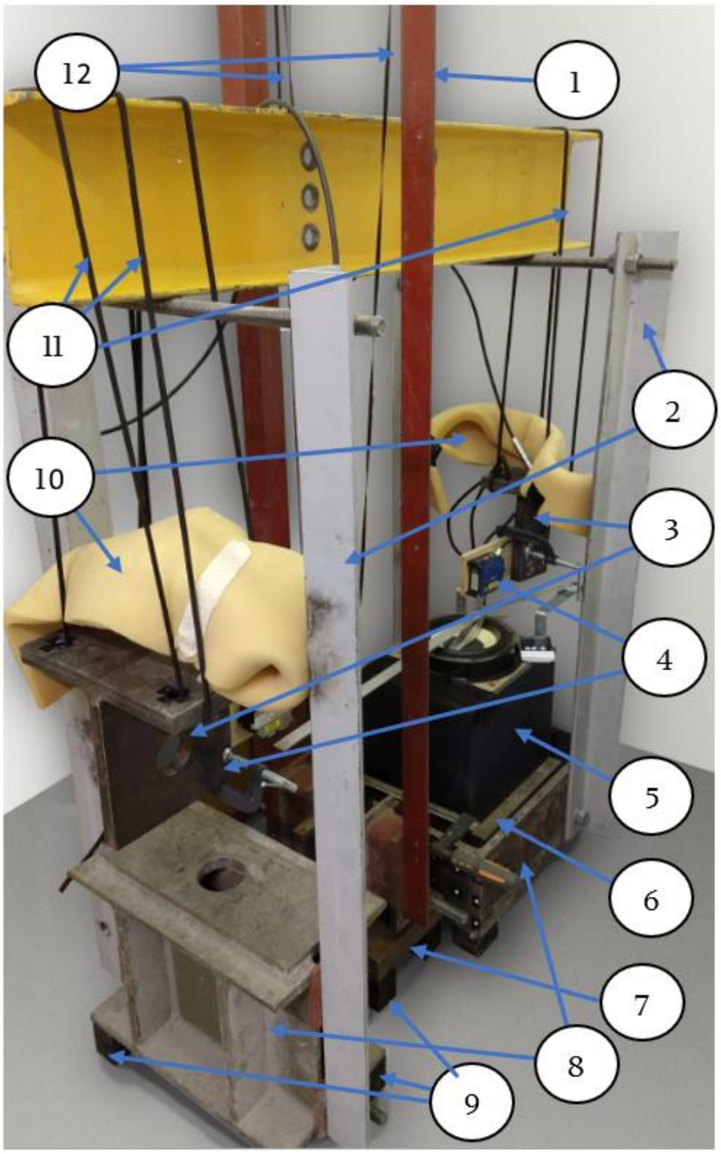

1. Support frame for elastic end support for cantilever beam
2. Support frame for laser transducer
3. Suspended laser transducer mounts
4. Laser transducers
5. Electrodynamic shaker
6. Base mass for electrodynamic shaker
7. Base mass for support frame for cantilever elastic end support frame
8. Base masses for laser transducer support frames
9. Resilient rubber pads
10. Foam dampers for transducer mounts
11. Elastic supports for transducer mounts
12. Elastic supports for cantilever end

Figure 3.7 Photograph of the actual vibration isolation assembly

amplitude of transducer vibration with and without the shaker in operation was measured to be less than 3.6 μm.

To limit the torque applied to the armature of the shaker by the weight of the prototype beam assembly, the free end of the beam is supported by long, light-weight elastic cords suspended from another independently mounted isolation frame. The tension on the cord was set so that the end of the beam was always at the same height prior to vibration input being applied (as measured by the laser transducer, which remained in place between configuration changes). Residual vibration at the end of the beam, in the absence of vibration input, was also measured to be less than 3.6 µm.

Temperature and humidity were recorded before and after each experimental run. The temperature ranged between 19.7 and 20.2°C, and relative humidity was between 35 and 40% throughout the experiments. This eliminated any possibility that experimental measurements were affected by large variations in those parameters.

3.4 Results and discussion

This section presents experimental results for the effect of nonlinear resonators on the vibrational behaviour of the metabeams, beginning with an overview of the best performing configurations and then examining the effects of each investigated parameter.

The largest mean amplitude reduction was achieved by the configuration with high IDA, high spring stiffness and small impact gap (S-G). That configuration had a 10 mm gap between the surfaces of the resonator and fixed magnets – the smallest of the gaps tested and, therefore, the highest spring stiffness (see Figure 3.3). Figure 3.8 (a) compares the displacement time history for that configuration with those of the corresponding large impact gap (L-G) condition and reference beam for amplifier input level -20 dB (the highest tested level). Both metabeam configurations produce a significant reduction in vibration relative to the reference beam. In terms of mean amplitude (RMS) reduction, the small gap condition outperforms the large gap condition with a mean amplitude reduction of 65% versus 55%.

For low IDA configurations, the lowest spring stiffness (with a spring gap of 20 mm) showed the most effective attenuation for both large and small impact gap conditions. Figure 3.8 (b) shows the same results for low IDA, 20 mm spring gap configurations. Again, the small gap condition outperforms the large gap condition in terms of mean

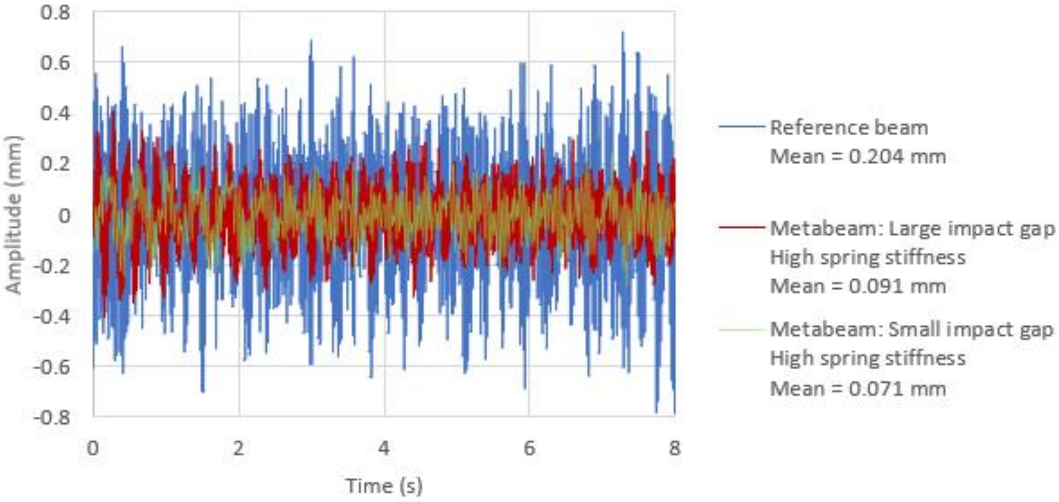

(a) High IDA case

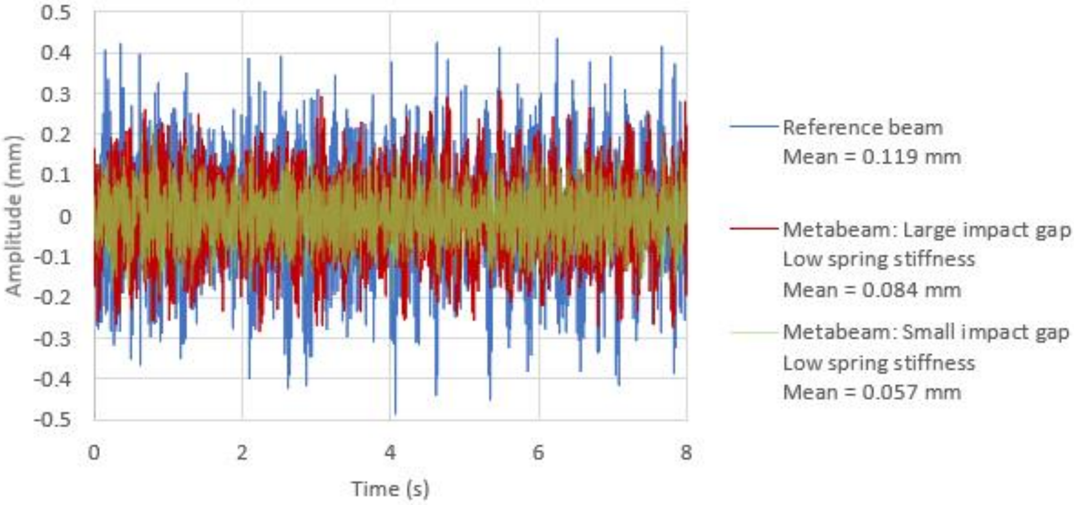

(b) Low IDA case

Figure 3.8 Comparison of the vibration amplitude time series for reference beams and metabeams with large and small impact gaps for (a) High IDA cases stiffness and (b) Low IDA cases. The best performing spring stiffness is shown for each case (high stiffness for high IDA and low stiffness for low IDA).

amplitude (RMS) reduction with a 52% improvement versus 29%.

Figure 3.9 presents frequency spectra for the vibration amplitude at the output end of reference and metabeams in the frequency range of interest (20 – 120 Hz). Significant attenuation of resonance peaks is being achieved for both high and low IDA cases. It is noted that the reference beam amplitude for the low IDA case is significantly smaller than that of the high IDA case. This demonstrates the attenuation effect of the additional mass added to that beam and shows that the level of attenuation achieved by the nonlinear resonators is significantly greater than that achieved by the addition of mass alone.

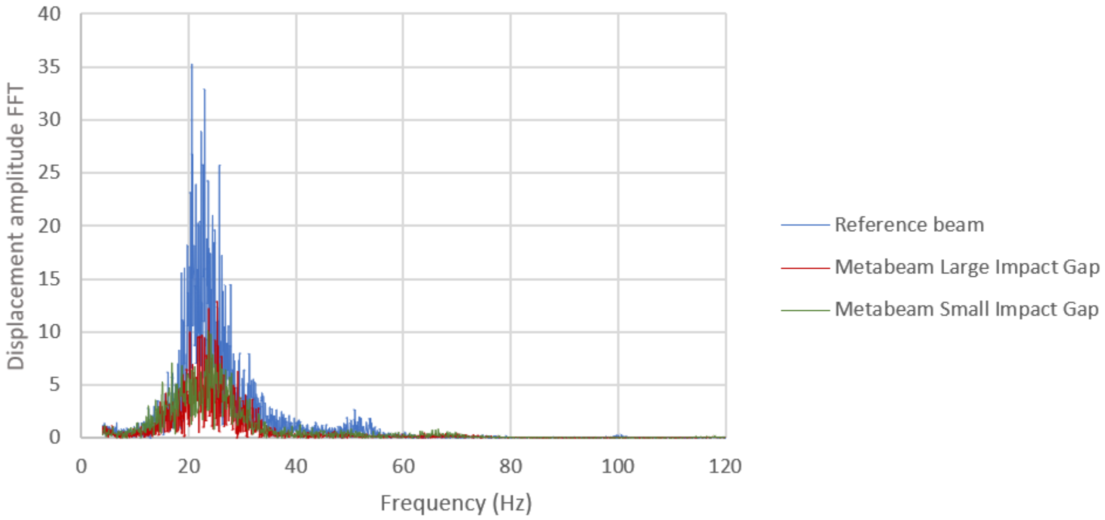

(a) High IDA case

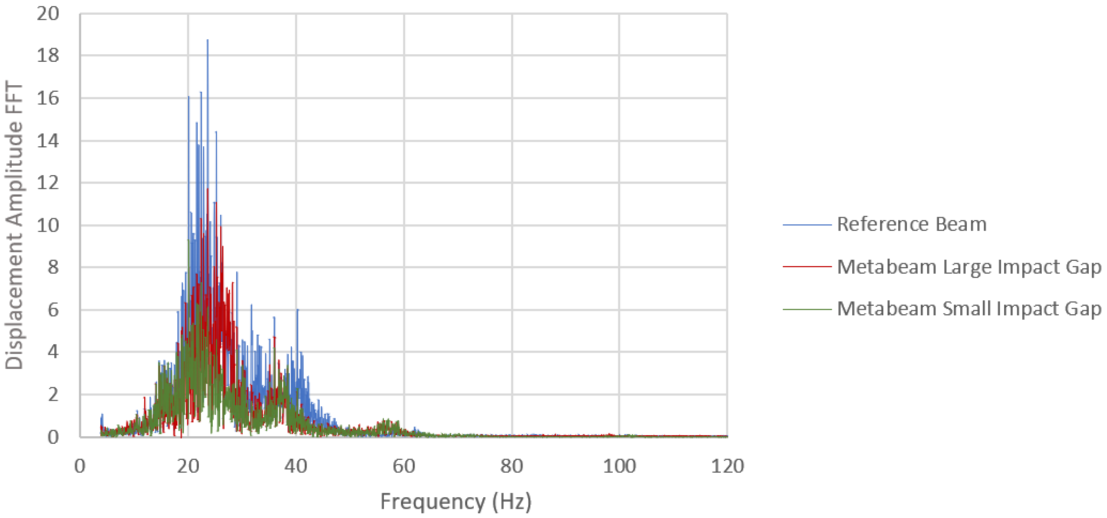

(b) Low IDA case

Figure 3.9 Comparison of output end displacement frequency spectra for reference beams and meta-beams with large and small impact gaps. (a) High IDA case and (b) Low IDA case. The best performing spring stiffness is shown for each case (high stiffness for high IDA and low stiffness for low IDA).

A common factor among the best performing resonator configurations is a tendency to promote high levels of vibro-impact excitation. The conditions for such excitation and experimental evidence for its importance in achieving the broadband attenuation seen in these resonators are discussed in the following sections.

3.4.1 Effect of magnetic spring stiffness

To demonstrate the effectiveness of the system relative to the reference beam across the full frequency range of interest (20-120 Hz), a decibel scale ‘vibration attenuation spectrum’ is defined here as the log ratio of metabeam to reference beam displacement frequency spectrum according to the following equation:

$$y = 20log_{10}\left(\frac{fft_{MB}}{fft_{RB}}\right)(dB) \tag{3.6}$$

Frequency spectra are calculated using a windowed fast Fourier transform. Figure 3.10 shows attenuation spectra for the range of tested spring stiffnesses for the high IDA, large impact gap condition (H-IDA_L-G). The best vibration attenuation for the frequency range of interest (averaged over 20 – 120 Hz) is 8.41 dB for the highest spring stiffness, as depicted in the left-most sub-plot of Figure 3.10. The mean attenuation decreases as

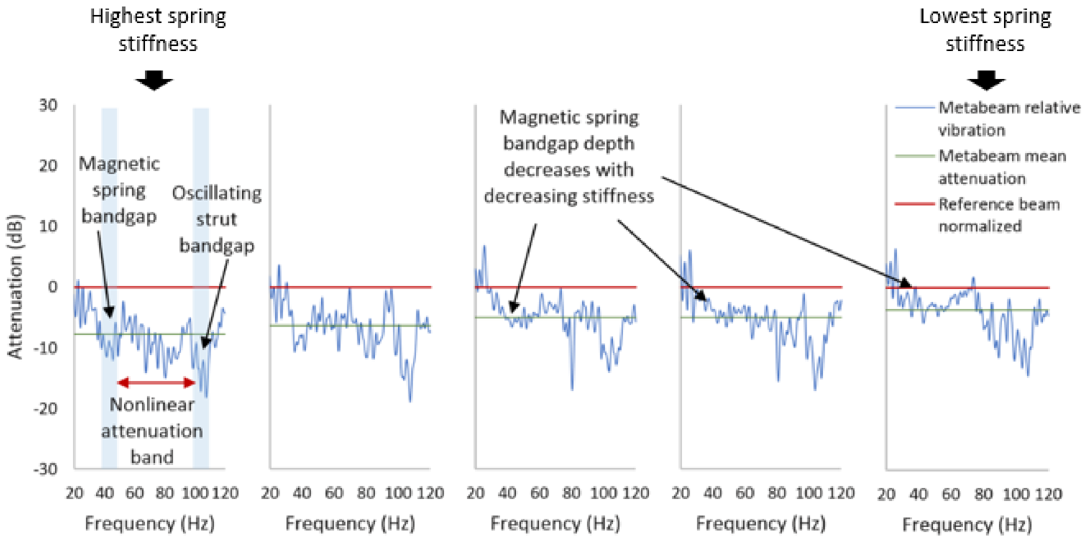

Figure 3.10 Spring stiffness variations: Attenuation spectra for High IDA, large impact gap - 20dB input. Spring stiffness decreases from left to right: Spring gap from left to right = 10, 12.5, 15, 17.5 & 20mm

the spring stiffness decreases. Further, a nonlinear attenuation band is observed between the linear bandgaps corresponding to resonances in the magnetic spring and the laterally oscillating strut.

Two factors contribute to the association between spring stiffness and attenuation. Firstly, as the spring stiffness decreases, the amplitude of the oscillating magnetic spring force decreases. This coincides with a decrease in the depth of the linear bandgap associated with the magnetic spring, as can be seen in Figure 3.10. Secondly, as the spring stiffness increases, the magnetic torque tending to rotate the impacting resonator towards contact with the strut also increases. This results in an increase in the impact forces that drive vibro-impact excitation. As a result, better attenuation is observed for the higher spring stiffness. However, it is also noted that the higher magnetic torque produced by higher spring stiffness means that the resonator won't start impacting until the driving vibration exceeds the threshold for vibro-impact excitation. In Section 3.4.3, it will be seen that this reduces the attenuation of the resonator system for smaller inputs. This is described mathematically in equations (3.3) and (3.4) in Section 3.2 and is discussed further in Section 3.4.3.

3.4.2 Effect of impact gap size

The size of the impact gap also affects the magnetic torque because a larger gap leads to a larger angle to which the resonator can rotate before impacting with the strut. Therefore, the maximum torque will be larger (see equations (3.3) & (3.4)). A larger impact gap will therefore necessitate higher input levels to initiate separation of the resonator from the strut. It will also cause larger impact forces once impact-oscillation is initiated. Configurations with larger impact gaps are, therefore, expected to require larger vibration inputs to initiate impact oscillation and to produce more effective attenuation once it is initiated.

This is supported by the results shown in Figure 3.11 which compares attenuation spectra for decreasing input levels (-20, -25, -30, -35 & -40 dB) for (a) large gap, and (b) small gap conditions. As expected, the best-recorded performance in terms of broadband attenuation was achieved by the metabeam with high IDA and large impact gap configuration (MB_H-IDA_L-G_10). For both large and small impact gap sizes, a deep

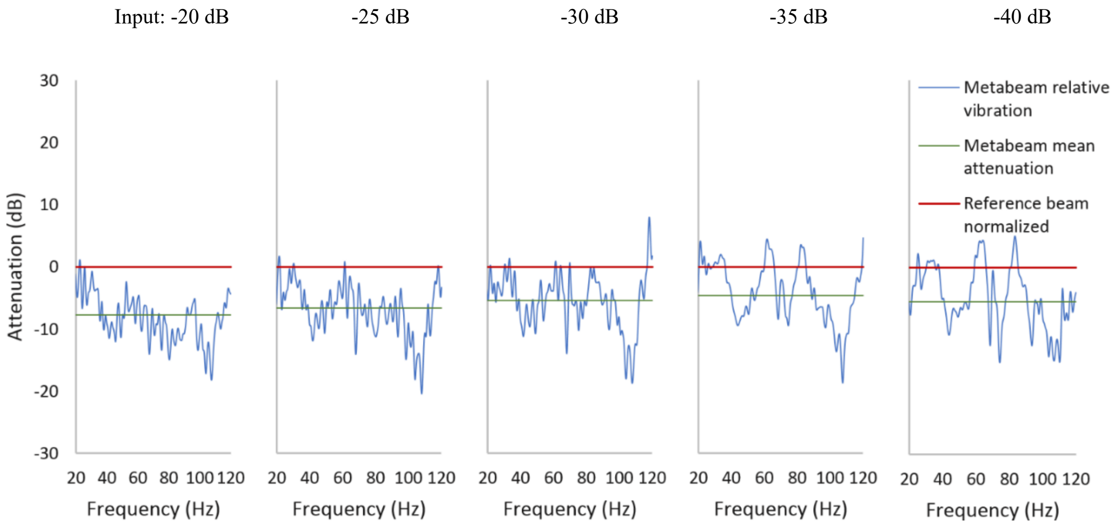

(a) Large impact gap

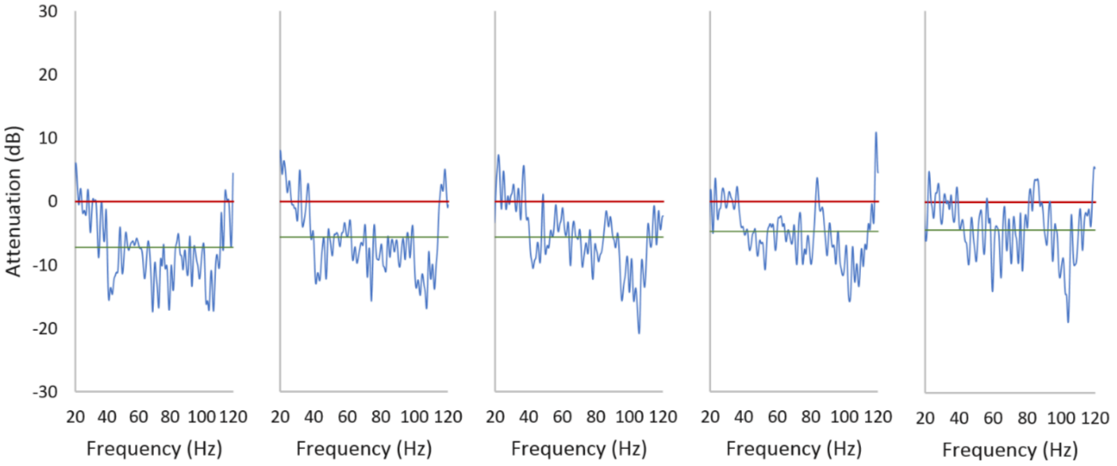

(b) Small impact gap

Figure 3.11 Input level variations: Attenuation spectra for (a) large impact gap vs (b) small impact gap configurations all with high IDA and 10mm spring stiffness. From left to right: input level = -20, -25, -30, -35 & -40 dB nonlinear attenuation band is observed for the highest input level (-20 dB). Then, as the input level decreases, so does the attenuation. Dense resonance peaks begin to form for the large impact gap condition but not for the small gap condition. This suggests that the system continues to exhibit vibro-impact-driven attenuation even for the lowest input levels when the impact gap is small due to the lower threshold for vibro-impact excitation. However, it is also observed that the mean attenuation decreases as the input level decreases for the small gap condition. This may be attributable to the fact that the small input level is closer to the threshold, thereby weakening the effectiveness of vibro-impact excitation.

3.4.3 Effect of input amplitude

By increasing the input amplitude, both the vertical spring motion of the resonator and the lateral oscillation of the strut is increased. These motions are primary contributors to the nonlinearity of the system's response – vertical spring motion because the magnetic spring is nonlinear, and lateral strut motion because impact-oscillation is driven by it. Figure 3.11 also shows that the depth of attenuation in the target frequency range increases with increasing input amplitude. This is a widely recognised feature of nonlinear attenuation systems. As has already been discussed in relation to the effects of impact gap size, for low input amplitudes, dense resonance peaks appear in the attenuation band, particularly for the large impact gap condition, suggesting that attenuation performance decreases as the conditions for vibro-impact behaviour are decreased. This is an observation that formed the basis for testing the effect of impact driving amplitude.

3.4.4 Effect of impact driving amplitude (IDA)

Finally, the effect of impact driving amplitude (IDA) on the observed results is considered. As has already been noted, the best performing configurations were those with a higher driving amplitude. This condition is expected to produce higher levels of vibro-impact excitation. Figure 3.12 shows vibration attenuation spectra for low IDA and high IDA, large impact gap, 10mm spring gap configurations. A large linear bandgap coinciding with the fundamental frequency of lateral strut oscillations is evident, along with a low level of vibro-impact effect in the frequencies ranging down to the second, resonator-induced linear bandgap. The greater depth of the low IDA linear bandgap can be explained by the larger mass of the upper fixed magnet retainer compared with that of the high IDA configurations. The low level of vibro-impact induced attenuation can be understood in terms of a combination of the low impact driving amplitude and the large impact gap, both of which tend to increase the threshold for vibro-impact excitation. It is, therefore, evident that observed attenuation spectra reflect deep attenuation in narrow frequency bands due to linear oscillations with a low level of vibro-impact-induced broadband attenuation.

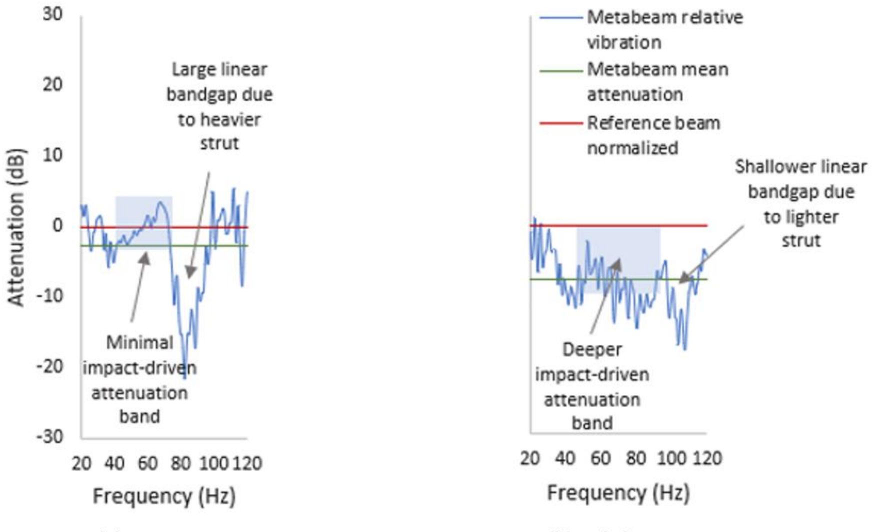

(a) Low IDA (b) High IDA

Figure 3.12 Attenuation spectra for (a) Low IDA vs (b) High IDA, both with large impact gap, 10mm spring and -20dB input. The low IDA configuration shows minimal impact-driven attenuation due to its higher input vibration threshold for initiating impact excitation.

3.5 Conclusions

In this study, a nonlinear metamaterial design for the attenuation of low-frequency vibration in the 20 – 120 Hz frequency range is investigated. The design employs multiple nonlinear vibro-impact-based resonators to absorb, counteract and dissipate low-frequency vibration energy from the host structure. Previous work in the literature has shown that the depth of attenuation in the target frequency range depends on the degree of nonlinearity in the response. In this study, experiments are conducted on a small-scale lightweight beam prototype with a series of developed nonlinear resonators attached to examine the effects of three key design parameters that are considered critical to the generation of nonlinearity, namely: impact driving amplitude, impact gap size and spring stiffness.

The study found that a common factor for improved attenuation performance among the designs was a tendency to exhibit high levels of vibro-impact excitation. The effective impact driving amplitude, which can be controlled by varying the height of the magnetic spring resonator assembly above the host beam, was shown to increase vibro-impact excitation. Impact gap size and magnetic spring stiffness were found to increase the potential intensity of vibro-impacts, but also the amplitude of the input vibration needed to initiate them. Both these effects were shown to be due to an increase in the magnetic torque that drives the resonator's impact-inducing rotation. This demonstrates the potential for such resonators to be tuned to attenuate a wide but targeted range of input magnitudes by balancing magnetic spring forces with structurally amplified driving amplitudes.

In this study, the best attenuation performance of the proposed vibro-impact resonant metamaterial design was achieved by the high impact driving amplitude, large impact gap, high spring stiffness configuration for which the mean vibration attenuation for the full, low-frequency range of interest (20 – 120 Hz) was 8.41 dB. The results suggest that the nonlinear vibro-impact metamaterial design has the potential to be successfully applied to lightweight structures for improving structure-borne sound performance.

Chapter 4. Model development and validation

4.1 Introduction

In the previous chapter, the potential of the developed nonlinear vibro-impact resonators to improve structure-borne sound performance in timber structures was demonstrated. The experiments conducted highlighted complex behaviours and revealed the effects of several design parameters, including impact driving amplitude, impact gap size and spring stiffness, on system performance. To investigate further, there is a need to develop a numerical model to simulate the system's dynamic behaviour. In this chapter, the development and validation of a numerical model for the transient dynamic simulation of a metabeam structure comprising multiple highly nonlinear resonators are described. The model is developed in Python and implements a linear elastic frame structure comprising two-dimensional Euler-Bernoulli beam elements. The frame supports multiple resonator assemblies comprising magnetic springs with suspended magnet resonators that double as vibro-impact oscillators.

Previous work has shown that metamaterial systems comprising multiple, coupled, nonlinear, vibro-impacting resonators, as shown in Figure 4.1, can attenuate broadband low-frequency vibration in lightweight structural beams more effectively and with less additional mass than previous attenuation technologies. This has been reported by Fang et al. [15] and Sheng et al. [16] and was also shown experimentally in Chapter 3 of this thesis. In this system, each resonator comprises an orthogonally attached metallic cantilever supporting a magnetic spring resonator aligned along its length. In response to beam vibrations, the resonators exhibit three distinct internal patterns of oscillation:

- Lateral oscillations in the cantilever caused by rotation of the beam/strut junction,
- Vertical oscillations in the suspended magnet caused by vertical translation of the beam/cantilever junction, and
- Vibro-impact oscillations between the suspended magnet and the cantilever, driven by lateral oscillations of the cantilever and magnetic torque acting on the magnet.

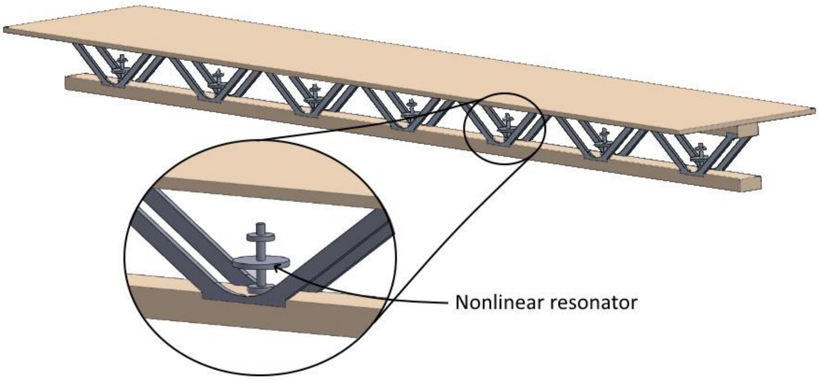

(a)

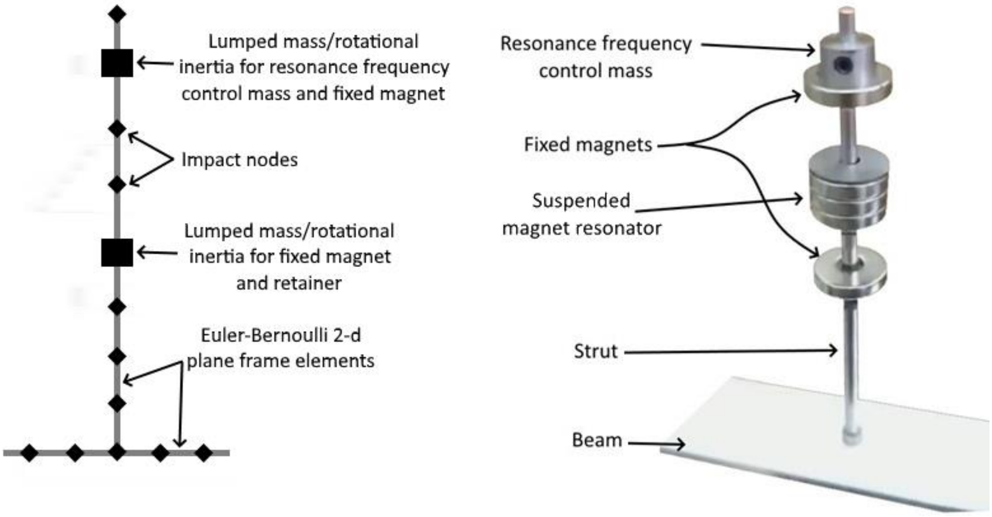

(b)

Figure 4.1 (a) Illustration of a proposed application of nonlinear resonators for improving building acoustic performance; (b) Schematic of the finite element implementation of a nonlinear resonator investigated in this study alongside a photograph of a physical prototype. Details of the implementation of the elastic structure shown on the left are described in Section 4.2.2 and further details of the use of the impact nodes to derive the contact locations in the 2-d structure are described in Section 4.2.3 and Figure 4.4

This combination has been shown to create a broad and deep attenuation band that can be targeted to different frequency ranges by tuning the natural frequencies of the cantilever and magnetic spring. Nonlinearity in the response contributes to the formation of an attenuation band spanning between those two frequencies. The vibro-impacting magnet, coupled with nonlinear magnetic spring oscillations, have been shown to be responsible for the system's nonlinearity and the depth of the attenuation increases with the amplitude (and therefore nonlinearity) of the response.

To model a version of this system, Fang et al. [15] used the harmonic balance method to solve a system of nonlinear differential equations of motion. In that model, the structure was simplified significantly. Lateral cantilever motion was modelled as a single degree of freedom mass-torsion spring system, and both vertical resonator motion and impact interactions between resonator and cantilever were modelled as hardening nonlinear springs. Higher vibration modes in lateral cantilever oscillations, rotation of magnetic resonators and effects of magnetic torque on resonator dynamics are therefore neglected. A similar model was used in [16], wherein both harmonic balance and transient time-domain methods were used for solution. This approach has made it possible to efficiently investigate the effects of parameters in systems that employ nonlinear coupling to induce very wide attenuation bands in this way. In reality, the motions of the suspended magnetic resonator are much more complex. Impact dynamics are dominated by rotations driven by a magnetic torque which results from interaction between the opposing magnetic fields. Thus, while the simplified model affords valuable insights into the nonlinear dynamics of the system, it does not account for the internal motion of the real physical system. To enable the design of such systems for construction applications, a simulation tool that captures the behaviour of the real physical system is needed to enable parametric studies that reveal relationships between physical dimensions.

The broader aim of this research is to develop a detailed understanding of the inner workings of this type of resonator, with a view to enabling the design of real-world systems capable of attenuating broadband, low-frequency vibration in lightweight building floor structures. A key challenge in simulating this system, therefore, arises from a need to simulate a large number of low-velocity[6] impacts in a short period of time. It is essential that an accurate, efficient simulation of resonator dynamics and strut response is achieved using an approach that solves in a reasonably short time. To achieve this, the developed model employs rigid body dynamics and an experimentally derived magnetic force-displacement curve to simulate the motion of resonators under the influence of magnetic forces. Impact interactions between resonator and structure are modelled using Hertzian contact mechanics.

Validation is undertaken in a staged process wherein individual components and component interactions are validated against experimental data and high-resolution finite element substructure models and progressively built up into the final model. The model is shown to simulate individual low-velocity impacts and two-dimensional resonator motion accurately. Furthermore, it achieves a high level of correlation with experimental results for attenuation at the highest tested input levels and effectively predicts the broadband attenuation in the same frequency range as is shown by experimental results but tends to overestimate the effect of lateral strut oscillation.

---

[6] Stronge's definition is used here [182]. According to Stronge, low-velocity impacts are those that result in "contact pressures that cause small deformations only; these are significant solely in a small region adjacent to the contact area". For metals, velocities on the order of 10 – 100 m/s are required to produce plastic deformations sufficient to define an impact as high-velocity. Testing in the model presented in this chapter has shown that peak relative velocities of the impacting bodies are on the order of 1 m/s.

4.2 Model development

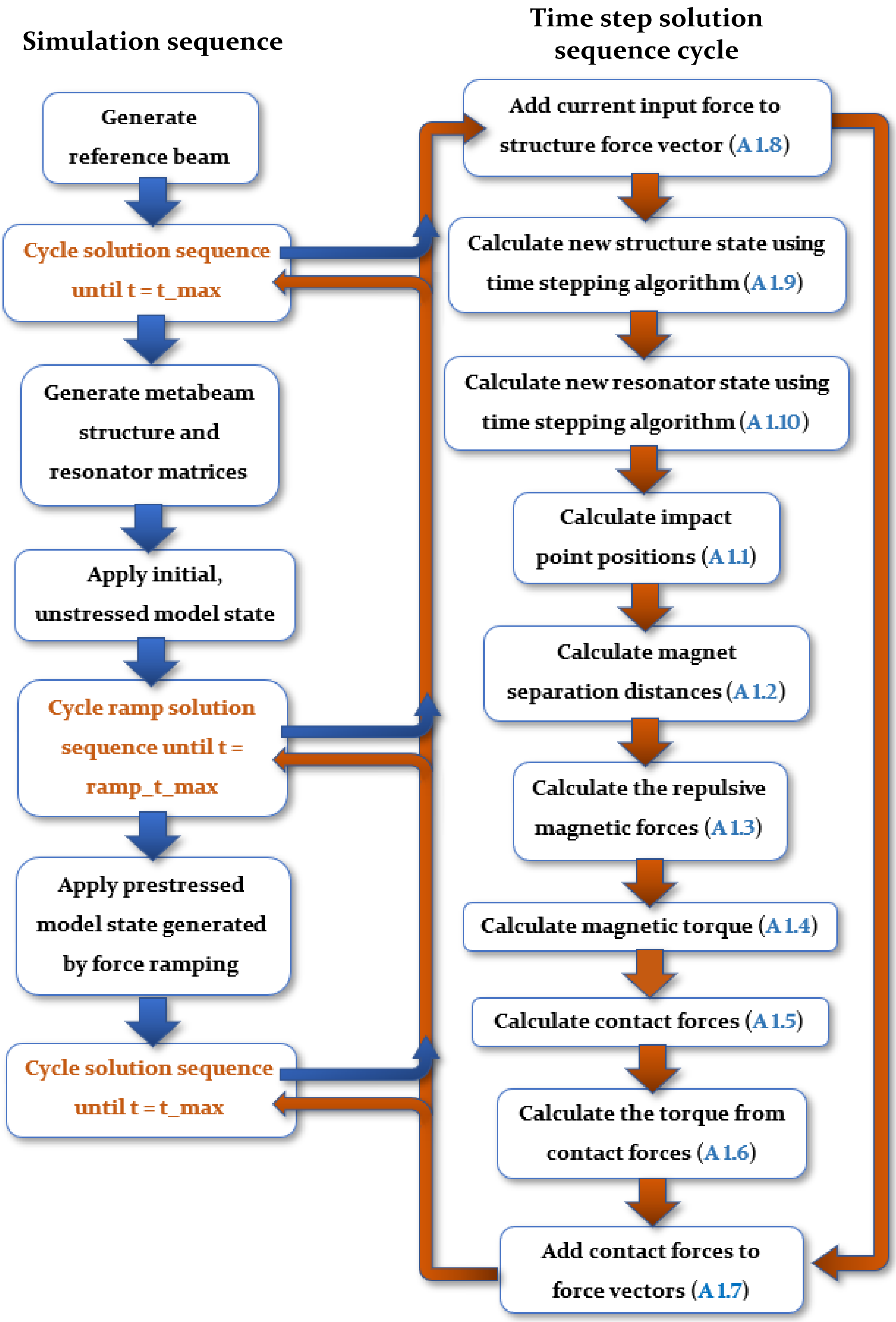

Figure 4.2 Flow chart showing an overview of Python code solution sequence. References shown in blue are to the relevant section in Appendix 1, where a segment of the actual code is shown.

4.2.1 Overview

A broad overview of the solution sequence carried out during a simulation is shown in the flow chart in Figure 4.2. It can be seen that the sequence first carries out a simulation for a reference beam which is a beam in which the resonators of the metabeam are replaced by lumped masses (see Section 4.3.3). Then the sequence calculates an initial prestressed state for the system (see Section 4.2.4) before simulating the metabeam itself. Relevant code segments, included in Appendix 1, are referenced in blue Figure 4.2.

Four broad categories of motion need to be addressed for the system’s behaviour to be captured effectively – 1.) the elastic behaviour of the continuous structure comprising the host-beam, struts, and fixed magnets, 2.) the vertical magnetic spring dynamics driven by coupling between the free and fixed magnets due to magnetostatic repulsion, 3.) rotation dynamics of the suspended magnet driven by magnetic torque and, 4.) the impact dynamics of the resonator magnet and strut.

The model design takes advantage of essentially linear aspects of the system. For the input amplitudes of interest, the behaviour of the continuous structure is in the linear elastic range. Beam sections are also sufficiently slender to consider shear forces negligible, thus enabling the use of two-dimensional Euler-Bernoulli plane frame elements [183]. Impacts are recognised as being of low enough velocity to consider plastic deformation energy losses as negligible in comparison with the magnitudes of kinetic energy being transferred between the bodies [184]. Impacts are therefore approximated as elastic interactions between single finite element nodes.

A schematic of the model structure is shown in Figure 4.3. It was developed using the Python programming language with associated libraries. It comprises a two-dimensional geometry employing Euler-Bernoulli plane frame elements with lumped masses and rotational inertias added to relevant degrees of freedom for the fixed masses in the structure (described in section 4.2.2). The free-magnet resonators are modelled separately as rigid bodies (i.e., vibrations internal to the resonators are ignored (see section 4.2.3)), and contact and magnetic interaction forces between the resonators and structure are calculated at each time step (discussed in section 4.2.5). Transient motion is calculated using a central difference time-stepping scheme (described in section 4.2.6).

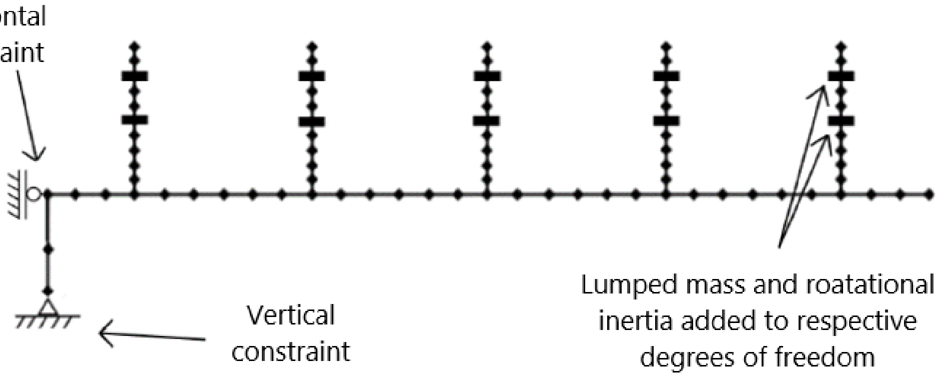

Figure 4.3 Schematic for five-strut metabeam elastic structure developed in Python using Euler-Bernoulli plane frame elements. Magnetic resonators, which are separately modelled as rigid bodies and interacting with the structure via Hertzian contact mechanics, are not shown.

4.2.2 Modelling the continuous structure

The metabeam structure considered in this study can be modelled as a long slender cantilever with a series of smaller cantilevers orthogonally attached along its length. To model this structure, two-dimensional Euler-Bernoulli frame elements are used. Each element comprises two nodes, the positions of which are specified by cartesian coordinates with respect to a set of global coordinate axes. Each node has three degrees of freedom – two translation and one rotation. Derivation of the Euler-Bernoulli frame element relies on the assumption that shear deformation can be ignored (i.e., cross-sectional plane sections perpendicular to the beam axis remain perpendicular and plane in the deformed state). The slenderness ratio of beam sections in the present model is easily sufficient for this to be considered a good approximation [183].

The Euler-Bernoulli beam element derivation also neglects the effects of rotational inertia. This can become an issue for high-frequency vibrations for which the flexural wavelength (λ) approaches approximately six times the cross-sectional depth [185]. Flexural wavelength (λ) in an Euler-Bernoulli beam can be calculated according to the following equation [186]:

$$\lambda = 2\pi\left(\frac{EI}{\rho \mathrm{A}\omega^2}\right)^{\frac{1}{4}} \tag{4.1}$$

where E is Young's modulus, I is the second moment of area, ρ is the mass density, A is the cross-section area, and ω is the angular frequency. In the present model, the wavelength approaches this threshold in the host-beam and individual struts for frequencies of 60 MHz and 1 MHz, respectively. It is therefore considered reasonable to neglect rotational inertia effects.

According to the Euler-Bernoulli beam theory, the potential energy (U) and kinetic energy (T) can be derived as follows:

$$U = \frac{1}{2}\int_0^L EA(x)[u'(x,t)]^2 dx + \frac{1}{2}\int_0^L EI(x)[v''(x,t)]^2 dx \tag{4.2}$$

$$T = \frac{1}{2}\int_0^L m(x)\{[u'(x,t)]^2 + [v'(x,t)]^2\} dx \tag{4.3}$$

where A is the cross-section area, I is the moment inertia and L is the length of the beam element.

The stiffness matrix and mass matrix can be derived from the Hermite cubic shape function as follows:

$$\boldsymbol{k}_e = \begin{bmatrix} \frac{EA}{L} & 0 & 0 & -\frac{EA}{L} & 0 & 0 \\ 0 & \frac{12EI}{L^3} & \frac{6EI}{L^2} & 0 & -\frac{12EI}{L^3} & \frac{6EI}{L^2} \\ 0 & \frac{6EI}{L^2} & \frac{4EI}{L} & 0 & -\frac{6EI}{L^2} & \frac{2EI}{L} \\ -\frac{EA}{L} & 0 & 0 & \frac{EI}{L} & 0 & 0 \\ 0 & -\frac{12EI}{L^3} & -\frac{6EI}{L^2} & 0 & \frac{12EI}{L^3} & -\frac{6EI}{L^2} \\ 0 & \frac{6EI}{L^2} & \frac{2EI}{L} & 0 & -\frac{6EI}{L^2} & \frac{4EI}{L} \end{bmatrix} \tag{4.4}$$

$$\boldsymbol{m}_e = \frac{m}{420} \begin{bmatrix} 140 & 0 & 0 & 70 & 0 & 0 \\ 0 & 156 & 22L & 0 & 54 & -13L \\ 0 & 22L & 4L^2 & 0 & 13L & -3L^2 \\ 70 & 0 & 0 & 140 & 0 & 0 \\ 0 & 54 & 13L & 0 & 156 & -22L \\ 0 & -13L & -3L^2 & 0 & -22L & 4L^2 \end{bmatrix} \tag{4.5}$$

The global stiffness ($\boldsymbol{K}$) and mass ($\boldsymbol{M}$) matrices are assembled by first multiplying rotated element matrices by a derived rotation matrix and then assembling them such that shared dofs are superposed. In the present model, rotated elements are orthogonal to unrotated elements, leading to a simple swapping between x and y translation dofs for rotated elements. Fixed masses are added into the structure explicitly by specifying the location of a node for each mass at the location of its centre of gravity and adding its inertial properties to the respective dofs.

For structural vibrations, a proportional (Rayleigh) damping scheme is employed. This involves the calculation of a damping matrix, $\boldsymbol{C}$, which is proportional to the mass and stiffness matrices, $\boldsymbol{M}$ and $\boldsymbol{K}$, according to the following relation:

$$\boldsymbol{C} = \eta \boldsymbol{M} + \delta \boldsymbol{K} \tag{4.6}$$

where η and δ are scalar constants of proportionality. These constants are derived to enable the damping matrix to be of a form that uncouples the modal equations [187]. This requires the damping matrix to have the following properties:

$$2\omega_n \zeta_n = \phi_n^T \boldsymbol{C} \phi_n = \eta \phi_n^T \boldsymbol{M} \phi_n + \delta \phi_n^T \boldsymbol{K} \phi_n \tag{4.7}$$

$$\text{and } \phi_n^T \boldsymbol{C} \phi_m = 0 \quad n \neq m \tag{4.8}$$

using the orthogonality properties of the mass as stiffness matrices, this leads to:

$$\zeta_n = \frac{1}{2\omega_n}\eta + \frac{\omega_n}{2}\delta \tag{4.9}$$

which can be solved for two natural frequencies ω_1 and ω_2 to obtain η and δ. The frequencies, ω_1 and ω_2, are identified at the beginning of the simulation via an eigenvalue analysis, as those closest to the upper and lower limits of the frequency range of interest (20 – 120 Hz). The respective damping ratios, ζ_1 and ζ_2, are set equal to each other, and a damping ratio of 0.04 is selected as an approximation for an aluminium and steel structure with threaded connections, in line with experimental data presented in [188].

A central difference scheme, which is detailed in section 4.2.6, is then employed to solve the following equation of motion for the structure:

$$\boldsymbol{M}\ddot{\boldsymbol{u}} + \boldsymbol{C}\dot{\boldsymbol{u}} + \boldsymbol{K}\boldsymbol{u} = \boldsymbol{F} \tag{4.10}$$

The force vector ($\boldsymbol{F}$) is generated for each time step. It contains the input force applied to the vertical dof of the base node of the host beam, the contact forces applied at the horizontal dofs of each impact node on the struts, and the magnetic reaction forces applied at the fixed magnet nodes. Magnetic reaction forces include both vertical repulsive forces and horizontal reaction forces that balance the torque applied to the resonator.

4.2.3 Modelling vibration-dominated impacts

Characteristics of transverse impacts between compact bodies and long slender bodies differ significantly from those involving compact bodies only, largely because the slender body's response includes some degree of internal vibration, whereas that of a compact body approximates a simple rigid body translation and rotation [189]. This leads to a decrease in the magnitude of peak forces and a transmission of some part of the pre-impact kinetic energy into the vibration of the slender body [184]. It also leads to an increase in the complexity of contact interactions, opening up the possibility of repeated sub-impacts prior to the net separation of the bodies [190, 191]. An important consideration for modelling such impacts is the relative velocity of the impacting bodies. For velocities smaller than the lowest wave speed in the impacting bodies, the impact can be treated as quasi-static, wherein equilibrium conditions are fulfilled at each moment in time [192]. The impacts occurring in the system under consideration can be considered to be of low-velocity in this respect.

Two broad categories of impact simulation exist for low-velocity impacts. One involves the integration of the forces acting between impacting bodies over the duration of contact. The other pre-supposes an instantaneous impact duration and calculates post-impact velocities from pre-impact velocities by applying a coefficient of restitution. While the instantaneous impact assumption and coefficient of restitution can be used to generate predictions of high accuracy with relatively low computational overhead, they rely on the supposition that the duration of individual impacts is small, relative to the time between impacts [193]. Preliminary high-resolution modelling of the system under consideration suggests that, in some instances, impact duration is likely to be of a similar order to that of the time between impacts. For the system under consideration, an important implication of this is that the resonator is expected to rotate somewhat during each impact. It would therefore be necessary to calculate a post-impact rotation state for the resonators based on the period of each impact. Preliminary calculations for this were performed but ultimately abandoned in favour of the alternative described below. These calculations are shown in Appendix 2.

A second complicating factor for the potential use of a coefficient of restitution-based model is in the vibratory response of the cantilever. As has already been discussed, transverse bending of the cantilever means that a simple momentum balance does not hold. Instead, a portion of the momentum goes into the vibratory motion. Some previous work has focused on the development of methods employing modal decomposition to enable the use of restitution-based modelling for vibration-dominated impacts [194-196]. These approaches offer effective reductions in computational overhead, but for the system under consideration, they would necessitate the development of a method for accounting for a non-zero impact duration. The method chosen for this model, therefore, integrates the impact forces over the duration of contact using an Euler-Bernoulli finite element-based approach.

A detailed schematic of the free-magnet resonator in contact with the strut is shown in Figure 4.4. In the two-dimensional model, the positions of the four points on the inner surface of the resonator that can make contact with the strut are derived from the horizontal position of the resonator's CG and the angle of its rotation. For the purpose of impact simulation, the vertical motion of the resonator with respect to the strut is ignored. Impact points on the surface of the strut can therefore be derived from the horizontal displacement of two strut impact nodes alone, which are positioned at the height of the contact points when the resonator is at rest. This is considered a reasonable approximation as the amplitude of vertical motion of the resonator is on the order of less than one millimetre.

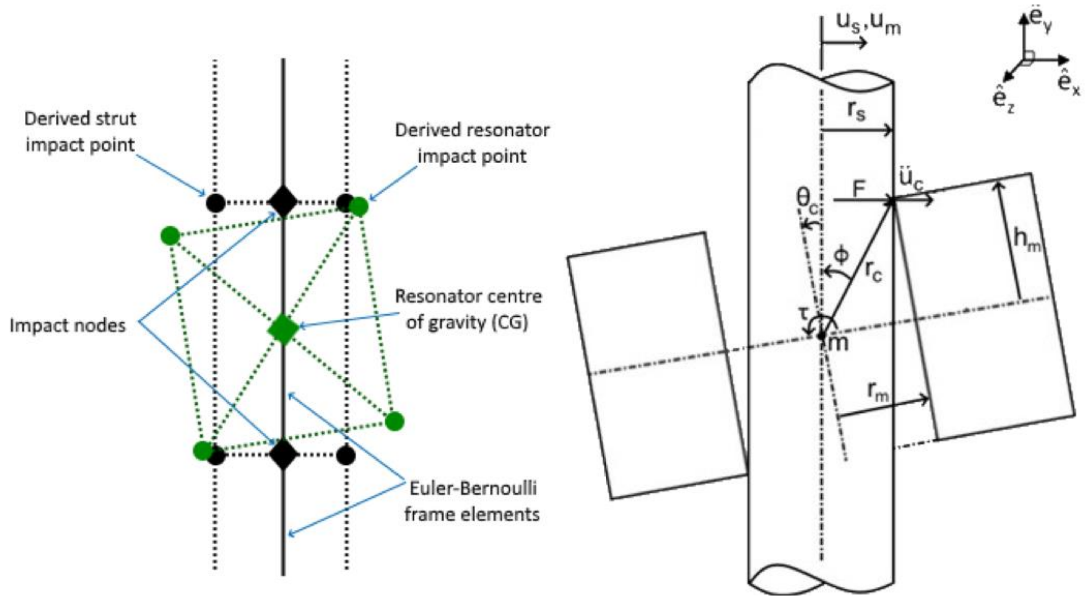

Figure 4.4 Interaction between strut and magnetic resonator prior to separation. u_s *and* u_m *are the displacements of the strut and resonator centre of gravity (CG) respectively (these are identical prior to separation).* r_s *and* r_m *are the radii of the strut and resonator respectively,* r_c *is the distance of the contact point from the resonator CG,* h_m *is half the thickness of the resonator,* ϕ *is the angle of* $\mathbf{r}_c$ *from vertical,* θ_c *is the angle of rotation of the resonator from vertical when at rest, F is the magnitude of the force applied to the resonator by the strut,* $\ddot{u}_c$ *the lateral acceleration of the resonator contact point,* τ *is the magnetic torque applied about the resonator CG. and m is the mass of the resonator which is represented in the equations of motion as a lumped mass located at the resonator CG*

At each time step, the horizontal positions of all eight contact points are calculated (see Appendix 1, section A 1.1). Any time a node pair is found to have overlapped (indicating that the bodies have interpenetrated), a contact force, which varies with the size of that overlap, is applied to both nodes. The magnitude of the force is derived using Hertzian contact theory for contact between two bodies with curved surfaces according to the following relation:

$$F = \frac{4}{3}E^{*}R^{1/2}d^{3/2} \tag{4.11}$$

where F is the contact force in newtons, E^{*} is the effective elastic modulus of the combined interacting materials, derived from their respective individual moduli, E_1 and E_2, and Poisson's ratios, υ_1 and υ_2, according to the relation:

$$\frac{1}{E^{*}} = \frac{1-\upsilon_1^2}{E_1} + \frac{1-\upsilon_2^2}{E_2} \tag{4.12}$$

R is the equivalent radius of the interacting geometries calculated from the inner radius of the resonator, R_1, and the radius of the strut, R_2, according to the relation:

$$\frac{1}{R} = \frac{1}{R_1} + \frac{1}{-R_2} \tag{4.13}$$

and d is the magnitude of the overlap between the node pair [197] (Appendix 1, section A 1.5). The program then independently calculates the acceleration response in the two bodies by applying the contact force to both and using a central difference time-stepping scheme described in section 4.2.6.

4.2.4 Initial conditions for pre-stressed regions

The system is initially at rest with velocities and accelerations set to zero. In this state, the resonator magnet is suspended by magnetic forces such that it is rotated about its z-axis to be in contact with the strut at two points (see Figure 4.4). It is therefore being acted on by a combination of a magnetically induced torque and reaction forces from the strut at the contact points. For the reaction forces to balance the magnetic torque, the bodies must overlap at each contact point by an amount that produces the correct Hertzian contact force. In the model, this is achieved by running the simulation in the absence of an externally applied input force, with a ramping function applied to increase the internal magnetic forces over time. Force ramping minimises residual vibrations, which would otherwise result from applying the full magnitude of the internal forces instantaneously.

In a similar vein, the magnetic forces acting on the two fixed magnets of each strut produce an initial longitudinal strain in the section of strut between the magnets due to magnetic repulsion and a transverse bending due to the reaction forces that balance the torque applied to the resonator magnet (see Figure 4.5).

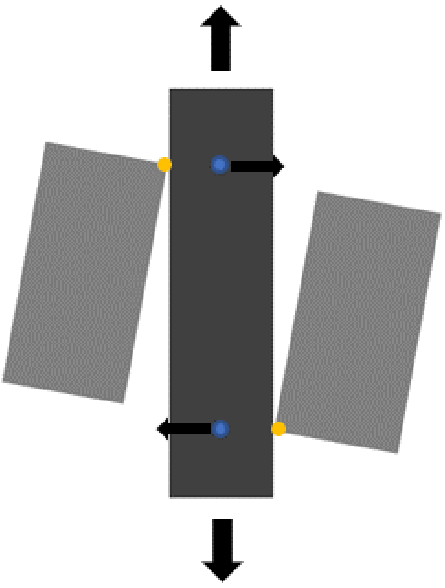

Figure 4.5 Schematic showing structural deformation caused by prestressing due to internal magnetic forces. Vertical arrows indicate elongation of the strut due to magnetic repulsion, and the horizontal arrows indicate transverse bending due to contact forces.

The structural deformation state is therefore also saved at the end of force ramping simulations for use as an initial condition. Force ramping is achieved by multiplying the internal magnetic forces by a time-varying sigmoid function:

$$S(t) = \frac{1}{1 + e^{-t}} \tag{4.14}$$

The shape of the sigmoid function, shown in Figure 4.6, eliminates sudden changes in acceleration, which can result in residual vibrations, allowing the force to be increased more quickly.

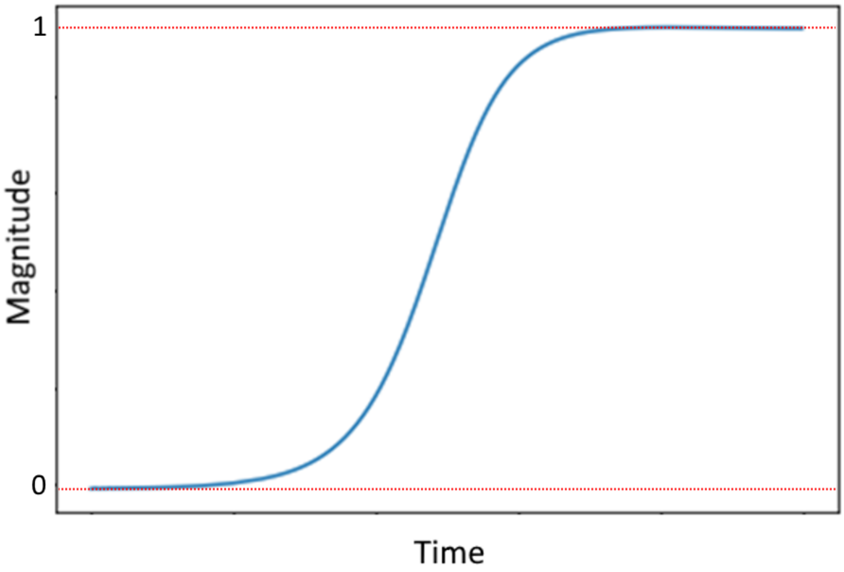

Figure 4.6 Sigmoid function used as a multiplier for internal magnetic forces during the force ramping process.

4.2.5 Resonator dynamics

Each resonator magnet is modelled as a rigid body using a single node with three dofs – two translation and one rotation. Both spring forces and contact forces are pre-calculated for each time step and applied as external input forces to each body. The vertical spring forces ($\boldsymbol{F_s}$) are calculated from the following experimentally derived force-displacement curve:

$$\boldsymbol{F_s} = -0.148 + 94.5/(1 + (u/2.02e8)\text{^}0.552)\text{^}3.65e4 \qquad (4.15)$$

where u is the distance between the surfaces of repelling magnets (see Section 4.2.7 for experimental measurement procedure). Two vertical magnetic force pairs are therefore present in each assembly at any one time – that between the upper surface of the resonator and the upper fixed magnet and that between the lower surface of the resonator and the lower fixed magnet. The net force on the resonator is therefore equal to the instantaneous difference between the two forces. These forces are applied to the vertical degrees of freedom at each respective node.

Contact forces ($\boldsymbol{F_c}$) are calculated according to equation (4.11) and applied to the horizontal dof of each resonator and strut contact point. Being applied at a distance from the resonator's centre of gravity, both contact and magnetic forces also induce a torque ($\boldsymbol{T}_c$) which is added to the rotational dof. Damping for the motion of the oscillating resonator magnet is likely affected by air resistance and a phenomenon known as eddy current damping. This is a form of energy dissipation that occurs due to the excitation of electrons in current-carrying materials in the presence of a changing magnetic field. Direct calculation of both of these effects is highly complex and beyond the scope of this study. As a practical alternative, a damping factor (c) for the vertical motion of the resonator magnet was estimated using experimental observation.

To model the motion of each resonator under the influence of the magnetically induced torque and contact and damping forces, the following equation of motion is solved using a central difference time-stepping scheme:

$$\boldsymbol{M\ddot{u}} + \boldsymbol{C\dot{u}} = \boldsymbol{F} \tag{4.16}$$

where:

$$\boldsymbol{M} = \begin{bmatrix} m_r & 0 & 0 \\ 0 & m_r & 0 \\ 0 & 0 & I \end{bmatrix}, \boldsymbol{C} = \begin{bmatrix} c & 0 & 0 \\ 0 & c & 0 \\ 0 & 0 & 0 \end{bmatrix}, \ \boldsymbol{u} = \begin{bmatrix} u_x \\ u_y \\ \theta \end{bmatrix}, \text{and } \boldsymbol{F} = \begin{bmatrix} F_c \\ F_r \\ T + \tau \end{bmatrix}$$

4.2.6 Transient solution scheme

A central difference time-stepping scheme is employed to solve the transient equations of motion for both structure and resonators. At each time step, structure and resonator equations are solved independently. Then contact forces are calculated, based on the interpenetration of the bodies, and applied at the next step.

For the structure, the equation of motion (4.10) can be rewritten as:

$$\boldsymbol{M}\frac{\boldsymbol{u}^{n+1} - 2\boldsymbol{u}^{n} + \boldsymbol{u}^{n-1}}{\Delta t^2} + \boldsymbol{B}\frac{\boldsymbol{u}^{n+1} - \boldsymbol{u}^{n-1}}{2\Delta t} + \boldsymbol{K}\boldsymbol{u}^{n} = \boldsymbol{F}^{n} \tag{4.17}$$

which leads to the following equations for the value of $\boldsymbol{u}$, $\dot{\boldsymbol{u}}$ and $\ddot{\boldsymbol{u}}$ at each new time step:

$$\boldsymbol{u}^{n+1} = (\boldsymbol{M} + \frac{\boldsymbol{B}}{2}\Delta t)^{-\mathbf{1}}(2\boldsymbol{M}\boldsymbol{u}^{n} + \left(\frac{\boldsymbol{B}}{2}\Delta t - \boldsymbol{M}\right)\boldsymbol{u}^{n-1} + \Delta t^2(\boldsymbol{F}^{n} - \boldsymbol{K}\boldsymbol{u}^{n})) \tag{4.18}$$

$$\dot{\boldsymbol{u}}^{n} = \frac{\boldsymbol{u}^{n+1} - \boldsymbol{u}^{n-1}}{2\Delta t} \tag{4.19}$$

$$\ddot{\boldsymbol{u}}^{n} = \boldsymbol{F}^{n} - \boldsymbol{B}\dot{\boldsymbol{u}}^{n} - \boldsymbol{K}\boldsymbol{u}^{n} \tag{4.20}$$

The same procedure is used to solve the transient equation of motion for the resonators, and the code implementation of these is shown in Appendix 1, sections A 1.9 and A 1.10.

4.2.7 Derivation of the magnetic force-displacement curve

As has already been mentioned, the forces applied to the resonators and fixed magnets in the model are derived from a force-displacement curve based on experimental measurements. To generate this curve, an experimental apparatus was assembled to measure the force between a resonator/fixed magnet pair for a range of different separation distances. In the setup used to do this (shown in Figure 4.7), a digital calliper was rigidly fixed to a telescopic steel pole which was, itself, connected to the ground reference frame via a tripod structure. The body of the calliper was fixed to the stationary part of the telescopic pole and its depth probe to the pole's extension arm so that the arm's extension is measured. On the end of the pole, a plastic fixture serves to press downwards on the resonator magnet, which is axially aligned with the strut and the fixed magnet beneath it. The plastic fixture maintains a separation between the magnets and the steel pole to avoid interference of the magnetic fields from the steel. Similarly, the magnet/strut assembly is supported on a glass stand to maintain a distance between the magnets and

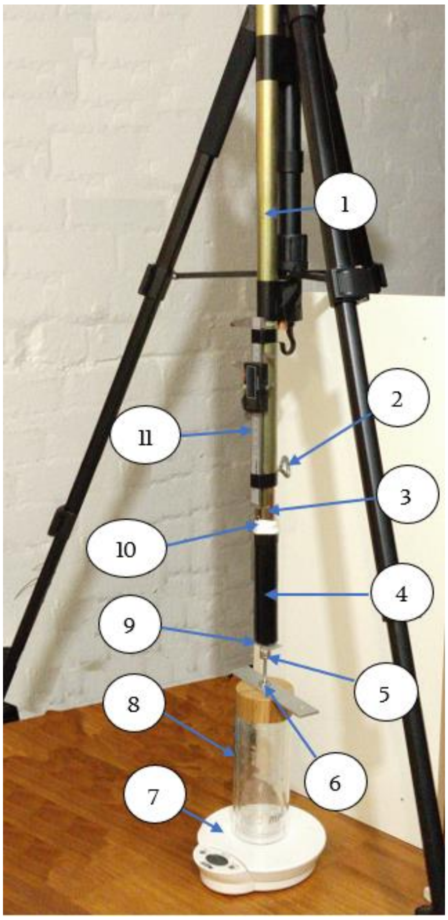

1. Telescopic pole connected to reference frame (rigidly fixed to ground)
2. Telescopic pole extension release
3. Telescopic pole extension (for setting the height of the resonator magnet
4. Plastic fixture at end of height extension pole to avoid magnetic interference from steel pole
5. Resonator magnet
6. Fixed magnet
7. Digital scale
8. Glass support stand for magnet spring assembly (to avoid magnetic interference with/from scale)
9. Aluminium components for even force distribution
10. Caliper depth probe (fixed to height extension)
11. Digital caliper (fixed to reference frame)

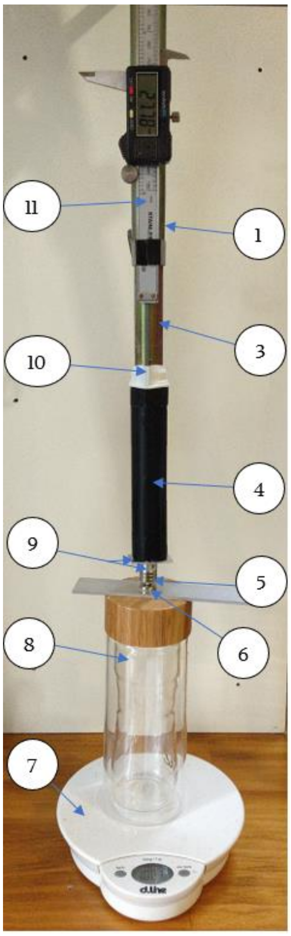

Figure 4.7 Experimental setup for measuring the force-displacement curve for the force between a fixed magnet and the resonator magnet.

the digital scale beneath.

Measurements were made with the resonator/magnet pair separation ranging between approximately 5 and 32 mm. A curve-fitting algorithm was then used to fit a curve to the data. The equation for the fitted curve is shown in Equation (4.15), and the measurement results with the fitted curve are shown in Figure 4.8. Raw measurement data is shown in Appendix 3.

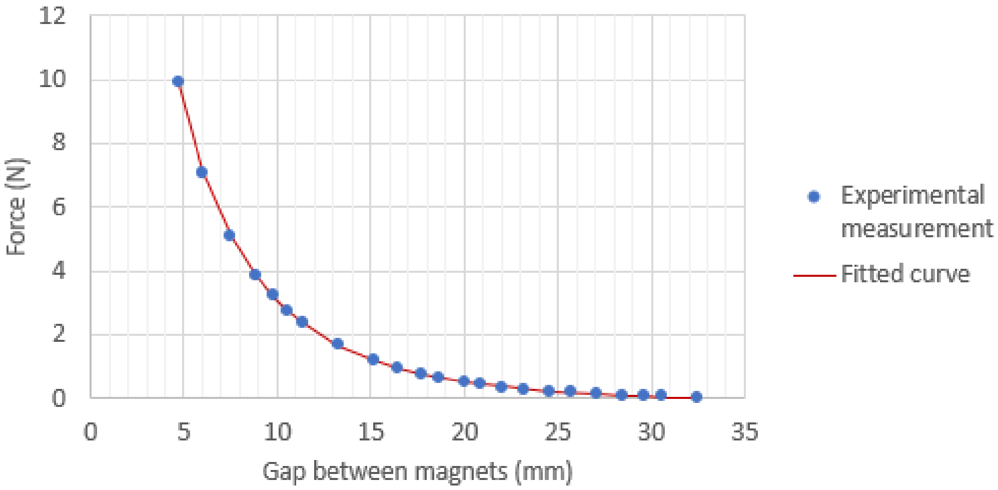

Figure 4.8 Measurement results and fitted curve for the repulsive magnetic force between a resonator and fixed magnet.

4.3 Model validation

The model validation process that was undertaken was born of a need to ensure the accuracy of the developed numerical model without ongoing access to an experimental laboratory (due to movement restrictions imposed during the Covid-19 pandemic). An approach was therefore developed which employed both previously published experimental data and a high-resolution three-dimensional model developed in COMSOL.

The model developed in COMSOL is a 3-D geometry comprising 57000 degrees of freedom per unit cell and employs quadratic serendipity shape functions. The maximum element size in contact regions is 50 µm. Contact is modelled using the penalty method with a penalty factor of 1.5×10^{17}N/m^3. Contact response was benchmarked against previously published data presented in [198]. Mesh convergence studies were run using eigenfrequency and frequency-based analyses for the bare beam, bare strut, beam with strut attached and beam with strut, retainer and fixed magnets attached. Studies were undertaken to determine mesh size requirements for different input frequencies, effects of shape function order, element type and local mesh density for contact regions.

Transient analyses were solved using the generalised alpha time-stepping method with a global tolerance factor of 1×10^{-4}. A maximum time step of 1 μs and a 0.75 amplification factor for high frequencies.

The experimental data used for benchmarking was presented in [198]. The data was for the dynamic response of a slender Aluminium cantilever to an impact from a steel ball – a setup with close similarities to the system under investigation (see section 4.3.1). By first validating both models against the experimental data, confirmation was attained of the validity of methods and parameters used to model individual impacts and the transient structural response of an Aluminium cantilever.

The COMSOL model was then used as a benchmark for future changes. In practice, this involved making a single change in both models (for example, changing the cross-section of the cantilever to match that of the cantilever attachments in this study) and validating the simplified model against results from the high-resolution model. This process was repeated until the full unit cell structure had been modelled and validated against the high-resolution COMSOL model. At each step, the transient structural response to a single impact was validated as well as the structure's modal properties. The validation sequence is shown graphically in Figure 4.9. Validation results for key steps in this process will be described in the following sections.

Finally, the unit cell was incorporated into a five-unit cell model and validated against experimental results that were presented in Chapter 3 of this thesis. Analysis of results from this model is presented at the end of this chapter.

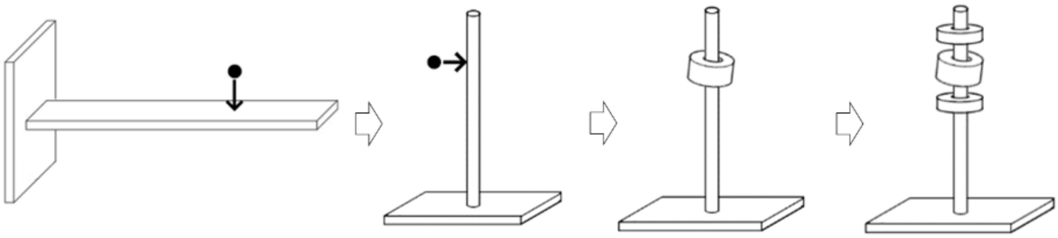

Figure 4.9 The sequence of steps used for preliminary validation of the developed model. First both models were validated against experimental data for the setup on the left, then the model geometry was progressively updated and compared with high-resolution model at each step.

4.3.1 Single impact experimental benchmark

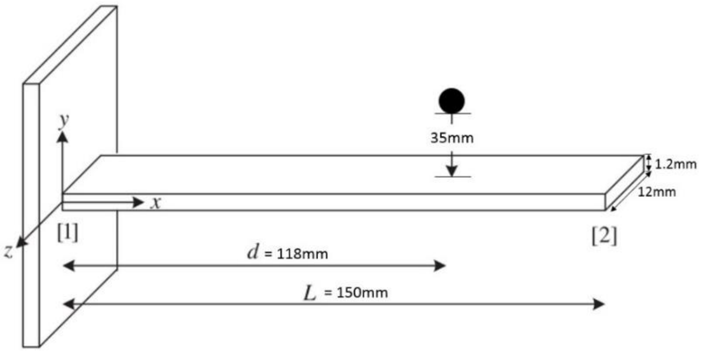

Figure 4.10 Experimental setup used to produce the data (previously published) that was used to validate the transient cantilever impact responses in base models [198].

The experimental setup used to generate the data used for benchmarking was presented in [198] and is shown in Figure 4.10. In the experiment, a 3.17 mm diameter steel ball is freely dropped onto the top surface of a 1050 Aluminium, 150 x 12 x 1.22 mm cantilever beam, from a height of 35 mm at a point 118 mm from the fixed end. The ball drop was triggered by an electromagnet, and displacement measurements were made using an optic fibre sensor with a resolution of 0.25nm and an upper-frequency limit of 500 kHz. In the models, gravity is ignored, and the initial velocity of the steel ball is calculated based on the initial experimental drop height. Simulation time history results for beam impact point displacement for both Python and COMSOL models are compared with the experimental data in Figure 4.11, showing a high level of agreement.

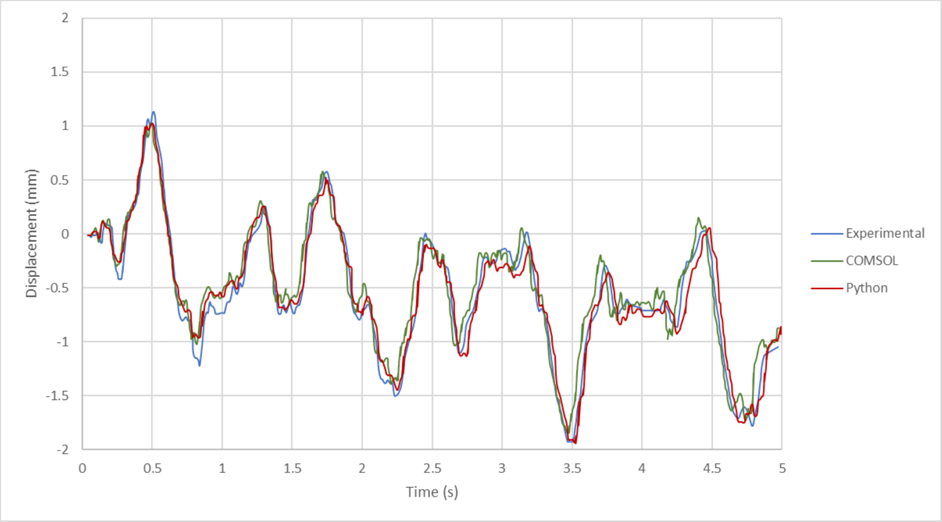

Figure 4.11 Comparison between experimental data obtained from [198] and present results for transient vertical displacement response to single impact from steel ball of a 150 x 12 x 1.22 mm cantilever, at a point 20 mm from the fixed end

Table 4.1 Eigenvalue comparison for the first ten modes of the experimental structure used as the basis for the experiments that produced data for benchmarking obtained from [198].

Mode number	Experimental eigenvalues (Hz)	Theoretical eigenvalues (Hz)	Model eigenvalues (Hz)	% Error (with respect to theory)
1	44	44.292	44.297	0.010
2	277	277.596	277.606	0.004
3	778	777.354	777.306	-0.006
4	1521	1523.198	1523.209	0.001
5	2516	2517.915	2517.974	0.002
6	3769	3761.523	3761.418	-0.003
7	5253	5253.370	5253.551	0.003
8	7008	6994.406	6994.374	0.000
9	8999	8984.195	8983.885	-0.003
10	11240	11221.985	11222.087	0.001

The eigenvalue response for the Python model was also compared with experimental data reported in [198] and theoretical predictions for an Euler-Bernoulli beam.[7] The comparisons (displayed in Table 4.1) show a strong correspondence between model results and both experimental data and theoretical predictions.

4.3.2 Single impact between resonator and strut

To assess the impact response for the resonator and structure, time histories for the contact points on the resonator and structure after a single impact are shown in Figure 4.12 (a). In that test, an initial velocity (V_0) of 0.83 m/s is applied, and the impact occurs in the first 50 μs. The results show that the resonator makes contact with the cantilever more than once before the two finally separate. It is evident that a small variation between the post-impact velocities for the first sub-impact can lead to a significantly larger variation in subsequent impacts. This is due to the fact that, by delaying the second impact by only a small margin, a large difference in the phase of the oscillating cantilever can accompany the second sub-impact. This can lead to a larger post-impact velocity variation than would be expected for an impact with a stationary structure. It is expected that, while this may affect individual impact outcomes, it should not create a mean bias over a large number of impacts.

To assess the post-impact rotation inertial response of the resonator, Figure 4.12 (b) shows results for a comparison of models in which resonator rotation was allowed magnetic torque was excluded. The post-impact velocities of both points on the resonator are almost identical for both models indicating that the inertial response of the simplified model is closely matching that of the high-resolution model.

---

[7] The nth natural frequency (ω_n) for a cantilever beam can be solved as $\omega_n = \left[(2n-1)\frac{\pi}{2}\right]^2 \sqrt{\frac{EI}{\rho A L^4}}$ [186]

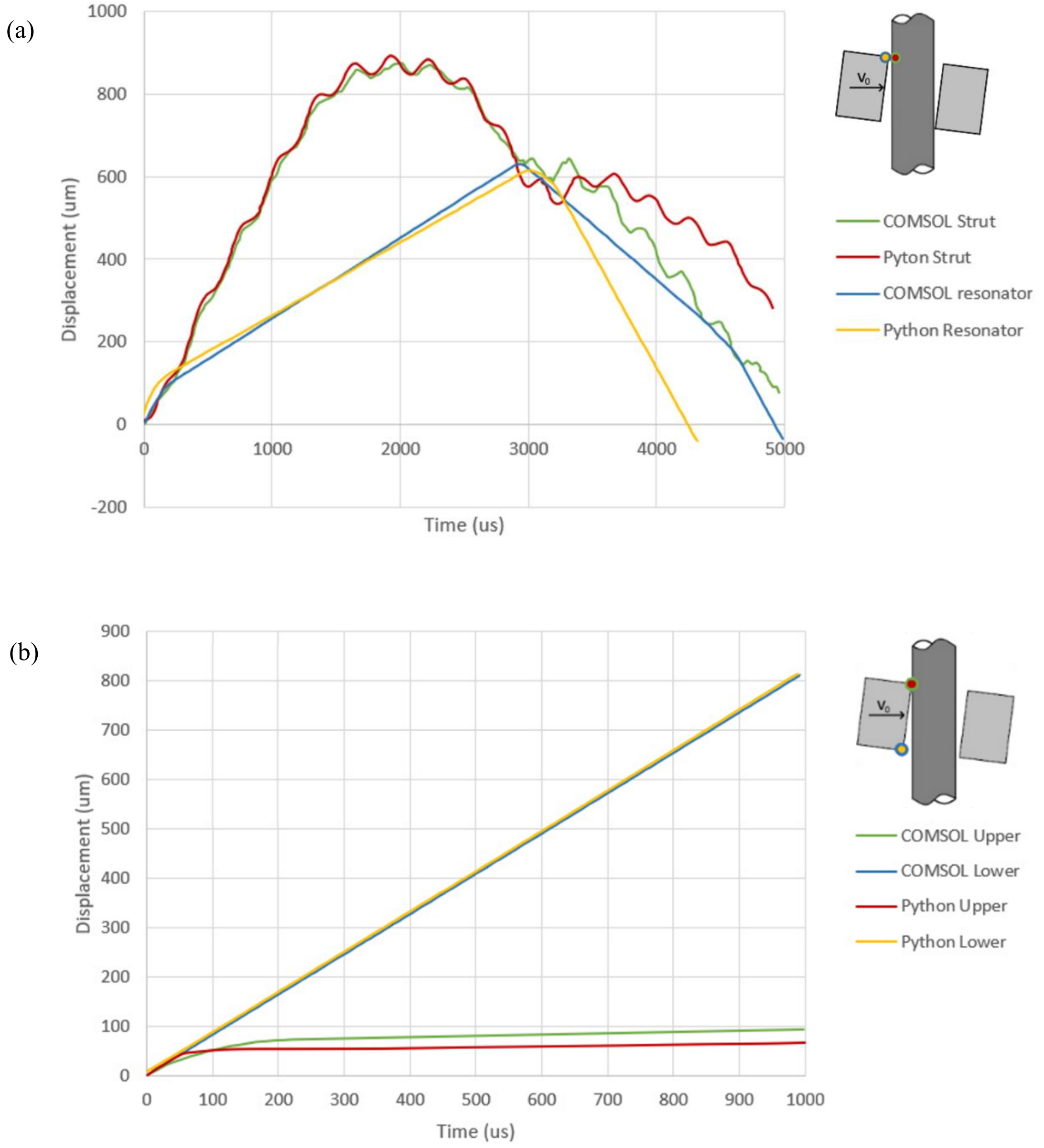

Figure 4.12 Transient displacement of contact points for resonator and structure after a single impact. The structure was initially at rest, and the resonator had initial velocity, $V_0 = 0.83$ m/s. In (a), displacements at the point of contact on both strut and resonator are compared over the course of 0.05 s. In (b), the rotation response of the resonator is assessed by tracking two points on the resonator over the course of 0.01 s the resonator was given an initial velocity (V_0) of 0.83 m/s and the impact occurs in the first 50 µs

4.3.3 Full system validation

To assess the modal response of the full elastic structure, eigenvalues were calculated for both models and compared for each stage of the validation. Figure 4.13 compares eigenvalue results for the full five-unit cell elastic structure with fixed magnet masses attached. The results show a close correspondence between the simplified Python model and the high-resolution COMSOL model.

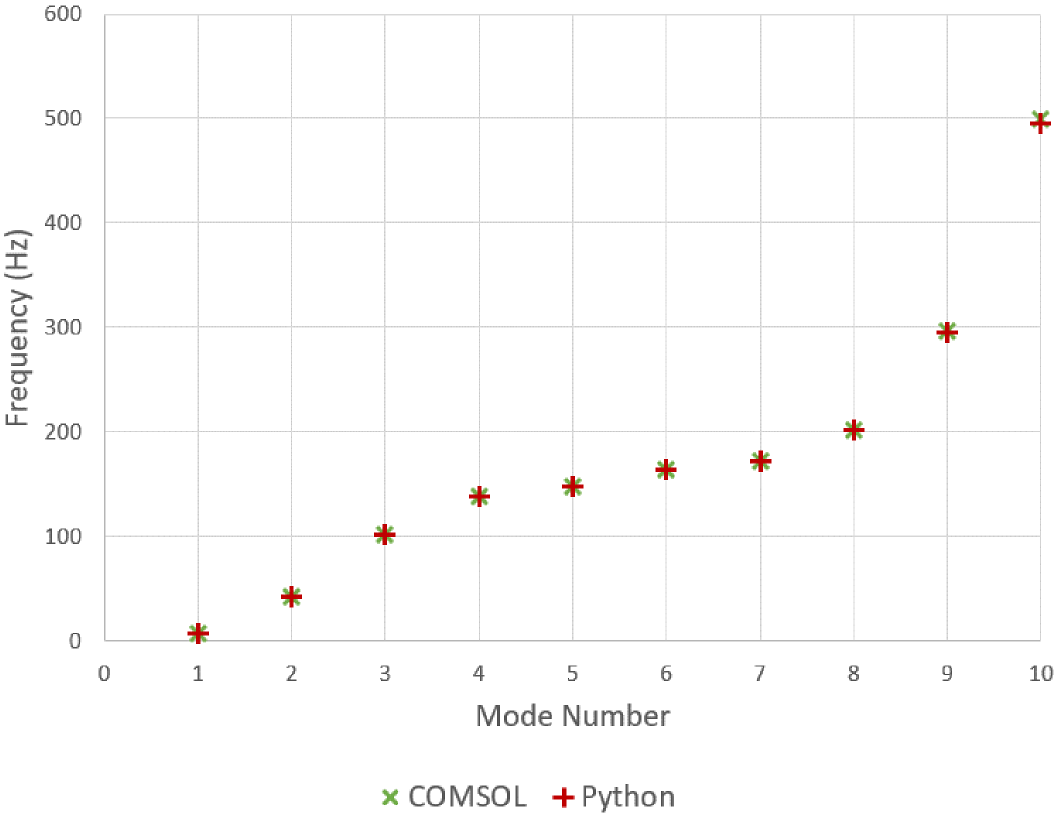

Figure 4.13 Eigenvalue analysis for the full, five-strut elastic structure with fixed magnet masses comparing results from the high-resolution COMSOL model, the simplified Python model.

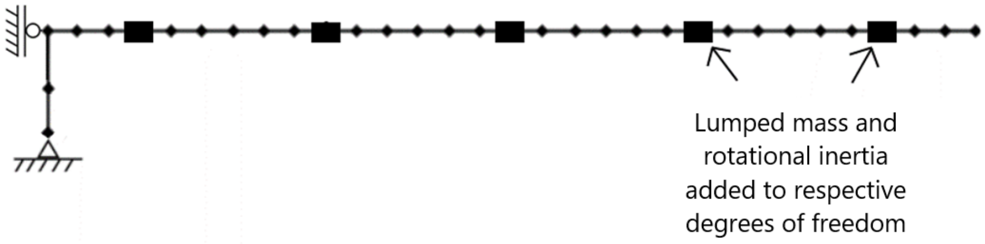

Figure 4.14 Reference beam configuration: identical to the metabeam except that the resonator assemblies are replaced by equivalent lumped masses. In the experiment, the mass was fixed such that its bottom surface rested on the host beam. In the model, the mass and rotational inertia are added to the node at the junction between the strut and the host beam. Rotational inertia is calculated with respect to the centre of the bottom surface of the experimental mass.

The experimental data used to validate the full five-resonator metabeam model was presented in Chapter 3. In that study, vertical vibration displacements at the input and output ends of a series of reference and prototype metabeams were measured. Reference beams were identical to prototype beams except for their having the resonator assemblies replaced by equivalent lumped masses located at the base of each strut (see Figure 4.14).

4.3.3.1 Input conditions

In the experimental setup, the electrodynamic shaker was adapted from a sub-woofer speaker. The shaker was driven by an amplified, frequency limited (10 – 200 Hz) pink noise waveform; however, the vibration response at the input end of all beams tested showed a distinct resonance peak in the frequency range around 50 Hz. The independence of the frequency of this peak on the mass of the beam suggests that it is due to a non-flat frequency response from the shaker itself. This might be explained by a reduced cavity volume of the speaker box caused by the presence of masses added to limit vibration transfer from the shaker to the measuring laser via the floor.

To reproduce the experimental input signal in the model, the waveform recorded at the input end of the experimental reference beam for each input level was employed. Figure 4.15 compares frequency spectra produced by the model with experimental spectra recorded at the input end of the reference beam for two input levels. The close correspondence shows that this excitation approach accurately reproduces the experimental input frequency conditions. This approach is therefore used for subsequent simulations.

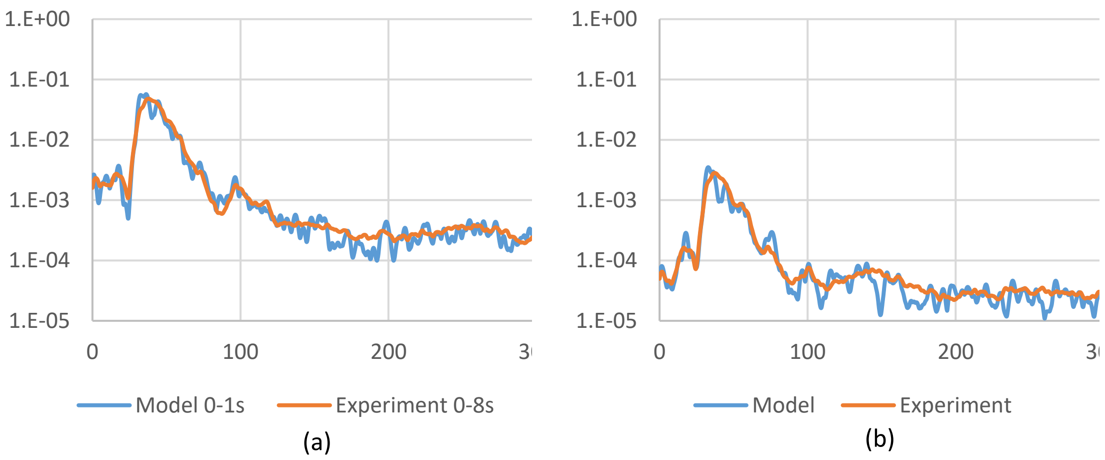

(a) (b)

Figure 4.15 Comparison of model and experimental frequency spectra for the vibration response recorded at the input end of the reference beam for (a) the highest input level (670 N RMS) and (b) the lowest input level (37 N RMS).

A schematic of the beam boundary condition configuration used in the model is shown in Figure 4.16. Preliminary measurements showed the shaker mount tended to exhibit a small amount of lateral motion in the direction of the beam axis (on the order of 50 μm for the highest input level). It is expected that this is due to a small amount of compliance in the armature support. To approximate this in the model, the base of the beam is attached to a short, three-node Euler-Bernoulli beam section which is pinned at its base (constrained for translation but free to rotate). The node at the junction between this support and the base of the beam is free to rotate as well as translate vertically

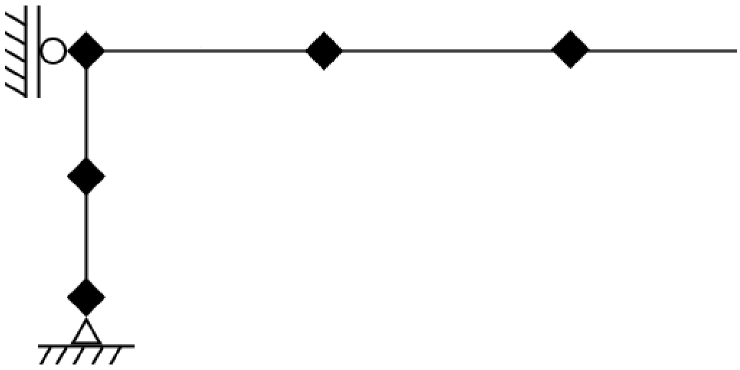

Figure 4.16 Input boundary condition configuration showing the grounded vertical spring support connected to the input end of the main beam (showing only the first three beam nodes). The vertical input force was applied at the junction node between the beam and spring support. The spring support is pinned at the base and the junction node is constrained horizontally only.

(i.e., horizontal translation is constrained). This beam section thus acts as an elastic support which also allows a small degree of rotation at the base of the beam. The effective axial and bending stiffnesses of the elastic support were estimated by measuring the displacement of the beam attachment point on top of the shaker armature in response to static forces applied in each direction.

To validate this setup, reference beam model results were compared against experimental results for the mean (RMS) displacement amplitude and the shape of the frequency response measured at the output end of the beam. Figure 4.17 shows model and experimental mean (RMS) amplitude response at the output end of a reference beam and shows good correlation. This also enabled the identification of the input force levels required to produce the same mean (RMS) vibration amplitudes at the input end of the reference beam in the model as in the experimental setup. The input force levels (RMS) used for simulations in this chapter were therefore 37, 124, 222, 386, and 670 N which corresponded to 0.009, 0.031, 0.055, 0.096, and 0.167 mm mean (RMS) amplitude response at the output end of the experimental reference beam respectively.

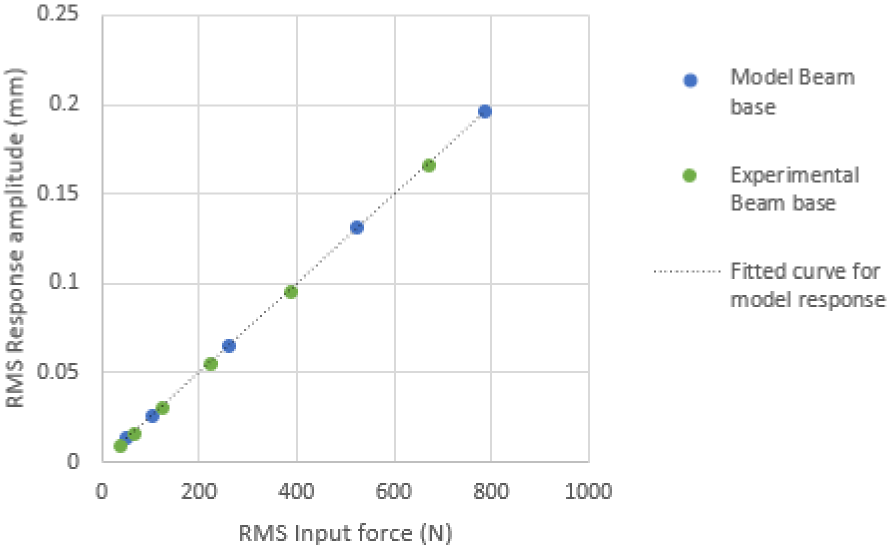

Figure 4.17 Comparison between model and experimental mean displacement amplitude results measured at the output end of the reference beam.

Figure 4.18 shows frequency spectra for the response at the output end of the reference beam for two input levels. In both cases, a close correlation between experimental and model results is shown for frequencies below 100 Hz. A broad valley appears in model results at around 200 Hz that does not appear in experimental results. This is likely due to the reference masses being attached to the top of the host beam in the experimental setup, whereas in the model, they are centred on the relevant beam node. This has the potential to create a small rotational resonance effect. The influence of interactions between struts and the host-beam is discussed further in section 4.3.3.3.

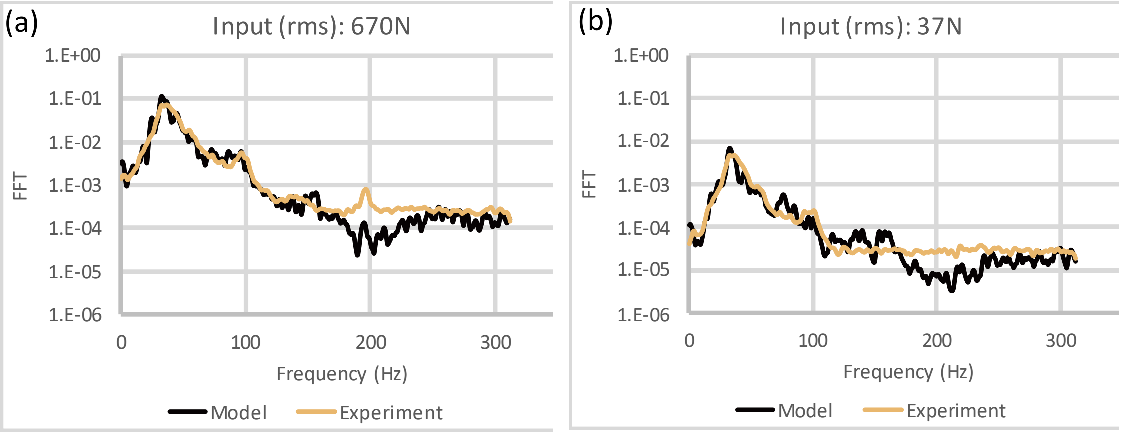

Figure 4.18 Comparison of model and experimental frequency spectra for the vibration response recorded at the output end of the reference beam for (a) the highest input level (670 N RMS) and (b) the lowest input level (37 N RMS).

4.3.3.2 Time-frequency analysis

To assess the development of the response for the full model over time, a time-frequency analysis is carried out. To achieve a high time-domain resolution for time-frequency spectra requires a consideration of short segments of the time history. For low frequencies, only a very small number of complete oscillations may be observable in a given time segment, and a trade-off between time and frequency domain resolution becomes unavoidable. A number of approaches are available which seek to maximise the resolution frequency information that can be derived from short time segments. A detailed description of the mechanics of these is beyond the scope of this article but a brief explanation of their relevant advantages and disadvantages follows.

Autoregressive methods are capable of estimating the frequency content of finite signals as if they were infinite and offer high-resolution in the frequency domain for short duration time series. However, their effectiveness relies on the calculation of model parameters and careful selection of the number of poles. This can lead to an amplification of noise in the signal [199]. Wavelet analysis methods can be thought of as windowed Fourier transform techniques that employ a frequency-dependent window width. The advantage of this approach is that they can achieve good high-frequency resolution from short-duration time series without the tendency to amplify noise, but they are not efficient for estimating low-frequency content from short-duration time series due to the widening of the window at low frequencies. Windowed Fourier transform approaches also avoid noise amplification and, due to their frequency-independent window width, offer a better resolution for low frequencies than Wavelet methods [199].

A windowed Fourier transform algorithm is therefore employed for time-frequency analyses in this study. Gaussian, Hann, Blackman, and Kaiser-a window shapes were compared, and the Gaussian window was found to provide a more consistent combination of temporal and frequency resolution in the frequency range of interest. Analyses were carried out using the PyModa software library [200]. Results (shown in Figure 4.19) show a significant change in the output signal from 0.3 to 0.4 seconds, decreasing to only a very small change from between results for 0-0.7 and 0-0.8 seconds. This suggests that a simulation time of one second is appropriate for steady-state analysis of this system as this is sufficient to provide temporal results up to approximately 0.8 seconds.

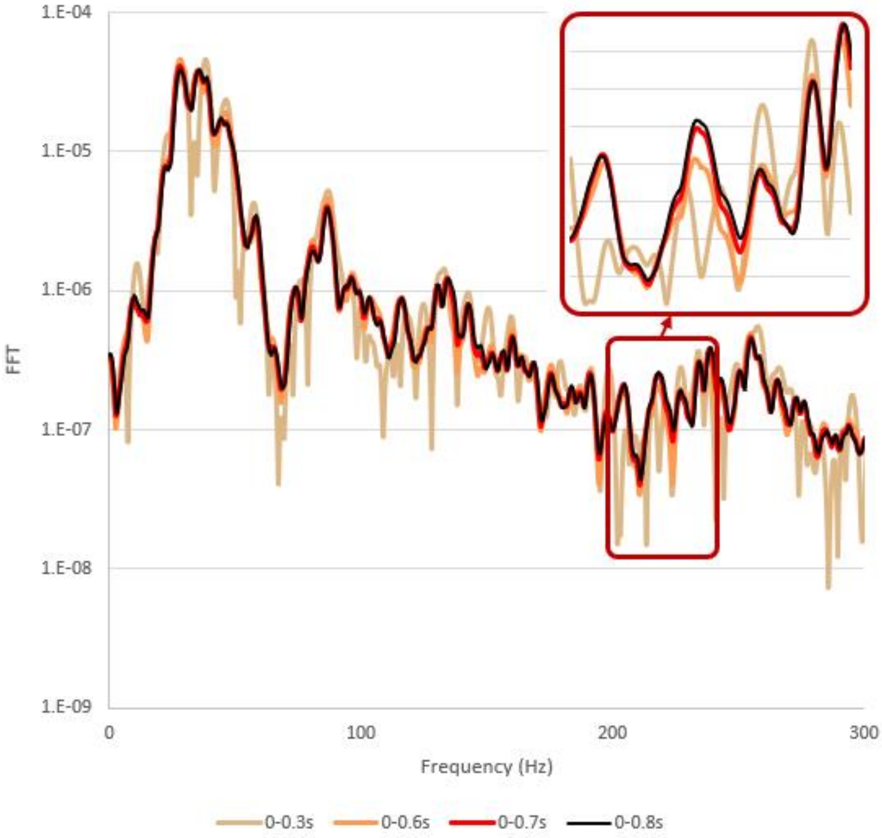

Figure 4.19 Time-frequency analysis results showing frequency spectra recorded at the tip of the meta-beam for four different simulation durations.

4.3.3.3 Metabeam response

Figure 4.20 (a) compares model and experimental results for the frequency response measured at the output end and transfer function for a five-strut metabeam excited at the highest input level (670 N). The transfer function (Y) is defined by the following relationship:

$$Y = 20log_{10}\left(\frac{fft_{output\ end}}{fft_{input\ end}}\right)(dB) \tag{4.21}$$

A reasonably good correlation is shown in both cases. The frequencies of the major peaks and troughs show close alignment, the magnitude of frequency spectra is similar across the frequency range and the general shape of the transfer functions is quite similar. In the experimental frequency spectrum, the first resonance peak is of lower amplitude and broader frequency range than the same peak in the model results, and deep bandgaps appear at around 5 and 70 Hz. Corresponding bandgaps in the experimental spectrum are evident but shallower. These differences are made more evident in the transfer function shown in Figure 4.20 (b).

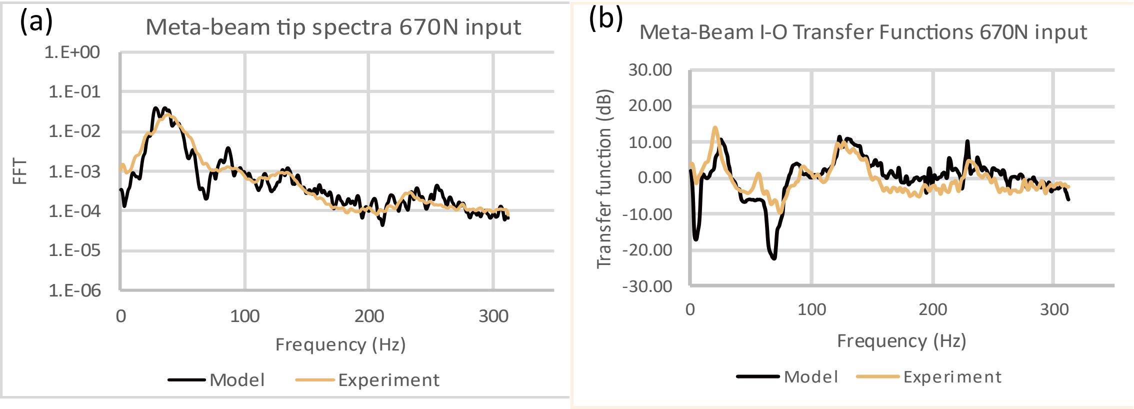

Figure 4.20 (a) Frequency spectra and (b) transfer functions comparing model and experimental displacement vibration response data recorded at the output end of the five-strut meta-beam for beams excited at the highest input level (670 N RMS)

To identify the cause of these bandgaps, the effects of lateral strut motion and vertical spring motion are considered separately. Figure 4.21 compares transfer functions for three configurations: (1) the reference beam with lumped masses only, (2) a metabeam with the resonator magnets fixed to the strut, and (3) a metabeam with the resonator magnets free to move vertically but constrained laterally and rotationally. By considering the reference beam response as a baseline, first, the fixed resonator configuration shows the effect of adding lateral strut motion and then, the free vertical resonator magnet configuration shows how the response changes with the addition of the magnetic spring motion. This reveals that the 70 Hz bandgap is associated with lateral strut oscillation and the 5 Hz bandgap is due to the vertical spring motion. This suggests that the deep bandgap at 70 Hz is likely due to a difference in the way the struts interact rotationally with the beam between the model and experimental setup. This might be associated with friction or some

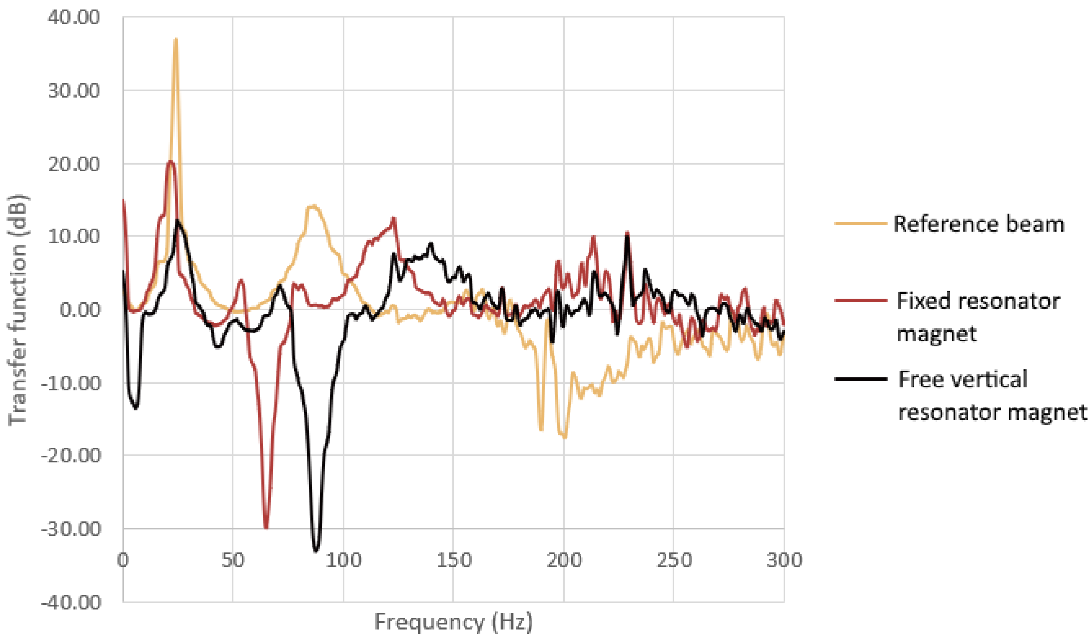

Figure 4.21 Comparison of reference beam transfer function (here referred to as 'Low strut rotational inertia') with transfer functions for beam configurations designed to isolate the causes of deep bandgaps appearing at 5 and 70 Hz (90 Hz in the case of the strut with vertical spring motion due to the reduced effective mass of the strut)

other relative motion effects in the threaded experimental prototype connection not captured by the model.

Finally, Figure 4.22 compares model and experimental results for the frequency response measured at the output end and transfer function for a five-strut metabeam excited at the lowest input level (37 N). Once again, reasonable correspondence is shown between model and experimental frequency spectra, with variations generally similar to those discussed in relation to results for the 670 N input (Figure 4.20). In the transfer functions, a couple of points are worth mentioning. Firstly, the depth of the attenuation shown in the model results is significantly larger than that in the experimental results. Further, while the experimental attenuation depth is lower at the lower input magnitude, the model attenuation depth is not. Secondly, the large peak, which appears around 140 Hz for both model and experimental results in the highest input case (Figure 4.20), has decreased in size and frequency for the experimental results in the lowest input case (Figure 4.22). It would therefore appear that the model captures the behaviour of the system more accurately for higher inputs.

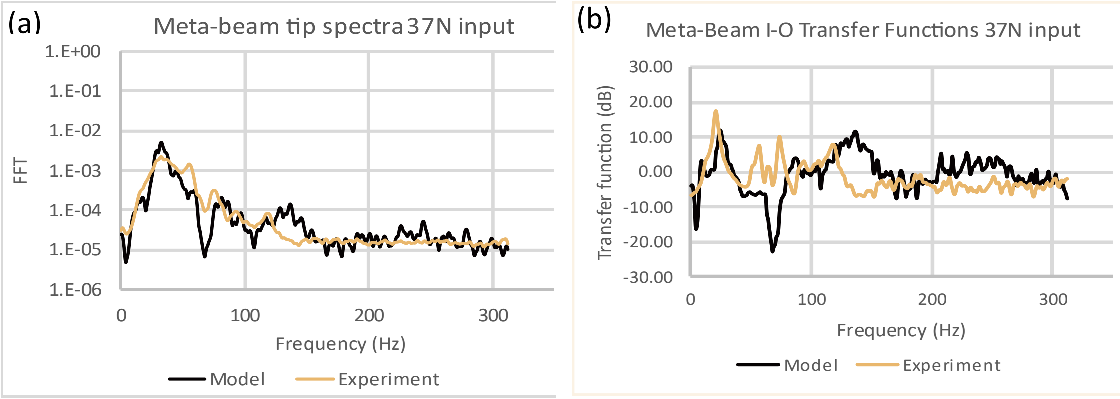

Figure 4.22 Comparison of model and experimental (a) frequency spectra for the vibration response recorded at the output end of the five-strut meta-beam and (b) transfer functions, for beams excited at the lowest input level (37 N RMS)

4.4 Conclusions

This paper describes the development and experimental validation of a numerical model for the simulation of a highly nonlinear multi-resonator metabeam. The metabeam system employs magnetic spring-based coupled vibro-impact oscillators, which introduce high levels of nonlinearity into the system’s vibration response. This has been shown experimentally to have the effect of broadening the attenuated low-frequency band.

The model comprises a two-dimensional Euler-Bernoulli beam structure coupled with a series of magnetically suspended, rigid body oscillators which interact with the structure via repulsive magnetic forces and Hertzian contact interactions. Transient motion is integrated over time using a central difference time-stepping regime.

To validate the model, a staged approach was taken whereby model sub-components were first constructed and compared with either experimental or high-resolution finite element model results. In this way, the structure of the model was built up and progressively validated before the full multi-resonator structure was compared with experimental results.

The model’s results show a high level of correlation with experimental results for beams excited at the highest input level (670 N RMS). Both frequency spectra and transfer functions show a generally good correspondence with experimental results. The model overestimates the depth of a bandgap associated with lateral strut oscillations but predicts its frequency well.

A comparison of constrained oscillator configurations with reference and meta-beam configurations suggests that attenuation in the frequency range of interest is affected significantly in the model by the presence of vertical spring motion and only slightly by the addition of resonator-strut impacts. This is contrary to findings reported in [15, 16] and warrants further investigation. However, in a broader sense, the developed model effectively predicts the broadband attenuation in the same frequency range as is shown by experimental results and reported in [15]. This suggests that the model, in its current form, can be expected to offer useful insights into the effects of future configuration variations for simulation responses to larger input levels.

Chapter 5. Numerical investigation of full-scale floor section

5.1 Introduction

In Chapter 4, the development and experimental validation of a numerical model for simulating a system comprising a two-dimensional elastic structure with multiple magnetically suspended vibro-impact oscillators attached was described. In that work, a small-scale cantilever beam with attached nonlinear resonators was transversely excited at its constrained end by a continuous random vibration input. The model showed good correlation with experimental results within a certain range of input magnitudes. This chapter investigates the potential for the developed nonlinear vibro-impact-based resonator concept to attenuate transient vibration arising from an impact input applied to a full-scale section of a floor structure with the mass and stiffness of a timber floor.

Some previous work has been directed towards the potential for locally resonant metamaterials to attenuate structure-borne sound and vibration in structure-scale real-world systems; however, most of that work has used small-scale models and prototypes for testing. Sangiuliano [201] investigated a linear, locally resonant design for attenuating road noise entering the interior cabin of a car via the suspension assembly by attaching metamaterial patches to the rear shock towers. The system was shown to attenuate frequencies between 185 and 200 Hz as effectively as existing systems but with less weight. Nateghi et al. [202] investigated the potential for metamaterial designs to improve the noise and vibration behaviour of pipe systems and achieved effective attenuation in the 800 – 885 Hz frequency by adding small locally resonant attachments to the exterior surface. Jagodzinski et al. [203] numerically improved structure-borne sound attenuation in a honeycomb-core sandwich panel design with tuned vibration absorbers installed by minimizing surface velocity. Mitchell et al. [121] investigated the potential for a locally resonant 'metaconcrete' floor structure concept to mitigate explosive blast load stress by adding resilient cells encapsulating steel balls into the concrete matrix. On a larger scale, Zhong et al. [123] investigated the vibration response of a 100 m long metamaterial I-girder in the context of a steel beam and cable-stayed bridge. They found that bandgaps were produced to the right of the resonant frequency of installed absorbers and that the width of the bandgaps could be increased by increasing damping in the absorbers.

Previous work investigating the effects of the type of coupled nonlinear resonator system being investigated here, including that described in Chapter 3, has been limited to small-scale prototypes (on the order of one-metre length) and focused on the ability of systems to attenuate steady-state inputs [15, 16]. However, no previous work has investigated transient response or prototypes on the scale of a structural floor system. Transient response to impacts is important in the context of structure-borne noise in buildings because footfall impacts are the predominant source of problematic excitation [22, 23].

In this study, the potential for a structural-scale resonator system to rapidly attenuate impact-induced 20 – 120 Hz vibrations in a timber floor is investigated. The effects of parameters affecting the practicality of the system are studied, and lower limits for the size and mass of resonators are investigated. The best performing configurations show a reduction in mean surface velocity power spectrum response of 88% in the frequency range of interest, and the time taken for reverberations to decay is significantly reduced. Increasing rotational inertia shows the most significant effect on improving performance.

5.2 Methodology

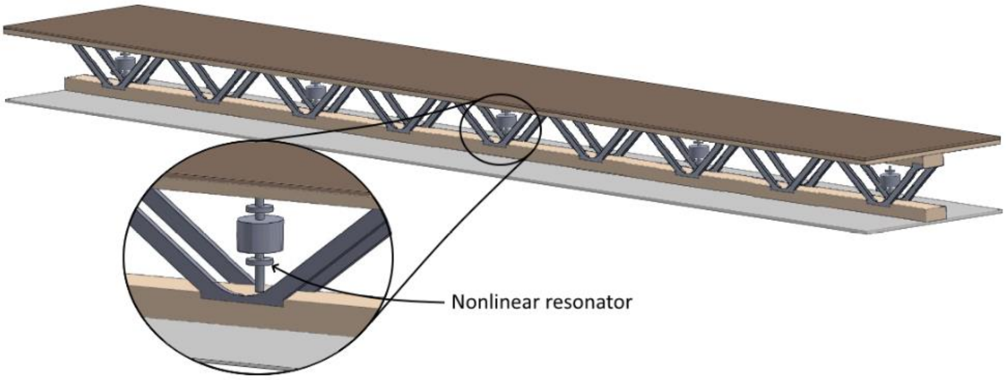

Figure 5.1 Concept illustration of timber floor beam section with nonlinear resonators installed.

To illustrate the timber floor system investigated in this chapter, Figure 5.1 shows the metamaterial structure upon which the numerical model's parameters are based. The host structure is a 600 mm wide section of an industrially produced modular floor cassette comprising a single, centrally located, open-web timber truss, with 22 mm particleboard, carpet or vinyl floor covering above and 10 mm particleboard ceiling below. The mass per unit length of this structure is 30 kg/m, and its flexural stiffness is 0.828 MNm^2 – one fifth that of a 6 x 3 m floor cassette designed to deflect according to serviceability requirements set out in AS ISO 1170[8].

To investigate the metamaterial floor system's potential for attenuating low-frequency structure-borne sound, the structure is simplified as a simply-supported beam with five orthogonally attached resonators evenly distributed along its length (Figure 5.2) and the squared surface velocity is compared with reference structures in which locally resonant elements are replaced with equivalent lumped masses.

---

[8] From discussions with practicing engineers from the industry, six-meter spans are considered as an approximate threshold above which the vibration response and natural frequency of a floor cassette become critical.

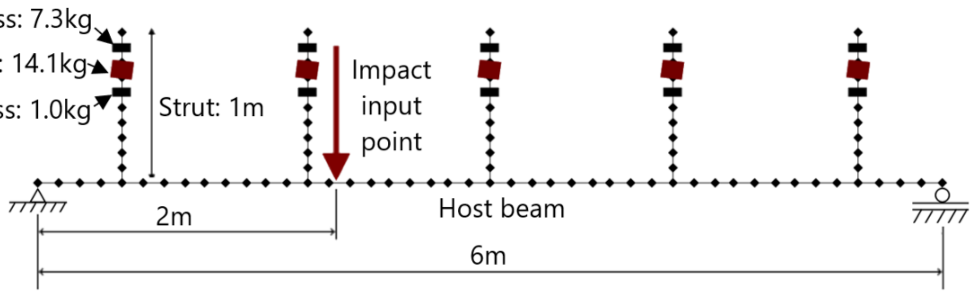

Figure 5.2 Schematic showing baseline metamaterial floor structure configuration dimensions and material properties

Validation of the model used in this study was presented in Chapter 4. The model comprises a two-dimensional geometry employing Euler-Bernoulli plane frame elements with lumped masses and rotational inertias added to relevant degrees of freedom for the fixed masses in the structure. Suspended-magnet resonators are modelled separately as rigid bodies, and interaction forces between resonators and structure are calculated at each time step. These then serve as inputs to each body at the next time step. A central difference time-stepping scheme is employed to solve the system. Host structure elements are assigned a material density of 510 kg/m^3, cross-sectional area of 0.059m^2, Young's modulus (E) of 10 GPa and second moment of area (I) of 8.28e-5 m^4. This leads to a mass per unit length of 30 kg/m and a flexural stiffness (EI) of = 0.828 MNm^2.

The structure is simply supported and excited at a point, one-third of the length of the host structure from its end, by a short-duration time-varying force (***F***). The time-varying magnitude of the impact force is modelled as a Hanning function according to the following relation:

$$\boldsymbol{F} = -\frac{1}{2}P\left(1 - cos\left(\frac{2\pi t}{T}\right)\right)\ (N) \tag{22}$$

where P is the peak magnitude of the impact, t is time with respect to the start of the impact, and T is the duration of the impact. This shape has been shown to be a good approximation for footfall impacts [204] and, in this study, is manipulated to provide appropriate excitation for the frequency range of interest. For impacts in this study, the peak magnitude (P) is set at 10 kN, and the duration (T) is set at 2e-3 s. The duration is set to ensure that frequencies in the full range of interest are excited, and the peak magnitude is set to produce a maximum host structure displacement of one millimetre. A detailed description of the implementation of the model and solution procedures used can be found in Chapter 4.

5.2.1.1 Resonator assemblies

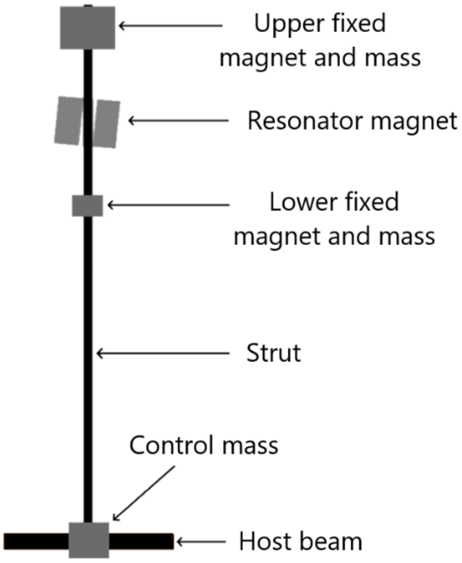

Figure 5.3 Schematic of resonator assembly comprising a stainless-steel strut that supports a magnetic spring.

A schematic of a resonator assembly is shown in Figure 5.3. Each assembly comprises a stainless-steel cantilever strut that supports a magnetic spring assembly close to its upper end. Each spring assembly comprises two variable, fixed masses (upper and lower), which each support a ring magnet with a magnetic field axially aligned along the cantilever. A third, suspended ring magnet with its magnetic field opposing those of the fixed magnets is suspended between them. In the model, the combined mass and rotational inertia of each fixed mass/magnet pair are added to a single node. For each simulation, the stiffness of the cantilever is adjusted depending on the combined mass and rotational inertia parameters of the cantilever and fixed magnets to maintain a constant fundamental frequency of 115 Hz for the lateral oscillation of the whole assembly.

The magnetic force acting on the suspended resonator magnet is estimated as the sum of two separate forces acting from the fixed magnets above and below. The force-displacement curve acting on the resonator from the lower magnet is specified as:

$$F_{lower} = k_{linear}x + k_{nonlinear}x^3 + C \qquad x < 0$$

$$F_{lower} = Ce^{-ax} \qquad x \geq 0 \tag{23}$$

where x is the vertical displacement of the resonator with zero being at its central resting position and up being positive, C is the force acting when the resonator is at rest and k_{linear} and $k_{nonlinear}$ are the linear and nonlinear spring stiffness coefficients, respectively. Similarly, the force acting on the resonator from the upper magnet is specified as:

$$F_{upper} = -(k_{linear}x + k_{nonlinear}x^3 + C) \qquad x \geq 0$$

$$F_{upper} = Ce^{ax} \qquad x < 0 \tag{24}$$

The sum of these forces closely approximates the cubic force curve of a duffing oscillator:

$$F_{total} = k_{linear}x + k_{nonlinear}x^3 \tag{25}$$

Opposing forces are also applied to the vertical degrees of freedom of the fixed magnets. The resulting force-displacement curves acting on the resonator are shown in Figure 5.4 for $k_{linear} = 1.2\text{e}6$ N/m, $k_{nonlinear} = 1\text{e}11$ Nm^{-3}, and $C = 100$ N.

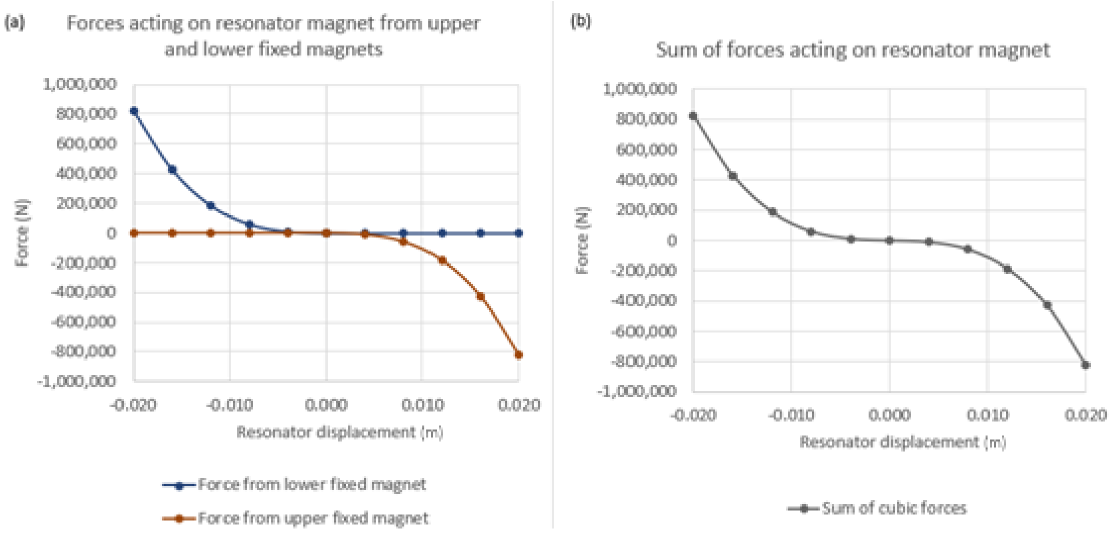

Figure 5.4 Force displacement curves for forces acting on resonator magnet. (a) Individual forces acting from fixed magnets above and below and (b) the sum of those forces produces a curve that closely approximates that of a duffing oscillator.

5.2.1.2 Metamaterial floor structure configurations

The effects of five parameters on the vibration response of the floor structure are investigated in this study: impact driving amplitude, the rotational inertia of resonator assemblies, the mass of resonator assemblies, the mass of resonators and spring stiffness. As a starting point, parameters for a 'baseline metamaterial structure configuration' are derived by approximately scaling the length, mass, and rotational inertia of the small-scale system studied in Chapter 4. The stiffness of the cantilever and the linear spring stiffness coefficient are then adjusted to maintain fundamental frequencies of lateral strut oscillation and magnetic spring motion of 115 Hz and 25 Hz, respectively. Resonator parameters for the metamaterial reference configuration are shown in Table 5.1.

Table 5.1 Resonator assembly parameters for the metamaterial reference configuration

	Length (m)	**Mass (kg/m)**	**Stiffness (EI) (Nm^2)**
Strut	1	1	1.16e6
Spring masses	**Height (m)**	**Mass (kg)**	**Rotational inertia (kgm^2)**
Lower mass	0.712	1	1.53e-3
Upper mass	0.95	7.29	1.03e-2
Resonator	0.811	14.08	3.35e-2
Control mass	0	7.29	0

To vary the spring stiffness, the linear component of the cubic spring stiffness equation is adjusted, and the mass of the resonator magnet is left unchanged. Changes in spring stiffness, therefore, coincide with changes in the linearised natural frequency of the magnetic spring. For the reference configuration, the linear spring stiffness is 8e5 N/m. Twelve stiffness levels between 1e4 and 3e6 N/m were tested.

To vary resonator mass, the linear spring stiffness is adjusted to compensate for each change of mass and maintain a constant linearised natural frequency for the magnetic spring. Five different resonator masses between 5.6 and 22.5 kg were tested.

To investigate the effects of varying the length and mass of the whole resonator assembly, three separate parameters were identified for investigation. Firstly, the impact driving amplitude (IDA) is defined as the amplitude of lateral strut oscillation at the point of contact between the strut and impacting resonator magnet. This amplitude varies with the distance of the contact point from the base of the strut. IDA, therefore, varies with the length of the strut. In Chapter 3, a higher IDA was found to correlate with better attenuation performance. However, due to practical limitations with the physical embodiment in that study, it was recognized that varying the IDA coincided with unavoidable changes in the total mass and rotational inertia of the resonator assembly. This was due to the additional requirement that the strut's natural frequency be maintained, which necessitated the use of the upper mass for frequency control.

In this study, each of those parameters is varied independently as follows:

- To vary IDA: the length of the strut is varied between 0.79 and 1.456 m, the upper mass is then varied to maintain the same rotational inertia, and the control mass is varied to maintain constant total mass.
- To vary rotational inertia: the upper mass is varied, then the control mass is adjusted to maintain constant total mass and strut length is left unchanged.
- To vary the total mass of resonator assembly: only the control mass is varied.

Frequency is then controlled by varying the strut's stiffness without varying its mass. While this is not practical in a physical sense, it is useful for the purpose of isolating each parameter.

For each metamaterial floor structure configuration, an associated reference structure with lumped masses in place of resonators is also included in the study. Each lumped mass is located on the host structure at the node to which a resonator is attached in the metamaterial structure, and its mass is equivalent to that of the whole resonator assembly.

5.2.2 Data analysis methods

In Chapter 3, the potential for improving structure-borne sound performance was considered from the perspective of transverse structural vibration measured in terms of displacement amplitude. This is a reasonable point of departure since previous work has shown attenuation levels to be dependent on displacement amplitude, and further, a reduction in displacement amplitude in the source structure will clearly lead to a vibration reduction in structural pathways leading to radiating surfaces in receiving rooms. In this chapter, the potential for the vibrating floor structure to be a sound radiator itself is also considered. The formal approach for estimating the sound power radiation from a vibrating surface is to calculate the acoustic field by simulating the interaction between the surface and the surrounding air [205]. A range of simplified methods that avoid the need to simulate fluid-structure interaction also exist for estimating sound power radiation with varying levels of complexity [203, 206-208]. However, the reliability of those methods is low for low frequencies due to difficulties associated with accounting for self-cancellation effects around modal node lines that were discussed in Section 2.2.4 [207]. As was discussed in Chapter 1, that level of simulation is beyond the scope of this investigation, but common among the methods mentioned above is a recognition that the magnitude of sound power radiation correlates with the squared magnitude of the normal velocity of the radiating surface.

The goal of this investigation is to assess variations in structure-borne sound between prototypes. The prototypes being compared are representative of real floor systems that will have identical exterior surfaces when manufactured (i.e., the addition of any resonators will always be inside the structure and therefore not affect surfaces that radiate sound). The radiation efficiency can therefore be considered to be identical between them. Therefore, a meaningful comparison of structure-borne sound performance can be made by comparing the squared magnitude of the structure's surface normal velocity. When used as the basis for frequency analysis, this becomes the surface velocity power spectrum. The relationship between structural vibration and sound radiation is discussed in Section 2.2.4, and the role of surface velocity is shown in Equation (2.3).

For each simulation, normal surface velocity is therefore recorded at the impact input point and at a point one-third of the structure's length from the right-hand end. To estimate the response of the structure, the mean of the squared velocity at each measurement point is used for comparisons. Frequency spectrum calculations and time-frequency analyses are carried out using the windowed Fourier transform method with a Gaussian window function discussed in Chapter 4, Section 4.3.3.2. This method provides a good combination of temporal and frequency resolution for the frequency range of interest without adding noise to the recorded response. The PyModa Python software library is used for frequency and time-frequency calculations [200].

5.3 Results and discussion

In this section, numerical results investigating the influence of linear spring stiffness, resonator mass, and the mass, rotational inertia, and length of resonator assemblies on the performance of a nonlinear metamaterial design for the attenuation of 20 – 120 Hz structure-borne sound in a 6 m long, 0.6 m wide section of timber floor are discussed.

5.3.1 Baseline metamaterial structure response

First, the response of the baseline metamaterial structure configuration is considered. This is the structure with resonator parameters set to values around which variations are made in later tests. It is shown in Figure 5.1 and described in section 5.2.1.2.

Figure 5.5 shows the surface velocity power spectrum for the baseline metamaterial structure configuration and its associated reference beam. Recalling that the frequency range of interest for lightweight timber floors is 20 – 120 Hz, this and subsequent graphs show the response for that interval, including frequencies 20 Hz to either side. The mean magnitude of the velocity power spectrum over the 20 – 120 Hz interval is 1.49e-7, 88% smaller than that for the reference structure (1.22e-6). The amplitude of the two main resonant modes in the reference structure response (at approximately 8 and 20 Hz) are considerably reduced in the metamaterial structure response. The frequency of the mode close to 20 Hz is also shifted slightly lower (and out of the interval of interest) in the metamaterial structure response, which contributes to the reduction in the mean value. There is also a new resonant mode appearing in the metamaterial structure response, at approximately 43 Hz which is associated with the nonlinear response of the magnetic spring (discussed in section 5.3.3). This pattern is representative of what is seen in subsequent metamaterial structure results.

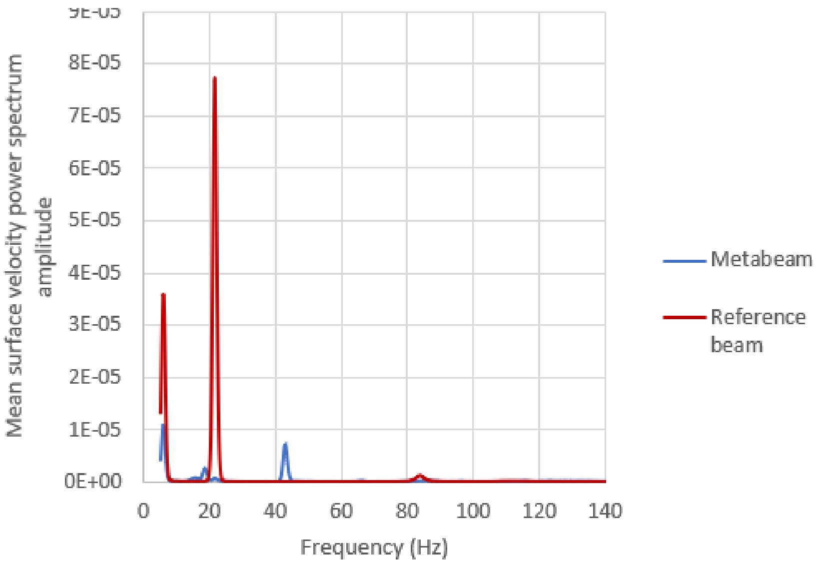

Figure 5.5 Surface velocity power spectra for the baseline metamaterial structure configuration and its associated reference structure.

5.3.2 Time-frequency analysis

To investigate how the signals change over time, Figure 5.6 compares time-frequency representations for (a) the baseline metamaterial structure configuration and (b) its associated reference structure for the one-second duration of simulations.

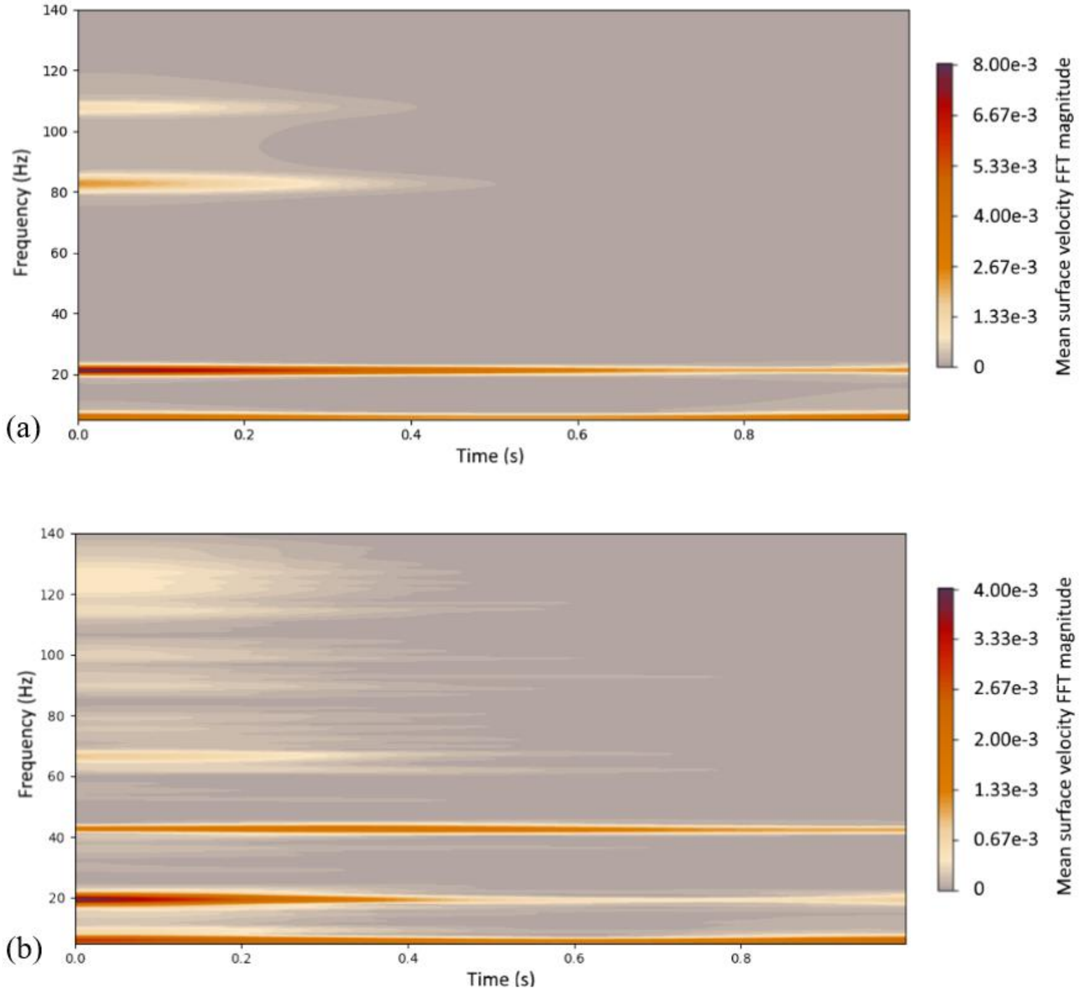

Figure 5.6 Time-frequency representations showing the surface velocity FFT magnitude of (a) the reference structure with lumped masses equivalent to the total mass of resonator assemblies in the baseline metamaterial structure configuration and (b) the baseline metamaterial structure configuration.

There is a significant difference in the decay rates for the peaks around 20 Hz between the meta- and reference structures. Aside from being less intense, the peak in the metamaterial structure decays considerably more quickly. The vibration energy is also more dispersed across the frequency range than in the reference structure response, indicating an energy flow from mode two to mode three. The reduction in the surface velocity of the metamaterial over that of the reference structure results from both lessened intensity and shortened duration in the transient signal.

5.3.3 Effect of spring stiffness

The force-displacement curve is implemented in the model as a cubic function with a linear component. To vary the spring stiffness for the purpose of these comparisons, the nonlinear component is left unchanged, and the linear component is varied between 1e4 and 3e6 N/m. Considering that the mass of the resonator is approximately 14.1 kg, this correlates with linear resonant frequencies ranging from approximately 26 to 460 Hz.

The mean value for frequency spectra of metamaterial structures supporting resonator assemblies with twelve different linear spring stiffnesses, and the associated reference structure, is shown in Figure 5.7. Better attenuation is seen for configurations at the high and low ends of the tested spring stiffness range. In Figure 5.8, this can be seen to be due to the changing amplitude of the mode associated with the presence of the resonator, which was mentioned in relation to the baseline response shown in Figure 5.5. The frequency of that mode increases with increasing spring stiffness, and the amplitude rises to a peak around 43 Hz before falling away. This mode is associated with the nonlinear

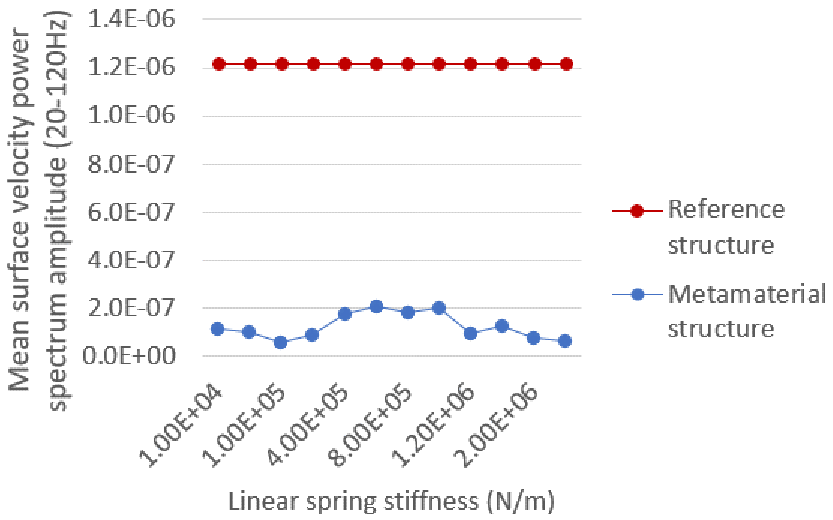

Figure 5.7 Mean surface velocity power spectrum amplitude for metamaterial and reference structures for each frequency response in the 20 – 120 Hz interval for twelve different linear spring stiffnesses.

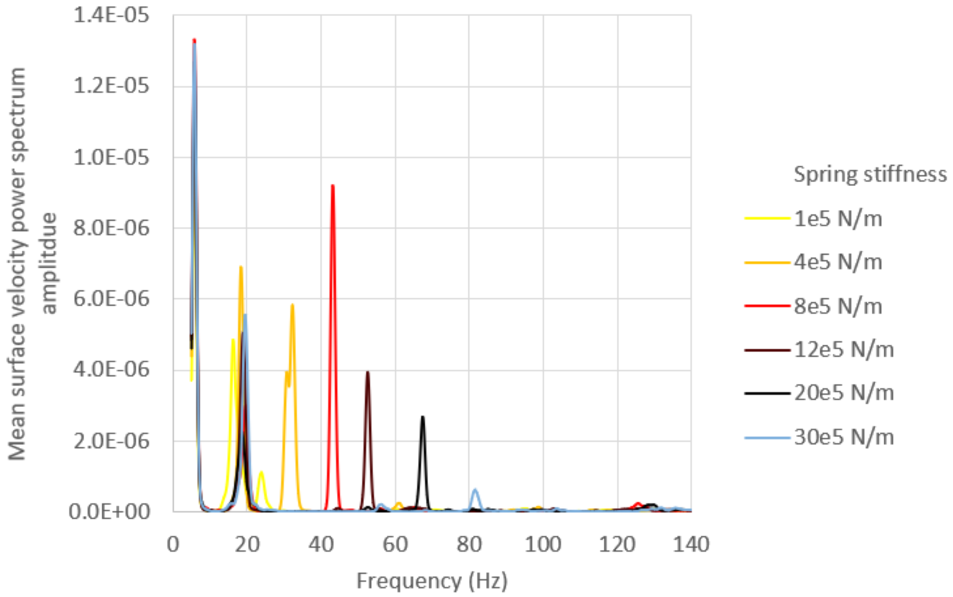

Figure 5.8 Surface velocity power spectra for metamaterial structures with six different linear spring stiffnesses.

response of the magnetic spring, and interesting to note that the largest amplitude reduction of that mode is achieved with the highest spring stiffness (460 Hz).

To investigate this further, Figure 5.9 shows frequency spectra for the vertical displacement of a single resonator with the same six spring stiffnesses shown in Figure 5.8. As the spring stiffness increases, the amplitude of the resonator response decreases, and its frequency response widens. Resonance modes also approximately coincide with those in the host structure response (Figure 5.8). The lower end of the resonator's response is largely unaffected for spring stiffness higher than 8e5 N/m. This suggests that the lower bound of the attenuation band may not be determined by the linearised spring stiffness, as is suggested in [15], but rather by the lower end of the oscillator's nonlinear subharmonic response. Further, by extending the upper end of this response into higher frequencies, the degree of nonlinearity is increased, and an associated improvement in attenuation is observed.

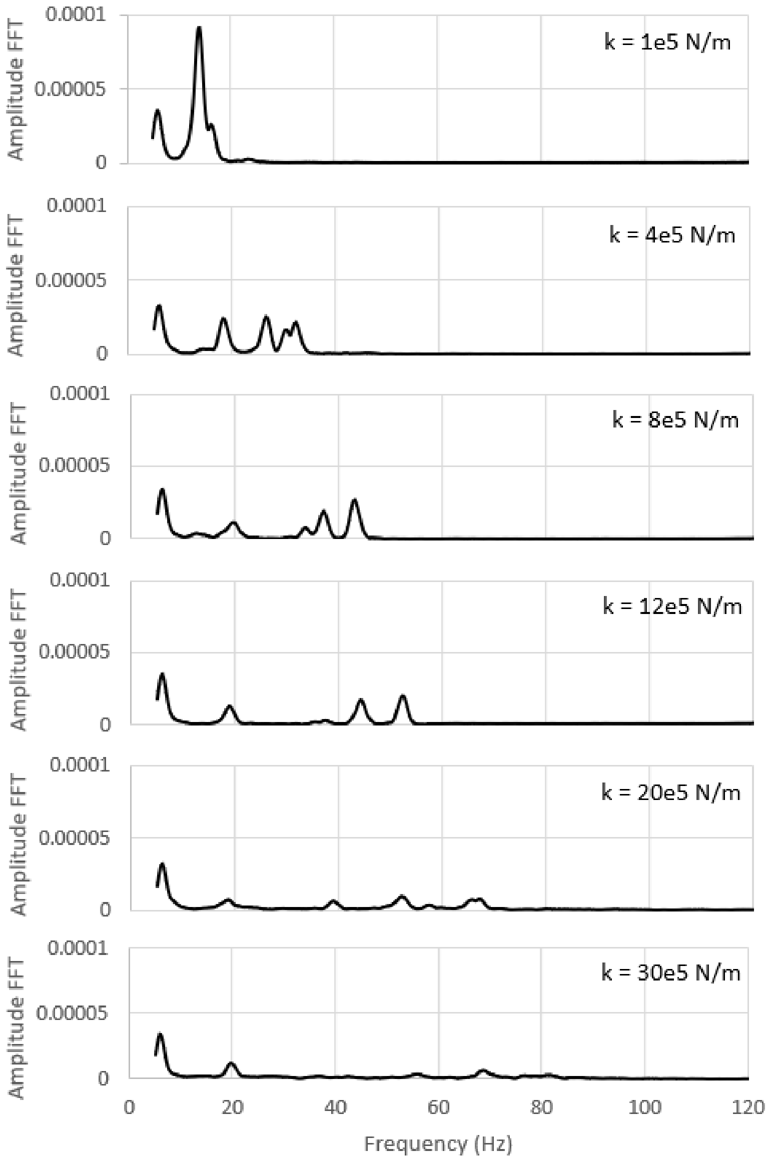

Figure 5.9 Displacement frequency response for vertical motion of a single resonator for six different linear spring stiffnesses.

5.3.4 Effect of resonator mass

To maintain a constant linearised natural frequency for the magnetic spring, changes in resonator mass were compensated for by adjusting the linear component of spring stiffness. The mean value for frequency spectra of metamaterial structures with five different resonator masses and their associated reference structures is shown in Figure 5.10. For the metamaterial structures, though a strong trend is not evident, the best attenuation is seen for the 11.3 kg resonator, and as the resonator mass increases, the effectiveness of the attenuation decreases. This result runs counter to an expected correlation between mass and attenuation that warrants further investigation. For the reference structures, a clear trend is evident. As expected, the magnitude of the mean response decreases with increasing mass.

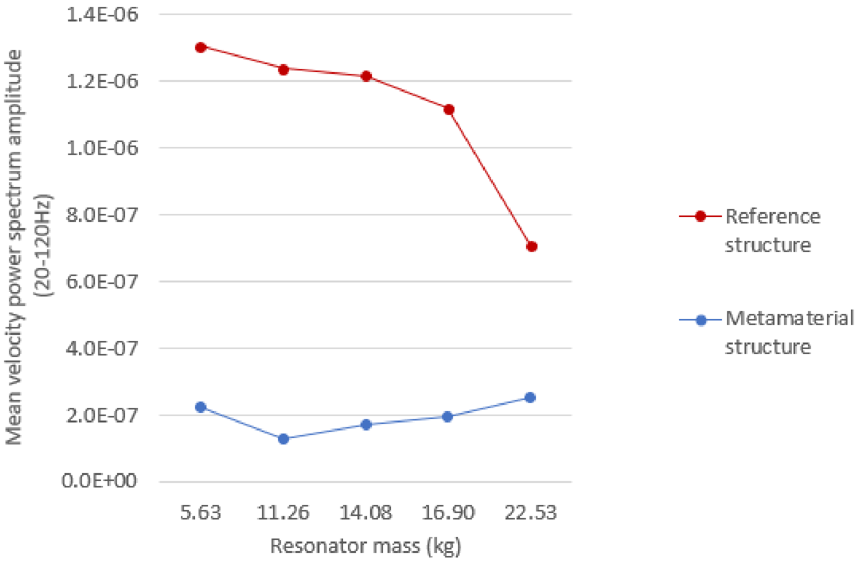

Figure 5.10 Mean surface velocity power spectrum amplitude in the 20 – 120 Hz interval for metamaterial structures with five different resonator masses and their associated reference structures.

Figure 5.11 shows the surface velocity frequency spectra for the same five metamaterial structures referred to in Figure 5.10. It is evident that the largest effect of the varying resonator mass occurs in the first resonant mode, below the frequency range of interest. Here, a clear decrease in amplitude is brought about by increasing resonator mass. A similar trend is evident for the amplitude of the resonant mode at ~20 Hz. The frequency of that mode also decreases with increasing mass. The pattern at ~45 Hz is reversed, with the amplitude of the mode increasing with increasing mass as well as the frequency.

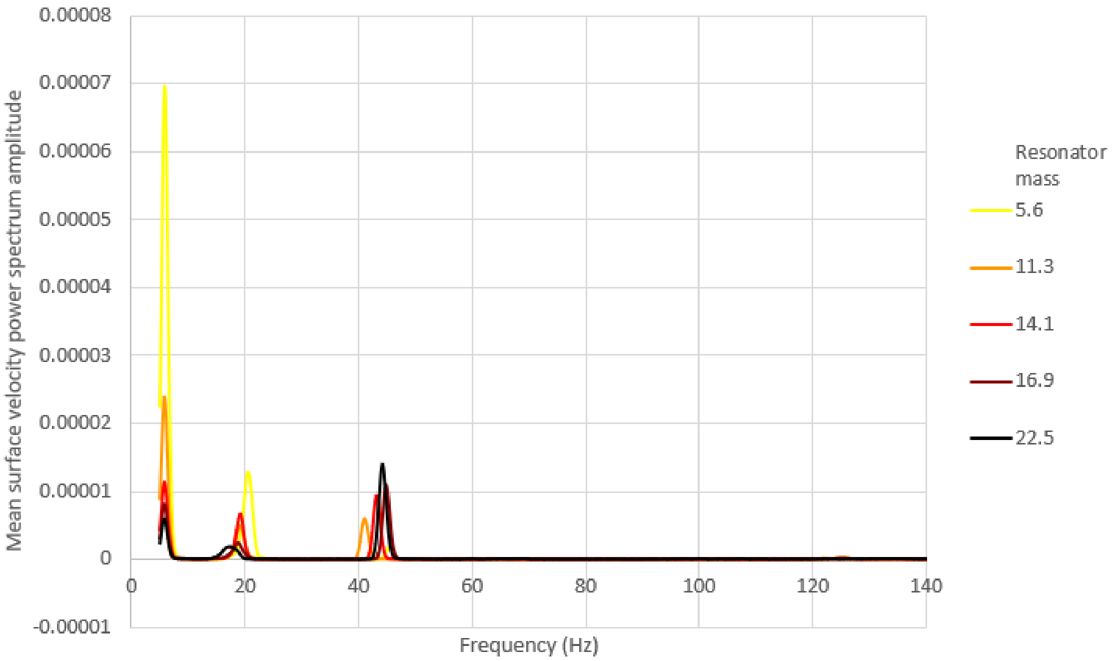

Figure 5.11 Surface velocity power spectra for metamaterial structures with five different resonator masses.

5.3.5 Effect of mass, rotational inertia, and height of resonator assembly

Figure 5.12 compares surface velocity power spectra means for metamaterial structures with (a) varying resonator assembly mass, (b) resonator assembly rotational inertia and (c) impact driving amplitude with their associated reference structures. The addition of mass to the base of the resonator does not show a strong attenuation improvement over the same addition of mass to the non-resonant reference structure. The metamaterial structure configuration with the largest mass shows the smallest response, but if the response is considered as a fraction of the reference structure response, the percentage amplitude reduction is almost identical for all configurations (80.4+-0.3%) except for the smallest mass, which shows a slightly smaller percentage reduction (76%).

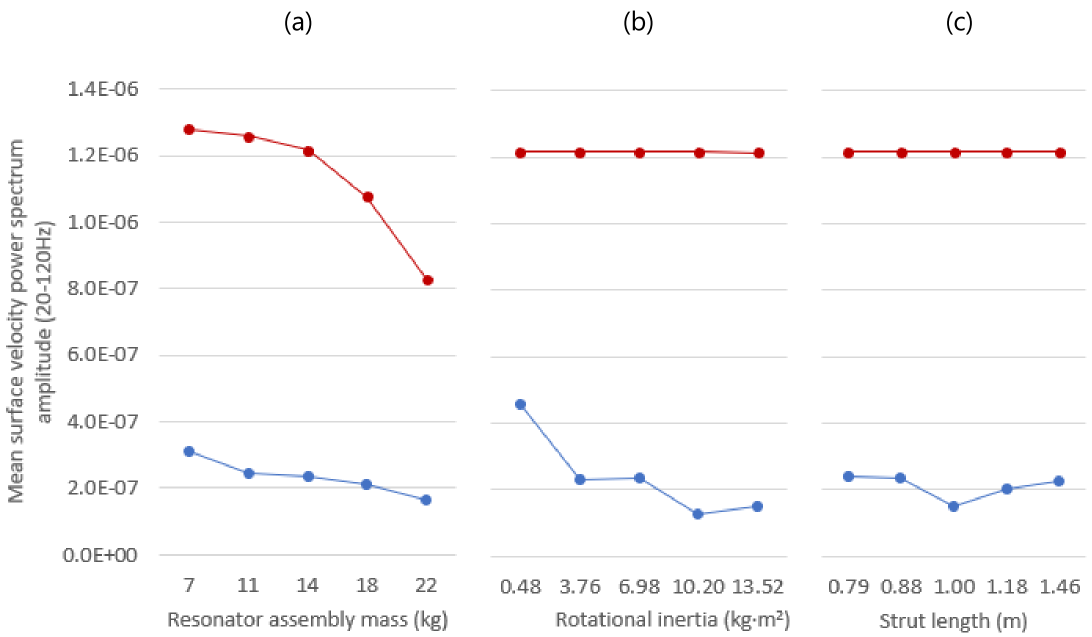

Figure 5.12 Mean surface velocity power spectrum amplitude in the 20 – 120 Hz interval for metamaterial structures with varying (a) total mass of resonator assemblies, (b) rotational inertia of resonator assemblies about the structure-strut junction, and (c) the length of the strut which governs the impact driving amplitude (IDA).

For increasing rotational inertia, a clear trend towards decreasing amplitude is evident, whereas for varying the IDA, a trend is not clear. Recall that to increase rotational inertia, the upper fixed mass is increased, and the length of the strut is left unchanged, whereas to increase IDA, the length of the strut is increased, and the upper mass is decreased (in both cases, the control mass is adjusted to maintain constant total mass).

Figure 5.13 shows the surface velocity power spectra for metamaterial structures with (a) varying rotational inertia and (b) varying IDA. In both cases, the resonant mode at ~20 Hz is significantly affected by variation of the parameters, and the mode at ~45 Hz is substantially unchanged. It is evident that the addition of mass to the system is most beneficial when it is added to the tip of the strut. This can be explained in terms of the inertial amplification effect. The increase of attenuation with increasing IDA observed in Chapter 3 is not evident in these results. This may be a result of any of several differences between the prototypes in that study and the current configurations, including differing boundary conditions, varying total resonator mass in Chapter 3, the addition of a control

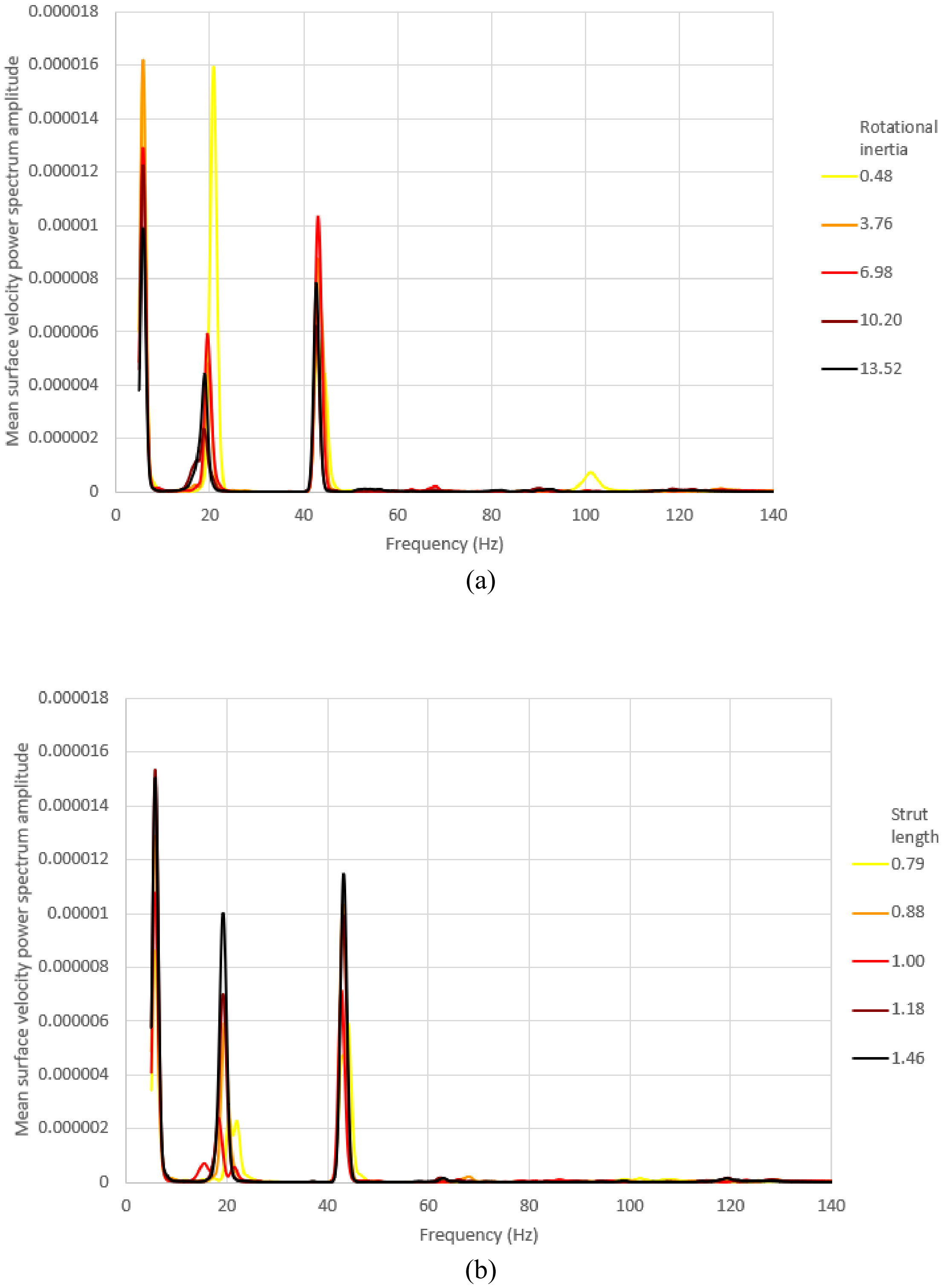

Figure 5.13 Surface velocity power spectra for metamaterial structures with (a) five different rotational inertias and (b) five different impact driving amplitudes (IDA).

mass in this study (which increases the resonator/host structure mass ratio without increasing local resonance), and variations in parametric relationships as a result of scaling.

5.4 Conclusions

In this chapter, the transient response of a nonlinear acoustic metamaterial floor structure subject to an impact input is investigated numerically to assess the potential for this type of system to attenuate structure-borne sound in the 20 – 120 Hz frequency range in lightweight floors. The system comprises a host structure with the mass and stiffness of a 0.6 m wide, 6 m long section of a light timber frame floor structure with five coupled nonlinear resonator assemblies orthogonally attached along its length. The resonator assemblies comprise a magnetic spring coupled with a vibro-impact oscillator and a weighted cantilever which acts as a torsion spring.

Parameters relevant to the practicality of the system in the context of a real floor system are investigated – including the mass, rotational inertia and length of the whole resonator assembly, the mass of resonators, and the linear stiffness coefficient of the magnetic spring. The effect of increasing the rotational inertia of the resonator assemblies is shown to increase attenuation. Increasing resonator mass shows little effect on the mean amplitude response but does significantly decrease the amplitude of the resonant mode at approximately 20 Hz.

The best performing configurations show a reduction in surface velocity amplitude of 88 % over that of associated reference structures for the frequency range of interest. Time-frequency analysis shows that the metamaterial structure response decays significantly faster than the reference structure. Along with the amplitude of the vibration response, the duration of structure-borne reverberation plays an important role in the perceived loudness of low-frequency impact sounds.

Further research is necessary to better understand the effects of changing boundary conditions and the interrelationships between the inertial, geometric, and resonant parameters that govern the way in which systems should be scaled. The findings relating to the mass and length of resonator assemblies required to achieve high levels of attenuation suggest that the geometric layout of the studied system presents challenges with respect to the constrained available space in real floor structures. Alternative geometries should be investigated in future research that might offer practical solutions to meet the limited space requirements of lightweight timber floor structures.

Chapter 6. Conclusions and Future Work

6.1 Conclusions

This work has investigated a potential alternative solution for the attenuation of 20 – 120 Hz structure-borne sound in timber floors as a method for improving sound insulation performance in multi-storey timber buildings. The approach employs multiple nonlinear vibro-impact-based resonators to absorb, counteract and dissipate broadband low-frequency vibration energy from the host structure. The system was investigated both numerically and experimentally and found to be capable of attenuating a very broad range of low frequencies in both small- and large-scale structural systems with minimal additional mass. Potential mechanisms for improving performance were investigated in the context of real floor applications, and identified improvements pointed to a need for a reconfiguring of system geometry if this type of system is to fit within the confines of a lightweight timber floor structure. Future work assessing potential alternative configurations is considered.

The challenge of attenuating low-frequency structure-borne sound in timber floors has remained an open research question for over five decades. After a wide-ranging assessment of past, present, and emerging technologies, the potential alternative approach chosen for investigation here was selected for its unique ability to rapidly attenuate low-frequency transient vibrations of small-amplitude in a broad range of frequencies and in a form factor that makes it possible for the system to be added without interfering with structural capacity – all key criteria for the solution of the research problem.

The literature shows that the effect of low-frequency impact sound on occupants is significant and that current standards for rating the performance of lightweight timber buildings are misleading. For a timber building that meets minimum requirements according to the current Australian National Building Code, research suggests that more than 40% of occupants will report high levels of annoyance, and fewer than 10% will consider themselves satisfied with the building's impact sound insulation performance. Research also shows that impact sound is considered more disturbing than other sources of noise and that frequencies down to 20 Hz are of critical importance for occupant comfort in timber buildings.

Existing construction technologies were found to be highly effective for frequencies above 120 Hz, moderately effective for frequencies down to 60 Hz, and largely ineffective for frequencies below that. Emerging metamaterial-based approaches employing local resonance were found to have great potential for deep attenuation of low frequencies but limited to narrow frequency bands in the absence of large additional mass. Mass requirements can be reduced using resonator geometries that amplify motion in response to small-amplitude vibrations in the host structure. The addition of nonlinearity to a system's locally resonant response was found to have the greatest potential for increasing attenuation bandwidth. Further, the use of internal impacts for the addition of nonlinearity was found to be specifically suited to problems requiring rapid attenuation of transient vibration events. The selected system combines each of these characteristics with a recently reported 'bridging-coupling' effect which makes it possible to dramatically broaden the attenuation bandwidth without the addition of mass.

The system was experimentally investigated using a small-scale prototype comprising an aluminium cantilever beam with five attached resonator assemblies. Results show that significant attenuation can be achieved across a broad range of frequencies. The results support previous work suggesting that the depth of attenuation depends on the degree of nonlinearity in the locally resonant response. Attenuation depth increased with input amplitude, and the best performing configurations were those that promoted high levels of vibro-impact behaviour. Conditions for this were created by high input amplitude, high spring stiffness, large impact gap size and high impact driving amplitude.

The model used to investigate the system was developed in Python using a hybrid finite element/rigid body approach. The approach was born of a need to simulate a large number of low-velocity impacts which excite high frequencies at multiple locations in a large structure. The model accurately simulates individual low-velocity impacts and two-dimensional resonator motion when compared with experimental data and a high-resolution finite element sub-structure model. It achieves a high level of correlation with experimental results for attenuation at the highest tested input levels, and it effectively predicts the broadband attenuation in the same frequency range as is shown by experimental results. The model less accurately correlates with experimental results for the lowest tested input levels and tends to overestimate the effect of lateral strut oscillation on metabeam vibration. While these limitations call for further investigation, for inputs in the range of the highest tested levels, the model offers valuable insights into system performance.

The transient impact response of a full-scale nonlinear acoustic metamaterial representing a narrow section of lightweight timber floor was then investigated numerically to assess the potential for this type of system to be applied in real lightweight floors. The best performing configurations achieved a reduction in mean surface velocity power spectrum response of 88% over that of corresponding reference beams in the frequency range of interest. Transient reverberation was significantly shortened, and energy was more spread out over the frequency range. The attenuation performance of the system was found to depend most strongly on the rotational inertia of resonator assemblies. Findings relating to minimum length requirements for resonator assemblies suggest that alternative geometric configurations will need to be developed if this type of system is to fit within the confines of a lightweight timber floor.

With respect to the original project objectives that were stated in Section 1.2.2:

- The effects of low-frequency impact sound transmission on building occupants were characterised by analysing data and conclusions from previous research in Chapter 2.
- Previous research was also studied to characterise the limitations of existing attenuation approaches and to identify a potential alternative approach for attenuating low-frequency structure-borne sound in timber buildings.
- Effects of parameters important for the selected system's potential application in timber floors were analysed experimentally in Chapter 3 and numerically in Chapter 5.
- The system was shown to be capable of rapidly attenuating broadband low-frequency vibrations in small- and large-scale structures without interfering with existing structural capacity or adding large amounts of additional mass. The approach, therefore, has good potential for helping to solve the research problem, but further research will be required to investigate the performance implications of alternative geometries required to fit resonators inside full-scale structures.

6.2 Future work

The work presented in this thesis represents a first step towards the development of a practical solution for improving sound insulation in multi-storey timber buildings by attenuating low frequencies in timber floors. To achieve that goal, further work is needed. Of primary importance is to answer the question as to whether configurations can be designed that will fit into the confines of a real floor while achieving good attenuation performance. Results so far suggest that a minimum inertial amplification effect is needed for the system to be effective. In its current form, the design concept, therefore, takes up too much space vertically. This problem might be solved by reorienting struts to be parallel to the beam or floor plate. This would dramatically increase the space available for lengthening struts. It would also open up possibilities for increasing nonlinearity by creating spring forces that act transversely to the strut.

For other work in floor systems, investigations could be extended to consider the effects of the internal structure of lightweight timber floors. Internal structural mode shapes may have implications for resonator placement due to spatial variations in rotation and translation that occur in relation to nodes and antinodes. Also, while some preliminary work has been done to assess the effects of friction between resonators and struts at the strut/host beam junction (not reported in this thesis), further work may also reveal important effects of friction on the dissipation of energy. To predict the acoustic performance of full-scale floor plates, these details will also need to be combined with an effective method for predicting the radiation of sound into the air.

While floors have been identified as the primary structural source and the largest contributor to the low-frequency sound transmission problem, the principles underlying the studied attenuation mechanism have the potential to be applied in walls, ceilings, and other elements in multi-storey timber structures. For vertical elements (walls), this work would necessitate consideration of resonator geometries that accommodate the need for vertical orientation of magnetic springs that can support low input threshold impact oscillations.

The numerical modelling approach developed for these investigations offers significant advantages in terms of its short solution times for low-velocity impacts while maintaining a detailed representation of resonator geometry. By coupling simplified structural elements with rigid bodies, low-velocity, vibration-dominated impacts can be simulated accurately and efficiently. As the potential of vibro-impacting designs for rapid broadband attenuation of structural vibration is further explored in future work, this type of approach may find application in situations where slender structures are deliberately designed to work with vibro-impact oscillators.

A wide range of configuration possibilities integrating the basic concepts of inertial amplification, impact-based nonlinearity, and bridging-coupling could be envisaged for disparate fields where broadband attenuation of low-frequency vibration is desirable. In the building construction industry, the attenuation of wind- and earthquake-induced whole building vibrations might be considered. Applications may also be found in duct and piping vibration attenuation. In civil construction, low-frequency bridge vibration issues caused by wind, earthquakes and traffic could be considered. Low-frequency vibration in pipelines (particularly gas pipelines) has also been a widely investigated, long-standing industrial issue. In the automotive and aviation industries, lightweight low-frequency structural noise attenuation systems are paramount.

While the complexity that arises from nonlinearity in vibrating systems has led to a broad tendency to avoid its effects in engineering design in the past, a growing number of nonlinear systems like the one investigated in this work are opening doorways to rich fields of new possibilities. As fundamental research in these areas continues to develop, opportunities to apply that knowledge to harness nonlinear and chaotic behaviour for solving practical issues will continue to grow.

Bibliography

1. Caniato, M., et al., *Acoustic of lightweight timber buildings: A review.* Renewable and Sustainable Energy Reviews, 2017. **80**: p. 585-596.
2. Öqvist, R., F. Ljunggren, and A. Ågren, *Walking sound annoyance vs. impact sound insulation from 20 Hz.* Applied Acoustics, 2018. **73**: p. 904-912.
3. Öqvist, R., *Measurement and Perception of Sound Insulation from 20 Hz between Dwellings*. 2017.
4. Caniato, M., et al., *Impact sound of timber floors in sustainable buildings.* Building and Environment, 2017. **120**: p. 110-122.
5. Ryu, J., et al., *Relation between annoyance and single-number quantities for rating heavy-weight floor impact sound insulation in wooden houses.* The Journal of the Acoustical Society of America, 2011. **129**(5): p. 3047-3055.
6. Sipari, P., *Sound Insulation Of Multi-Storey Houses – A Summary Of Finnish Impact Sound Insulation Results.* Building Acoustics, 2000. **7**(1): p. 15-30.
7. Olynyk, D. and T.D. Northwood, *Assessment of Footstep Noise through Wood-Joist and Concrete Floors.* The Journal of the Acoustical Society of America, 1968. **43**(4): p. 730-733.
8. Gerretsen, E., *A New System for Rating Impact Sound Insulation.* Applied Acoustics, 1976. **9**(4): p. 247-263.
9. Broch, J.T., *Seminar on impact sound insulation test methods: ELAB report STF44 A, 82022*. 1982.
10. Bodlund, K., *Alternative Reference Curves for Evaluation of the Impact Sound Insulation Between Dwellings* Journal of Sound and Vibration, 1985. **102**(3): p. 381-402.
11. Cummer, S.A., J. Christensen, and A. Alù, *Controlling sound with acoustic metamaterials.* Nature Reviews Materials, 2016. **1**.

12. Lu, M.-H., L. Feng, and Y.-F. Chen, *Phononic crystals and acoustic metamaterials.* Materials Today, 2009. **12**(12): p. 34-42.
13. Hussein, M.I., M.J. Leamy, and M. Ruzzene, *Dynamics of Phononic Materials and Structures: Historical Origins, Recent Progress, and Future Outlook.* Applied Mechanics Reviews, 2014. **66**(4): p. 040802-040802.
14. Ma, G. and P. Sheng, *Acoustic metamaterials: From local resonances to broad horizons.* Science Advances, 2016. **2**(2): p. e1501595-e1501595.
15. Fang, X., et al., *Ultra-low and ultra-broad-band nonlinear acoustic metamaterials.* Nature Communications, 2017. **8**(1).
16. Sheng, P., et al., *Vibration properties and optimized design of a nonlinear acoustic metamaterial beam.* Journal of Sound and Vibration, 2020: p. 115739.
17. Georgiadis, F., et al., *Shock isolation through passive energy pumping caused by nonsmooth nonlinearities.* International Journal of Bifurcation and Chaos in Applied Sciences and Engineering, 2005. **15**(6): p. 1989-2001.
18. Lee, Y.S., et al., *Periodic orbits, damped transitions and targeted energy transfers in oscillators with vibro-impact attachments.* Physica D: Nonlinear Phenomena, 2009. **238**(18): p. 1868-1896.
19. Emms, G., et al. *Improving the Impact Insulation of Light Timber Floors*. in *Acoustics*. 2006. Christcurch, New Zealand.
20. Ramage, M.H., et al., *The wood from the trees: The use of timber in construction.* Renewable and Sustainable Energy Reviews, 2017. **68**: p. 333-359.
21. Forssén, J., et al., *Acoustics in wooden buildings State of the art 2008*. 2007.
22. Ljunggren, F., C. Simmons, and K. Hagberg, *Correlation between sound insulation and occupants' perception – Proposal of alternative single number rating of impact sound, par I.* Applied Acoustics, 2014. **85**: p. 57-68.
23. Ljunggren, F., C. Simmons, and R. Öqvist, *Correlation between sound insulation and occupants' perception – Proposal of alternative single number rating of impact sound, part II.* Applied Acoustics, 2017. **123**: p. 143-151.

24. Chui, Y.H., *Vibrational performance of timber floors and the related human discomfort criteria.* Institute of Wood Science, 1986. **10**(5): p. 183-188.

25. Hu, L.J., Y.H. Chui, and D.M. Onysko, *Vibration serviceability of timber floors in residential construction.* Progress in Structural Engineering and Materials, 2001. **3**: p. 228-237.

26. Bard, D., et al., *Human footsteps induced floor vibration.* Journal of the Acoustical Society of America, 2008. **123**(5): p. 3356-3356.

27. Brunskog, J. and P. Hammer, *Prediction model for the impact sound level of lightweight floors.* Acta Acustica - Acustica, 2003. **89**(April 2002): p. 309-322.

28. Weckendorf, J., *Dynamic Response of Structural Timber Flooring Systems*, in *The Centre for Timber Engineering*. 2009, Edinburgh Napier University: Edinburgh, Scotland. p. 235.

29. Brunskog, J., *The Interaction Between the ISO Tapping Machine and Lightweight Floors.* Acta Acustica, 2003. **89**(2): p. 296-308.

30. Cremer, L., M. Heckl, and B.A.T. Petersson, *Structure-Borne Sound*. 3rd ed. 2005, Berlin: Springer.

31. Brunskog, J. and P. Hammer, *Prediction models of impact sound insulation on timber floor structures.* Building acoustics, 2000.

32. Nightingale, T.R.T., et al., *Flanking Transmission in Multi-Family Dwellings: Phase IV*. 2006, National Research Council Canada. p. 426-426.

33. Nightingale, T.R.T. and R.E. Halliwell, *Flanking Transmission at Joints in Multi-Family Dwellings Phase I: Effects of Fire Stops at Floor/Wall Intersection.* Final Report –, 1997.

34. Rindel, J.H., *Sound insulation in buildings.* 1st ed. 2017: CRC Press.

35. Xie, G., D.J. Thompson, and C.J.C. Jones, *The radiation efficiency of baffled plates and strips.* Journal of Sound and Vibration, 2005. **280**(1-2): p. 181-209.

36. Olsson, J. and A. Linderholt. *Low Frequency Force To Sound Pressure Transfer Function Measurements Using a Modified Tapping Machine on a Light Weight*

Wooden Joist Floor. in *World Conference on Timber Engineering*. 2016. Vienna, Austria, Vienna University of Technology.

37. Jeon, J.Y., et al., *Review of the Impact Ball in Evaluating Floor Impact Sound.* Acta Acustica united with Acustica, 2006. **95**(5): p. 777-786.
38. Insternational Standards, O., *ISO 15712-2:2005 Summary*. 2005.
39. International Standards, O., *ISO 12354-2:2017 Summary*. 2017.
40. International Standards, O., *ISO 12354-2:2017 Preview*. 2017.
41. Rasmussen, B., *Sound insulation between dwellings – Requirements in building regulations in Europe.* 2009.
42. Höller, C. and B. Zeitler, *Change in Canada's national building code—Assessing flanking sound transmission in steel-framed constructions.* The Journal of the Acoustical Society of America, 2015. **138**(3): p. 1757-1758.
43. International Code, C., *ICC G2 -2010 Guideline for Acoustics*. 2010.
44. Caniato, M., et al., *Thermal and acoustic performance expectations on timber buildings.* Building Acoustics, 2017. **24**(4): p. 219-237.
45. Liebl, A., M. Späh, and P. Leistner, *Acoustics in wooden buildings-Evaluation of acoustic quality in wooden buildings: Listening tests and questionnaire field study AcuWood Report 3*. 2014: Stuttgart.
46. Park, S.H. and P.J. Lee. *Effects of floor impact noise on people – annoyance and physiological responses*.
47. Simmons, C., K. Hagberg, and E. Backman, *Acoustical performance of apartment buildings - Resident's survey and field measurements Aculite Report 2*. 2011.
48. Hagberg, K.G., *Evaluating Field Measurements of Impact Sound.* Building Acoustics, 2010. **17**(2): p. 105-128.
49. Ljunggren, F., C. Simmons, and K. Hagberg. *Findings from the AkuLite project: Correlation between measured vibro-acoustic parameters and subjective perception in lightweight buildings*. in *Internoise*. 2013. Innsbruck, Austria.
50. Hagberg, K., L. Eng, and P. Leistner, *Acoustics in Wooden Constructions: Acuwood Final Report*. 2013.

51. Ljunggren, F. and A. Ågren, *Potential solutions to improved sound performance of volume based lightweight multi-storey timber buildings.* Applied Acoustics, 2011. **72**: p. 231-240.

52. Rindel, J.H., A. Løvstad, and R. Klæboe. *Aiming at satisfactory sound conditions in dwellings–the use of dose-response curves*. in *Baltic-Nordic Acoustic Meeting*. 2016. Stockholm.

53. Yeoh, D., et al., *State of the Art on Timber-Concrete Composite Structures: Literature Review.* Journal of Structural Engineering, 2011. **137**(10): p. 1085-1095.

54. Martins, C., et al., *Acoustic performance of timber and timber-concrete floors.* Construction and Building Materials, 2015. **101**: p. 684-691.

55. Bolmsvik, Å. and A. Brandt, *Damping assessment of light wooden assembly with and without damping material.* Engineering Structures, 2013. **49**: p. 434-447.

56. Ljunggren, F. and A. Ågren, *Elastic Layers to Reduce Sound Transmission in Lightweight Buildings.* Building Acoustics, 2013. **20**(1): p. 25-42.

57. Schiavi, A., C. Guglielmone, and P. Miglietta, *Effect and importance of static-load on airflow resistivity determination and its consequences on dynamic stiffness.* Applied Acoustics, 2011. **72**: p. 705-710.

58. Harris, C.M. and A.G. Piersol, *Applied Damping Treatments*, in *Harris' Shock and Vibration Handbook*. 2002, McGraw-Hill.

59. Flodén, O., et al., *The effect of modelling acoustic media in cavities of lightweight buildings on the transmission of structural vibrations.* Engineering Structures, 2015. **83**: p. 7-16.

60. Medveď, J., B. Ingeleare, and L. de Geetere, *Impact Sound Insulation Concept for Lightweight Timber Floor.* Advanced Materials Research, 2013. **855**(2014): p. 245-251.

61. Bein, T., S. Herold, and D. Mayer. *Recent advances in active noise and vibration control*. in *Euronoise*. 2015. Maastricht, Netherlands.

62. Hansen, C.H., *Active control of noise and vibration*. Vol. 1. 2013: CRC Press Taylor and Francis Group.

63. Kraus, R., et al., *Development of Active Engine Mounts Based on Piezo Actuators.* ATZ worldwide, 2014. **116**(1): p. 46-51.

64. Fisco, N.R. and H. Adeli, *Smart structures: Part I—Active and semi-active control.* Scientia Iranica, 2011. **18**(3): p. 275-284.

65. Schiavi, A., et al., *Acoustical Performance Characterization of Resilient Materials Used under Floating Floors in Dwellings.* Acta Acustica united with Acustica, 2007. **93**: p. 477-485.

66. Schiavi, A., *Improvement of impact sound insulation: A constitutive model for floating floors.* Applied Acoustics, 2018. **129**: p. 64-71.

67. Schiavi, A., et al., *The effect of damping in Resilient materials used in floating floors on impact sound insulation*, in *22nd International Congress on Sound and Vibration, ICSV 2015*. 2015: Florence, Italy. p. 8.

68. Warnock, A.C.C., *Impact Sound Measurements on Floors Covered with Small Patches of Resilient Materials or Floating Assemblies*. 2000, Institute for Research in Construction.

69. Kuhl, W. and H. Kaiser, *Absorption of structure-borne sound in building materials without and with sand-filled cavities.* Acta Acustica united with Acustica, 1952. **2**(4): p. 179-188.

70. Emms, G.W. *Measurements on Timber-Framed Floors with a Granular Material in the Floor Topping*. in *Proceedings of 20th International Congress on Acoustics*. 2010. Sydney.

71. Chung, H., et al., *Lightweight Floor/Ceiling Systems with Improved Impact Sound Insulation.* Building Acoustics, 2010. **17**(2): p. 129-141.

72. Caniato, M., et al., *Time-depending performance of resilient layers under floating floors.* Construction and Building Materials, 2016. **102**: p. 226-232.

73. Ding, Y.W., et al., *Research on Impact Sound Insulation Performance of Timber Floor Structure.* Experimental Techniques, 2021.

74. Lu, Z., et al., *Nonlinear dissipative devices in structural vibration control: A review.* Journal of Sound and Vibration, 2018. **423**: p. 18-49.

75. Homb, A., C. Guigou-Carter, and A. Rabold, *Impact sound insulation of cross-laminated timber/ massive wood floor constructions: Collection of laboratory measurements and result evaluation.* Building Acoustics, 2017. **24**(1): p. 35-52.

76. Homb, A., *Low frequency sound and vibrations from impacts on timber floor constructions*. 2005.

77. Sheng, P., et al., *Locally resonant sonic materials.* Physica B, 2003. **338**: p. 201-205.

78. Fang, N., et al., *Ultrasonic metamaterials with negative modulus.* Nature Letters, 2006. **5**: p. 452-456.

79. Sheng, P. and C.T. Chan, *Classical wave localization and spectral gap materials.* Zeitschrift für Kristallographie-Crystalline Materials, 2005. **220**(9-10): p. 757-764.

80. Goffaux, C. and J. Sánchez-Dehesa, *Two-dimensional phononic crystals studied using a variational method: Application to lattices of locally resonant materials.* Physical Review B, 2003. **67**(144301).

81. Sheng, P., et al., *Dynamic mass density and acoustic metamaterials.* Physica B, 2007. **394**: p. 256-261.

82. Liu, Z., et al., *Locally Resonant Sonic Materials.* Science, 2000. **289**(5485): p. 1734-1736.

83. Goffaux, C., et al., *Evidence of Fano-Like Interference Phenomena in Locally Resonant Materials.* Physical review letters, 2002. **88**(22).

84. Liu, Z., C.T. Chan, and P. Sheng, *Analytic model of phononic crystals with local resonances.* Physical Review B, 2005. **71**: p. 014013-014013.

85. Yao, S., X. Zhou, and G. Hu, *Experimental study on negative effective mass in a 1D mass-spring system.* New Journal of Physics, 2008. **10**: p. 43020-43020.

86. Milton, G.W. and J.R. Willis, *On modifications of Newton's second law and linear continuum elastodynamics.* Proceedings of the Royal Society A, 2007. **463**: p. 855-880.

87. Oudich, M., et al., *A sonic band gap based on the locally resonant phononic plates with stubs.* New J. Phys., 2010. **12**(083049).

88. Peng, H. and P.F. Pai, *Acoustic metamaterial plates for elastic wave absorption and structural vibration suppression.* International Journal of Mechanical Sciences, 2014. **89**: p. 350-361.

89. Huang, T.-Y., C. Shen, and Y. Jing, *Membrane- and plate-type acoustic metamaterials.* The Journal of the Acoustical Society of America, 2016. **139**(6): p. 3240-3250.

90. Yang, Z., et al., *Membrane-Type Acoustic Metamaterial with Negative Dynamic Mass.* Physical Review Letters, 2008. **101**: p. 204301-204301.

91. Pronk, A., R. Maffei, and H. Martin, *Research on the combination of water and membranes as a structural building material.* Proceedings of the International Association for Shell and Spatial Structures (IASS) Symposium 2009, 2009(October): p. 3024-3033.

92. Yang, M., et al., *Subwavelength total acoustic absorption with degenerate resonators.* Appl. Phys. Lett, 2015. **1071**(10).

93. Yang, Z.M., et al., *Acousticmetamaterial panels for sound attenuation in the 50–1000 Hz regime.* Applied Physics Letters, 2010. **96**.

94. Tang, Y., et al., *Hybrid acoustic metamaterial as super absorber for broadband low-frequency sound.* Nature Publishing Group, 2017.

95. Ming Ho, K., et al., *Broadband locally resonant sonic shields.* Citation: Appl. Phys. Lett, 2003. **83**: p. 5566-5566.

96. Xiao, Y. and J. Wen, *Longitudinal wave band gaps in metamaterial-based elastic rods containing multi-degree-of-freedom resonators.* New Journal of Physics, 2012. **14**: p. 033042-033042.

97. Sugino, C., M. Ruzzene, and A. Erturk, *Merging mechanical and electromechanical bandgaps in locally resonant metamaterials and metastructures.* Journal of the Mechanics and Physics of Solids, 2018. **116**: p. 323-333.

98. Hyeon Lee, S., et al., *Acoustic metamaterial with negative modulus.* Journal of Physics: Condensed Matter, 2009. **21**: p. 175704-175704.

99. Huang, H.H. and C.T. Sun, *Theoretical investigation of the behavior of an acoustic metamaterial with extreme Young's modulus.* Journal of the Mechanics and Physics of Solids, 2011. **59**: p. 2070-2081.

100. Sugino, C., et al., *An investigation of electroelastic bandgap formation in locally resonant piezoelectric metastructures.* Smart Materials and Structures, 2017. **26**: p. 055029-055029.

101. Sugino, C., et al., *A general theory for bandgap estimation in locally resonant metastructures.* Journal of Sound and Vibration, 2017. **406**: p. 104-123.

102. Wang, G., J. Wen, and Y. Liu, *Two-Dimensional Locally Resonant Phononic Crystals with Binary Structures.* Article in Physical Review Letters, 2004.

103. Banerjee, A., R. Das, and E.P. Calius, *A new approach for determination of the attenuation bandwidth of a resonating metamaterial.* Applied Mechanics and Materials, 2016. **846**: p. 264-269.

104. Lee, S.H. and O.B. Wright, *Origin of negative density and modulus in acoustic metamaterials.* Physical Review B, 2016. **93**: p. 024302-024302.

105. Pai, P.F., H. Peng, and S. Jiang, *Acoustic metamaterial beams based on multi-frequency vibration absorbers.* International Journal of Mechanical Sciences, 2014. **79**: p. 195-205.

106. Sugino, C., et al., *On the mechanism of bandgap formation in locally resonant finite elastic metamaterials.* Journal of Applied Physics, 2016. **120**(13).

107. Huang, H.H. and C.T. Sun, *Wave attenuation mechanism in an acoustic metamaterial with negative effective mass density.* New Journal of Physics, 2009. **11**(013003): p. 15.

108. Zhu, R., et al., *A chiral elastic metamaterial beam for broadband vibration suppression.* Journal of Sound and Vibration, 2014. **333**: p. 2759-2773.

109. Yilmaz, C., G.M. Hulbert, and N. Kikuchi, *Phononic band gaps induced by inertial amplification in periodic media.* Physical Review B, 2007. **76**.

110. Yilmaz, C. and G.M. Hulbert, *Theory of phononic gaps induced by inertial amplification in finite structures.* Physics Letters A, 2010. **374**: p. 3576-3584.

111. Taniker, S. and C. Yilmaz, *Design, analysis and experimental investigation of three-dimensional structures with inertial amplification induced vibration stop bands.* International Journal of Solids and Structures, 2015. **72**: p. 88-97.

112. Yuksel, O. and C. Yilmaz, *Shape optimization of phononic band gap structures incorporating inertial amplification mechanisms.* Journal of Sound and Vibration, 2015. **355**: p. 232-245.

113. Taniker, S. and C. Yilmaz, *Generating ultra wide vibration stop bands by a novel inertial amplification mechanism topology with flexure hinges.* International Journal of Solids and Structures, 2016. **106107**: p. 129-138.

114. Frandsen, N.M.M., et al., *Inertial amplification of continuous structures: Large band gaps from small masses.* Journal of Applied Physics, 2016. **119**(12): p. 124902.

115. Li, J. and S. Li, *Generating ultra wide low-frequency gap for transverse wave isolation via inertial amplification effects.* Physics Letters A, 2017. **1**: p. 7-13.

116. Schmied, J.U., et al. *Toward structurally-integrated locally resonant metamaterials for vibration attenuation*. in *Active and Passive Smart Structures and Integrated Systems*. 2017. SPIE.

117. Xiao, Y., et al., *Theoretical and Experimental Study of Locally Resonant and Bragg Band Gaps in Flexural Beams Carrying Periodic Arrays of Beam-Like Resonators.* Journal of Vibration and Acoustics, 2013. **135**(4): p. 041006-041006.

118. Xiao, Y., J. Wen, and X. Wen, *Flexural wave band gaps in locally resonant thin plates with periodically attached spring--mass resonators.* J. Phys. D: Appl. Phys. J. Phys. D: Appl. Phys, 2012. **45**(45): p. 195401-12.

119. Krödel, S., et al., *3D Auxetic Microlattices with Independently Controllable Acoustic Band Gaps and Quasi-Static Elastic Moduli.* Advanced Engineering Materials, 2013. **15**(9999).

120. Al Ba'ba'a, H., et al., *Dispersion transitions and pole-zero characteristics of finite inertially amplified acoustic metamaterials.* Journal of Applied Physics, 2018. **123**: p. 105106-105106.

121. Mitchell, S.J., *Metaconcrete : engineered aggregates for enhanced dynamic performance*. 2016.

122. Kettenbeil, C. and G. Ravichandran, *Experimental investigation of the dynamic behavior of metaconcrete.* International Journal of Impact Engineering, 2018. **111**: p. 199-207.

123. Zhong, R., et al., *Metamaterial I-Girder for Vibration Absorption of Composite Cable-Stayed Bridge.* Journal of Engineering Mechanics, 2018. **144**(7).

124. Gendelman, O., et al., *Energy Pumping in Nonlinear Mechanical Oscillators: Part I—Dynamics of the Underlying Hamiltonian Systems.* Journal of Applied Mechanics, 2001. **68**: p. 34.

125. Vakakis, A.F., et al., *Dynamics of linear discrete systems connected to local, essentially non-linear attachments.* Journal of Sound and Vibration, 2003. **264**(3): p. 559-577.

126. Brooke, D.C., et al., *Acoustic metamaterial for low frequency sound absorption in linear and nonlinear regimes.* Journal of Sound and Vibration, 2020. **485**: p. 115585.

127. Zhou, J., et al., *A nonlinear resonator with inertial amplification for very low-frequency flexural wave attenuations in beams.* Nonlinear Dynamics, 2019. **96**(1): p. 647-665.

128. Fang, X., et al., *Ultrabroad acoustical limiting in nonlinear metamaterials due to adaptive-broadening band-gap effect.* Physical Review B, 2020. **101**(1): p. 104304.

129. Rajasekar, S. and M.A.F. Sanjuan, *Nonlinear resonances*. Springer Series in Synergetics 2016, Switzerland: Springer.

130. Wierschem, N.E., et al., *Response attenuation in a large-scale structure subjected to blast excitation utilizing a system of essentially nonlinear vibration absorbers.* Journal of Sound and Vibration, 2017. **389**: p. 52-72.

131. Banerjee, A., E.P. Calius, and R. Das, *Impact based wideband nonlinear resonating metamaterial chain.* International Journal of Non-Linear Mechanics, 2018. **103**: p. 138-144.

132. Gendelman, O.V. and A. Alloni, *Dynamics of forced system with vibro-impact energy sink.* Journal of Sound and Vibration, 2015. **358**: p. 301-314.

133. Das, S., et al., *Reliability-based optimization of nonlinear energy sink with negative stiffness and sliding friction.* Journal of Sound and Vibration, 2020. **485**: p. 115560.

134. Lee, Y.S., et al., *Passive non-linear targeted energy transfer and its applications to vibration absorption: A review.* Journal of Multi-body Dynamics, 2008. **222**(2): p. 77-134.

135. Farshi, B. and A. Assadi, *Development of a chaotic nonlinear tuned mass damper for optimal vibration response.* Communications in Nonlinear Science and Numerical Simulation, 2011. **16**(11): p. 4514-4523.

136. Laalej, H., et al., *MR damper based implementation of nonlinear damping for a pitch plane suspension system.* Smart Materials and Structures, 2012. **21**(4).

137. Hoang, N. and Y. Fujino, *Multi-mode control performance of nonlinear dampers in stay cable vibrations.* Structural Control and Health Monitoring, 2009. **16**: p. 860-868.

138. Ding, H. and L.Q. Chen, *Designs, analysis, and applications of nonlinear energy sinks.* Nonlinear Dynamics, 2020. **100**(4): p. 3061-3107.

139. Vakakis, A.F., et al., *Nonlinear targeted energy transfer in mechanical and structural systems I.* Solid Mechanics and its Applications. Vol. 156. 2008: Springer Science & Business Media.

140. Vakakis, A.F., *Inducing passive nonlinear energy sinks in vibrating systems.* Journal of Vibration and Acoustics, Transactions of the ASME, 2001. **123**(3): p. 324-332.

141. Gourdon, E., et al., *Nonlinear energy pumping under transient forcing with strongly nonlinear coupling: Theoretical and experimental results.* Journal of Sound and Vibration, 2007. **300**(3-5): p. 522-551.

142. Starosvetsky, Y. and O.V. Gendelman, *Vibration absorption in systems with a nonlinear energy sink: Nonlinear damping.* Journal of Sound and Vibration, 2009. **324**(3-5): p. 916-939.

143. Georgiades, F. and A.F. Vakakis, *Dynamics of a linear beam with an attached local nonlinear energy sink.* Communications in Nonlinear Science and Numerical Simulation, 2007. **12**(5): p. 643-651.

144. Nucera, F., et al., *Targeted energy transfers in vibro-impact oscillators for seismic mitigation.* Nonlinear Dynamics, 2007. **50**(3): p. 651-677.

145. Li, T., et al., *Chaotic characteristic of a linear oscillator coupled with vibro-impact nonlinear energy sink.* Nonlinear Dyn, 2018. **91**: p. 2319-2330.

146. Narisetti, R.K., M. Leamy, and M. Ruzzene, *A Perturbation Approach for Predicting Wave Propagation in One-Dimensional Nonlinear Periodic Structures.pdf>.* Journal of Vibration and Acoustics 2010. **132**(3).

147. Fang, X., et al., *Wave propagation in one-dimensional nonlinear acoustic metamaterials.* New J. Phys, 2017. **19**: p. 53007-53007.

148. Banerjee, A., R. Das, and E.P. Calius, *Waves in Structured Mediums or Metamaterials: A Review.* Archives of Computational Methods in Engineering, 2019. **26**(4): p. 1029-1058.

149. Vakakis, A.F., M.E. King, and A.J. Pearlstein, *Forced localization in a periodic chain of non-linear oscillators.* International Journal of Non-Linear Mechanics, 1994. **29**: p. 429-447.

150. Khajehtourian, R. and M.I. Hussein, *Dispersion characteristics of a nonlinear elastic metamaterial.* AIP Advances, 2014. **4**(12).

151. Fang, X., et al., *Bridging-coupling band gaps in nonlinear acoustic metamaterials.* Physical Review Applied, 2018. **10**(5): p. 054049.
152. Blazier, W.E., R.B. Dupree, and B. Warren, *Investigation of low-frequency footfall noise in wood-frame, multifamily building construction.* The Journal of the Acoustical Society of America, 1994. **96**(108): p. 1521-1433.
153. Hammer, P. and J. Brunskog, *Vibration Isolation on Lightweight Floor Structures.* Building Acoustics, 2002. **9**(4): p. 257-269.
154. Ryu, J., H. Song, and Y. Kim, *Effect of the suspended ceiling with low-frequency resonant panel absorber on heavyweight floor impact sound in the building.* Building and Environment, 2018. **139**: p. 1-7.
155. Bolmsvik, Å., *Structural-Acoustic Vibrations in Wooden Assemblies: Experimental Modal Analysis and finite element modelling*, in *School of Engineering*. 2013, Linnaeus University: Växjö, Sweden.
156. Cho, T., *Experimental and numerical analysis of floating floor resonance and its effect on impact sound transmission.* Journal of Sound and Vibration, 2013. **332**(25): p. 6552-6561.
157. Cho, T., *Vibro-acoustic characteristics of floating floor system: The influence of frequency-matched resonance on low frequency impact sound.* Journal of Sound and Vibration, 2013. **332**(1): p. 33-42.
158. Kim, K.-W., et al., *Correlation between dynamic stiffness of resilient materials and heavyweight impact sound reduction level.* Building and Environment, 2009. **44**: p. 1589-1600.
159. Alessandro, L.D., E. Belloni, and G.D. Al. *Modelling and experimental verification of a single phase three-dimensional lightweight locally resonant elastic metamaterial with complete low frequency bandgap*. in *11th International Congress on Engineered Material Platforms for Novel Wave Phenomena - Metamaterials*. 2017. Marseille, France.

160. Claeys, C.C., et al., *On the potential of tuned resonators to obtain low-frequency vibrational stop bands in periodic panels.* Journal of Sound and Vibration, 2013. **332**: p. 1418-1436.

161. Xiao, Y., J. Wen, and X. Wen, *Sound transmission loss of metamaterial-based thin plates with multiple subwavelength arrays of attached resonators.* Journal of Sound and Vibration, 2012. **331**: p. 5408-5423.

162. Nouh, M., O. Aldraihem, and A. Baz, *Wave propagation in metamaterial plates with periodic local resonances.* Journal of Sound and Vibration, 2015. **341**: p. 53-73.

163. Sharma, B. and C.T. Sun, *Impact load mitigation in sandwich beams using local resonators.* Journal of Sandwich Structures and Materials, 2015. **18**(1): p. 50-64.

164. Van Belle, L., et al., *On the impact of damping on the dispersion curves of a locally resonant metamaterial: Modelling and experimental validation.* Journal of Sound and Vibration, 2017. **409**: p. 1-23.

165. Sun, H., X. Du, and P.F. Pai, *Theory of metamaterial beams for broadband vibration absorption.* Journal of Intelligent Material Systems and Structures, 2010. **21**(11): p. 1085-1101.

166. Qureshi, A., B. Li, and K.T. Tan, *Numerical investigation of band gaps in 3D printed cantilever-in- mass metamaterials.* Nature: Scientific Reports, 2016. **6**: p. 28314-28314.

167. Sun, C.T., J.S. Chen, and W. Lafayette, *Dynamic Behaviour of a Sandwich Beam with Internal Resonators.* Journal of Sandwich Structures & Materials, 2011. **13**(4): p. 391-408.

168. Van Belle, L., et al., *The impact of damping on the sound transmission loss of locally resonant metamaterial plates.* Journal of Sound and Vibration, 2019. **461**: p. 114909.

169. Wu, L., Q. Geng, and Y.-m. Li, *A locally resonant elastic metamaterial based on coupled vibration of internal liquid and coating layer.* Journal of Sound and Vibration, 2020. **468**: p. 115102.

170. Wang, X., *Dynamic behaviour of a metamaterial system with negative mass and modulus.* International Journal of Solids and Structures, 2014. **51**: p. 1534-1541.

171. Brun, M., A. Movchan, and I.S. Jones, *Phononic Band Gap Systems in Structural Mechanics: Finite Slender Elastic Structures and Infinite Periodic Waveguides.* Journal of Vibration and Acoustics, 2013. **135**: p. 041013.

172. Wang, T., et al., *Acoustic characteristics of damped metamaterial plate with parallel attached resonators.* Archives of Mechanics, 2017. **69**: p. 29-52.

173. Sharma, B. and C.T. Sun, *Impact load mitigation in sandwich beams using local resonators.* Journal of Sandwich Structures and Materials, 2015. **18**: p. 50-64.

174. Gao, P., et al., *Single-phase metamaterial plates for broadband vibration suppression at low frequencies.* Journal of Sound and Vibration, 2019. **444**: p. 108-126.

175. Oliveira, M.F. and J.V. Patricio, *Impact Noise of Non-homogeneous Floors: Analysis of Different Input Parameters for Computational Modeling Predictions.* Journal of Civil Engineering and Architecture, 2017. **11**(3): p. 274-281.

176. Manimala, J.M. and C.T. Sun, *Microstructural design studies for locally dissipative acoustic metamaterials.* Journal of Applied Physics Applied Physics Letters, 2014. **115**(101).

177. Wang, T., M.-P. Sheng, and Q.-H. Qin, *Multi-flexural band gaps in an Euler–Bernoulli beam with lateral local resonators.* Physics Letters A, 2016. **380**: p. 525-529.

178. Chen, Y.Y., et al., *Dissipative elastic metamaterials for broadband wave mitigation at subwavelength scale.* Composite Structures, 2016. **136**: p. 358-371.

179. Banerjee, A. and R. Das, *Nonlinear mechanical metamaterial experimental study*, in *Phononics*. 2017: Changsha.

180. Vakakis, A.F., M.E. King, and A.J. Pearlstein, *Forced localization in a periodic chain of non-linear oscillators.* International Journal of Non-Linear Mechanics, 1994. **29**(3): p. 429-447.

181. Khajehtourian, R., *Nonlinear Dispersive Elastic Waves in Solids: Exact, Approximate, and Numerical Solutions.* 2017.

182. Stronge, W.J., *Impact mechanics*. 2000: Cambridge University Press.

183. Han, S.M., H. Benaroya, and T. Wei, *Dynamics of transversely vibrating beams using four engineering theories.* Journal of Sound and Vibration, 1999. **225**(5): p. 935-988.

184. Bhattacharjee, A., *New Approximations in Vibroimpact Problems*, in *Department of Mechanical Engineering* 2019, Indian Institute of Technology Kanpur: Kanpur. p. 130.

185. Thompson, D., *Railway noise and vibration: mechanisms, modelling and means of control*. 2009, Oxford, U.K.: Elsevier.

186. Rao, S.S., *Vibration of continuous systems*. 2007, Hoboken, New Jersey, U.S.A.: John Wiley & Sons.

187. Wilson, E.L., *Three-dimensional static and dynamic analysis of structures*. 3rd ed. 2002, Berkeley, California: Computers and Structure, Inc.

188. Walker, S.J.I., G.S. Aglietti, and P. Cunningham, *A study of joint damping in metal plates.* Acta Astronautica, 2009. **65**(1): p. 184-191.

189. Christoforou, A.p. and A.S. Yigit, *Effect of Flexibility on Low Velocity Impact Response* Journal of Sound and Vibration, 1998. **217**(3): p. 563-578.

190. Ivanov, A.P., *On multiple impact.* Journal of Applied Mathematics and Mechanics, 1996. **59**(6): p. 887-902.

191. Liu, C., Z. Zhao, and B. Brogliato, *Frictionless multiple impacts in multibody systems. I. theoretical framework.* Proceedings of the Royal Society of London A: Mathematical, Physical and Engineering Sciences, 2008. **464**(2100): p. 3193–3211.

192. Wang, H., et al., *Experimental and theoretical analysis of the elastic-plastic normal repeated impacts of a sphere on a beam.* International Journal of Solids and Structures, 2017. **109**: p. 131-142.

193. Bishop, S., M. Thompson, and S. Foale, *Prediction of period-1 impacts in a driven beam.* Proceedings of the Royal Society of London. Series A: Mathematical, Physical and Engineering Sciences, 1996. **452**(1954): p. 2579-2592.

194. Vyasarayani, P.C., J. McPhee, and S. Birkett, *Modeling Impacts Between a Continuous System and a Rigid Obstacle Using Coefficient of Restitution.* Journal of Applied Mechanics, 2010. **77**(021008).

195. Wagg, D.J., *A note on coefficient of restitution models including the effects of impact induced vibration.* Journal of Sound and Vibration, 2007. **300**(3-5): p. 1071-1078.

196. Melcher, J., A. Champneys, and D. Wagg, *The impacting cantilever: modal non-convergence and the importance of stiffness matching.* Philosophical Transactions of the Royal Society A, 2013. **371**(20120434).

197. Popov, V.L., *Contact mechanics and friction: Physical Principles and Applications*. 2017: Springer.

198. Huang, K.-C. and C.-C. Ma, *Investigating dynamic transient behavior of Timoshenko cantilever beam by theoretical analysis, numerical calculation and experimental measurement.* International Journal of Solids and Structures, 2016. **80**: p. 274-283.

199. Neild, S.A., P.D. McFadden, and M.S. Williams, *A review of time-frequency methods for structural vibration analysis.* Engineering Structures, 2003. **25**(6): p. 713-728.

200. Boškoski, P., et al., *PyMODAlib: v0.4.0b1.* 2020.

201. Sangiuliano, L., et al., *Reducing vehicle interior nvh by means of locally resonant metamaterial patches on rear shock towers*. 2019, SAE Technical Paper.

202. Nateghi, A., et al., *Design and experimental validation of a metamaterial solution for improved noise and vibration behavior of pipes.* JOURNAL OF SOUND AND VIBRATION, 2019. **96-117**: p. 96-117.

203. Jagodzinski, D.J., et al., *Modeling and optimizing an acoustic metamaterial to minimize low-frequency structure-borne sound.* Mechanics Based Design of Structures and Machines, 2020: p. 1-15.

204. Caetano, E., Á. Cunha, and C. Moutinho, *Vandal Loads and Induced Vibrations on a Footbridge.* Journal of Bridge Engineering, 2011. **16**(3): p. 375-382.

205. Klaerner, M., et al., *FEA-based methods for optimising structure-borne sound radiation.* Mechanical Systems and Signal Processing, 2017. **89**: p. 37-47.

206. Conta, S. and A. Homb. *Challenges and limitations using the Integral Transform Method to obtain the impact noise level of timber floors*. in *Euronoise 2018*. 2018. Crete, Greece.

207. Fritze, D., S. Marburg, and H.J. Hardtke, *Estimation of Radiated Sound Power: A Case Study on Common Approximation Methods.* Acta Acustica united with Acustica, 2009. **95**(5): p. 833-842.

208. Putra, A., et al. *Estimation of Radiated Sound Power: A Case Study on Common Approximation Methods*

in *INTERNOISE 2014 - 43rd International Congress on Noise Control Engineering*. 2014. Melbourne, Australia.

Appendix 1. Code segments

The following code is selected to show segments that are critical for the simulation of the system. Each section relates to a logical step in the overall sequence followed for each time step. The sequence begins by calculating the relative positions of points on the resonators and the elastic structure that are interacting via either contact or magnetic forces. Then, the forces are calculated based on those positions and added to the relevant dofs in the force vectors. Finally, the displacements, velocities and accelerations are calculated via separate time-stepping algorithms for the elastic structure and the resonators. The whole codebase comprises approximately 3200 lines of code.

A 1.1. Impact point positions

```
# Calculate positions of impact points and distance between resonator
and fixed magnet surfaces

    # Reference variables relating impact point positions to array
indices
    upper_left          = 0
    upper               = 0
    lower_left          = 1
    lower               = 1
    upper_right         = 2
    lower_right         = 3

    # For each strut
    for i in range(num_struts):
        # Calculate horizontal position of each resonator impact point
(4 per resonator)
        # um            = horizontal displacement of resonator cog
        # resonator_dr  = the length of the vector from resonator cog
to an impact point
        # theta         = the angle of the resonator from vertical from
resonator cog to top right impact point
        # theta_orthog  = the angle of the vector

        resonator_impact_point[i, upper_left]  = um[i] - resonator_dr *
sin(theta[i] + theta_orthog)
        resonator_impact_point[i, lower_left]  = um[i] + resonator_dr *
sin(theta[i] - theta_orthog)
        resonator_impact_point[i, upper_right] = um[i] - resonator_dr *
sin(theta[i] - theta_orthog)
        resonator_impact_point[i, lower_right] = um[i] + resonator_dr *
sin(theta[i] + theta_orthog)

        # Calculate the height of upper and lower surfaces of each
resonator
```

```
        resonator_surface[i, upper]             = wm[i] + resonator_h +
resonator_t/2
        resonator_surface[i, lower]             = wm[i] + resonator_h -
resonator_t/2

        # Calculate the horizontal position of each strut impact point
(4 per strut)
        strut_impact_point[i, upper_left]      = us2[i] - strut_r
        strut_impact_point[i, lower_left]      = us1[i] - strut_r
        strut_impact_point[i, upper_right]     = us2[i] + strut_r
        strut_impact_point[i, lower_right]     = us1[i] + strut_r
```

A 1.2. Magnet separation distances

```
        # Calculate the heights of the lower surface of the upper magnet
and upper surface of the lower magnet
        strut_magnet_surface[i, upper]          = wm2[i] + magnet2_h -
upper_fixed_magnet_t/2
        strut_magnet_surface[i, lower]          = wm1[i] + magnet1_h +
lower_fixed_magnet_t/2

        # Calculate the distance between facing surfaces of each fixed
magnet to resonator
        magnet_separation[i, upper]            = strut_magnet_surface[i,
upper] - resonator_surface[i, upper]
        magnet_separation[i, lower]               = resonator_surface[i,
lower] - strut_magnet_surface[i, lower]
```

A 1.3. Repulsive magnetic forces

```
# Calculate the current repulsive magnetic forces for each spring
assembly

    # For each strut
    for i in range(num_struts):
        # Reset net contact force variable since later, it is added to
rather than assigned a value directly
        net_cntct_frc_strut[i, 1]    = 0

        # If the simulation is using the experimentally derived force
displacement curve described in Chapter 3
        if beam_config['mag_frc_curve'] == 'experimental':
            magnet1_force[i] = mag_frc_multiplier * ramp_variable*(-(-
0.1483557 + (94.5189957)/(1 + (1000*magnet_separation[i,
lower]/202116600)**0.5518322)**36496.28)) # spring force applied to
lower fixed magnet
            magnet2_force[i] = mag_frc_multiplier * ramp_variable*(-
0.1483557 + (94.5189957)/(1 + (1000*magnet_separation[i,
upper]/202116600)**0.5518322)**36496.28) # spring force applied to upper
fixed magnet

        # If the simulation is using the cubic force displacement curve
describe in Chapter 5
        elif beam_config['mag_frc_curve'] == 'cubic':
```

```
            low_frc_decay_rate = 10 # higher number = faster force decay
at low end of force displacement curve
            prestress = 100 # magnitude of repulsive force between
resonator and fixed magnets when relative displacement is zero
            res_relative_displacement[i] = wm[i] - (wm1[i]+wm2[i])/2

            if res_relative_displacement[i] > 0:
                magnet1_force[i] = ramp_variable * (-prestress *
np.exp(-low_frc_decay_rate * res_relative_displacement[i]))
                magnet2_force[i] = ramp_variable * (k_spr_linear *
res_relative_displacement[i] + k_spr_nonlinear *
res_relative_displacement[i]**3 + prestress)
            else:
                magnet1_force[i] = ramp_variable * (k_spr_linear *
res_relative_displacement[i] + k_spr_nonlinear *
res_relative_displacement[i]**3 - prestress)
                magnet2_force[i] = ramp_variable * (prestress *
np.exp(low_frc_decay_rate * res_relative_displacement[i]))
```

A 1.4. Magnetic torque applied to resonator

```
# Calculate the current magnetic torque on each resonator
        net_sprng_frc_res[i, 1] = -magnet1_force[i] + -
magnet2_force[i] - F_frctn1_strut[i] - F_frctn2_strut[i] # rename to
spring force
        # If resonators are free to rotate
        if beam_config['fixed_res_rotation'] == False:
            # Calculate the magnetic torque on each resonator
            mag_trq_res[i] =
(mag_trq_multiplier*(abs(magnet1_force[i]) + abs(magnet2_force[i])) *
resonator_t * sin(theta[i]))
```

A 1.5. Impact point forces

```
# Calculate  forces for each strut-resonator impact point pair

            # For each left hand side impact point
            for j in range(2): # left hand side impact points
                # Calculate the overlap between the strut and the
resonator
                overlap[i, j] = resonator_impact_point[i, j] -
strut_impact_point[i, j]
                # If there is an overlap
                if overlap[i, j] >= 0:
                    # Calculate the contact force at that point
                    # (captures the sign of 'overlap' but avoids raising
a negative value to a non-integer power)
                    impct_pt_frc_strut[i, j] = hertzian_stiffness *
abs(overlap[i, j])**(3/2)
                    # Add it to the net force for that strut
                    net_cntct_frc_strut[i, 1] += impct_pt_frc_strut[i,
j]
                # If there is no overlap,
                else:
```

```
                    # set it to zero
                    overlap[i, j]               = 0
                    # Record contact separation unless simulation is
currently ramping internal forces for prestressing
                    if beam_config['ramp'] == False:
                        cntct_separation[i, j]      = True
                    # Set strut contact force for that point to zero
                    impct_pt_frc_strut[i, j]    = 0

            # For each right hand side impact point
            for j in range(2,4):    # right hand side impact points
                # Calculate the overlap between the strut and the
resonator
                overlap[i, j] = resonator_impact_point[i, j] -
strut_impact_point[i, j]
                # Catch instability for troubleshooting
                if mat.isnan(overlap[i, j]) == True:
                    trace()
                # If there is an overlap
                if overlap[i, j] <= 0:
                    # Calculate the contact force at that point
                    # (captures the sign of 'overlap' but avoids raising
a negative value to a non-integer power)
                    impct_pt_frc_strut[i, j]   = -1 * hertzian_stiffness
* abs(overlap[i, j])**(3/2)
                    # Add it to the net force for that strut
                    net_cntct_frc_strut[i, 1]                       +=
impct_pt_frc_strut[i, j]     # total impact force applied to strut
                    # Catch instability for troubleshooting
                    if np.isnan(impct_pt_frc_strut[i, j]) == True or
np.isinf(impct_pt_frc_strut[i, j]) == True:
                        trace()
                # If there is no overlap,
                else:
                    # set it to zero
                    overlap[i, j]               = 0
                    # Record contact separation unless simulation is
currently ramping internal forces for prestressing
                    if beam_config['ramp'] == False:
                        cntct_separation[i, j]      = True
                    # Set strut contact force for that point to zero
                    impct_pt_frc_strut[i, j]    = 0
```

A 1.6. Torque due to contact forces

```
# Calculate total impact_torque and add to resonator torque

            # first reset variable since it is added to later rather
than assigned a value directly
            impact_torque[i]      = 0
            for j in range(2):
                impact_torque[i]    += impct_pt_frc_strut[i, 2*j] *
resonator_t/2 - impct_pt_frc_strut[i, 2*j+1] * resonator_t/2

            # Calculate the total torque applied to resonator
            net_trq_res[i, 1]                     = mag_trq_res[i] +
impact_torque[i]
```

A 1.7. Add contact forces to force vector for elastic structure

```
# Add precalculated contact forces to appropriate force vector dofs

    # For each strut
    for i in range(num_struts):
        # For upper contact points, then lower contact points
        for j in range(2):
            # If contact exists at either upper left or right mpact
points
            if impct_pt_frc_strut[i, 2*j] != 0:
                # Store the contact force in the relevant horizontal
force vector dof
                F[impact2_hdof[i], 1] = impct_pt_frc_strut[i, 2*j]
            # If contact exists at eith lower left or right impact points
            if impct_pt_frc_strut[i, 2*j+1] != 0:
                # Store the contact force in the relevant horizontal
force vector dof
                F[impact1_hdof[i], 1] = impct_pt_frc_strut[i, 2*j+1]

        # Apply magnet spring forces to fixed magnet vertical dofs
        # magnet1 = lower fixed magnet,
        # vdof = vertical dof
        F[magnet1_vdof[i], 1] = magnet1_force[i]
        # magnet2 = upper fixed magnet
        F[magnet2_vdof[i], 1] = magnet2_force[i]
        # the magnetic reaction forces applied to the fixed magnets
result in a torque
        # being applied to the structure, equal and opposite to that
applied to the resonator
        # torque_reaction_length precalculated elsewhere
        # hdof = horizontal dof
        F[magnet1_hdof[i], 1] = -mag_trq_res[i] /
(2*torque_reaction_length)
        F[magnet2_hdof[i], 1] = mag_trq_res[i] /
(2*torque_reaction_length)
```

A 1.8. Add input force to force vector

```
# Input force calculation

    # Calculate current impact input force magnitude and apply it at
vertical dof of input node
    # A similar process is carried out for a continuous input (e.g. sin
or random noise signal)
    # If the input in this simulation is an impact
    if beam_config['impact_input_force'] == True:
        impact_duration = study_properties['impact_duration']
        # calculate the time since the beginning of current impact
```

```
        impact_t_count = t_count % t_steps_per_impact
        impact_t = impact_t_count * delta_t
        # if the impact is still occurring, apply current impact force
        if impact_t < impact_duration:
            impact_input_force                  =                   0.5-
0.5*np.cos(2*np.pi*impact_t/impact_duration)
        # else, impact force is zero
        else:
            impact_input_force = 0
        # add the impact force to the force vector
        F[beam_input_vdof, 1] = impact_input_force
```

A 1.9. Time stepping for elastic structure

```
# Central difference time stepping scheme for elastic structure

    # Prior to calling this module, the following matrix preparation for
tansient analysis calculations
    # are carried out in separate module to avoid recalculating for
every time step
    #     Bdt               = B * delta_t/2
    #     MB_inv            = np.linalg.inv(M + Bdt)    # invert (M + Bdt)
    #     M_inv             = np.linalg.inv(M)          # invert M
    #     V                 = 2*M - delta_t**2 * K
    #     W                 = Bdt - M

    # d         = displacement vector
    # dt        = velocity vector
    # dtt       = acceleration vector
    d[:,2]        = MB_inv.dot(delta_t**2 * F[:,1] + V.dot(d[:,1]) +
W.dot(d[:,0]))
    dt[:,1]     = (d[:,2] - d[:,0])/(2*delta_t)
    dtt[:,1]    = M_inv.dot(F[:,1] - B.dot(dt[:,1]) - K.dot(d[:,1]))

    # At each time step, the current value is store at [:, 0] and the
previous value at [:, -1]
    # Update values for use as previous time step values during next
step
    d[:,-1]     = d[:,0]
    d[:,0]      = d[:,1]
    d[:,1]      = d[:,2]
    dt[:,0]     = dt[:,1]
    dtt[:,0]    = dtt[:,1]
    F[:,0]      = F[:,1]
```

A 1.10. Time stepping for resonators

```
# Central difference time stepping scheme for resonators

    # Calculate displacement, velocity and acceleration for each
resonator dof

    # Horizontal displacement
```

```
    # If the resonators are not free to rotate
    if beam_config['fixed_res_rotation'] == True:
        # Set resonator horizontal translation to zero
        um[:,2] = um[:,0]
    # If the resonators are free to rotate
    else:
        # Calculate horizontal displacement for each resonator cog
        um[:,2]  =  spring_MB_inv  *  (dt**2  *  net_cntct_frc_res[:,1]  +
spring_V * (um[:,1]) + spring_W * (um[:,0]))

    # Calculate horizontal velocity for each resonator cog
    dum[:,1] = (um[:,2] - um[:,0])/(2*dt)
    # Calculate horizontal acceleration for each resonator cog
    d2um[:,1] = 1/m * (net_cntct_frc_res[:,1] - spring_B * (dum[:,1]) -
spring_k * (um[:,1]))


    # Vertical displacement
    # Calculate vertical displacement for each resonator cog
    wm[:,2] = spring_MB_inv * (dt**2 * net_sprng_frc_res[:,1] + spring_V
* (wm[:,1]) + spring_W * (wm[:,0]))
    # Calculate vertical velocity for each resonator cog
    dwm[:,1] = (wm[:,2] - wm[:,0])/(2*dt)
    # Calculate vertical acceleration for each resonator cog
    d2wm[:,1] = 1/m * (net_sprng_frc_res[:,1] - spring_B * (dwm[:,1]) -
spring_k * (wm[:,1]))


    # Rotation
    # If the resonators are not free to rotate
    if beam_config['fixed_res_rotation'] == True:
        # Set resonator rotation to zero
        theta[:,2] = theta[:,0]
    else:
        # Calculate angle of rotation for each resonator
        theta[:,2] = 1/J * (dt**2 * net_trq_res[:,1] + 2*J * (theta[:,1])
- J * (theta[:,0]))
    # Calculate angular velocity for each resonator
    dtheta[:,1] = (theta[:,2] - theta[:,0])/(2*dt)
    # Calculate angular acceleration for each resonator cog
    d2theta[:,1] = 1/J * (net_trq_res[:,1])


    # Store previous values for use in next time step
    for i in range(3):
        um[:, i-1] = um[:, i]
    dum[:, 0]       = dum[:, 1]
    d2um[:, 0]      = d2um[:, 1]

    for i in range(3):
        wm[:, i-1] = wm[:, i]
    dwm[:, 0]       = dwm[:, 1]
    d2wm[:, 0]      = d2wm[:, 1]

    for i in range(3):
        theta[:, i-1] = theta[:, i]
    dtheta[:, 0]    = dtheta[:, 1]
    d2theta[:, 0]   = d2theta[:, 1]

    # Record net forces and torques
    net_cntct_frc_res[:, 0] = net_cntct_frc_res[:, 1]
```

```
net_sprng_frc_res[:, 0] = net_sprng_frc_res[:, 1]
net_trq_res[:, 0]       = net_trq_res[:, 1]
```

Appendix 2. Dynamics of free magnet resonator

This appendix presents preliminary calculations done as part of an exploration of a restitution-based impact model that accounts for a non-negligible impact duration relative to the time between impacts. This discussion is not a complete treatment of all that would be required to implement a model. It is limited to the calculation of angular acceleration of the resonator relative to the linear acceleration imparted during an impact.

Chapter 4, Section 4.2.3 explained that restitution-based models assume that the impact duration is negligible relative to the time between impacts. In the system being investigated, that was found not to be the case. Under the instantaneous impact assumption used in standard restitution methods, the post-impact position of each body is the same as the pre-impact position. However, with a non-instantaneous impact assumption, the post-impact position of each body must be calculated.

Figure A 2.1 shows a schematic of the interaction between a resonator and strut during an impact event. In the diagram, $\boldsymbol{r_c}$ is the vector from the resonator CG to the point of contact with the strut, ϕ is the angle of $\boldsymbol{r_c}$ from vertical and $\boldsymbol{\theta_c}$ is the angle of the resonator's rotation from vertical.

Firstly, recall from Chapter 3, Section 3.2 that the resonator magnet is acted upon by a magnetically induced torque which can be estimated as:

$$|\boldsymbol{\tau}| = |\boldsymbol{m} \times \boldsymbol{B}| = |\boldsymbol{m}||\boldsymbol{B}| \sin\theta \qquad \text{(A2.1)}$$

where τ is the torque acting on the magnet (approximated as a dimensionless dipole), m is the strength of the magnetic dipole and B is the strength of the magnetic field of the fixed magnets and θ is the angle of rotation of the resonator from orthogonal (i.e., the angle between the directions of the fields).

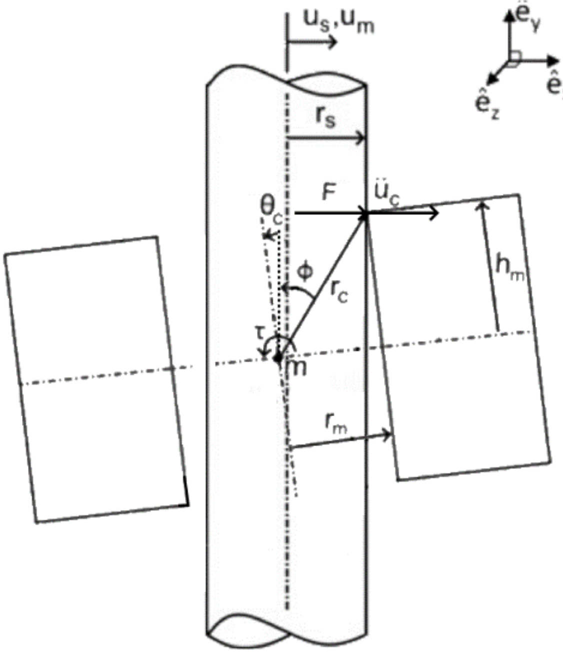

Figure A 2.1 Interaction between strut and magnetic resonator during an impact interaction

During an impact event, the resonator is also acted upon by a force ($\boldsymbol{F}$) from the strut at a single location (referred to here as the impact point). The angular acceleration imparted to the resonator over the course of an impact event can, therefore, be expressed as the sum of the moments acting on it:

$$\sum M = \ddot{\boldsymbol{\theta}} I_{c.o.g.} + \boldsymbol{r}_c \times \boldsymbol{F} + \boldsymbol{\tau} \tag{A2.2}$$

Where the $\ddot{\boldsymbol{\theta}} I_{c.o.g.}$ term is equal to the force due to rotational inertia. This can be rewritten in terms of unit vectors in the x, y and z coordinate directions, $\hat{\boldsymbol{e}}_x, \hat{\boldsymbol{e}}_y$ and $\hat{\boldsymbol{e}}_z$ as:

$$\sum M = \ddot{\theta} I_{c.o.g.} \hat{\boldsymbol{e}}_z + r_c\big(\cos(\phi)\,\hat{\boldsymbol{e}}_y + \sin(\phi)\,\hat{\boldsymbol{e}}_x\big) \times m\big[(\ddot{u}_c - \ddot{\theta} r_c \cos(\phi))\hat{\boldsymbol{e}}_x + (\ddot{\theta} r_c \sin(\phi))\,\hat{\boldsymbol{e}}_y\big] + \tau \hat{\boldsymbol{e}}_z \tag{A2.3}$$

Which simplifies as:

$$\sum M = \left[(\ddot{u}_c m r_c \cos(\phi) - \ddot{\theta}\left(m r_c^2 + I_{c.o.g.}\right) + \tau\right]\hat{\boldsymbol{e}}_z \qquad \text{(A2.4)}$$

where $m r_c^2 + I_{c.o.g.} = I_c$ is the moment of inertia about the contact point.

Therefore:

$$\ddot{\theta} = (\ddot{u}_c m r_c \cos(\phi) + \tau)/I_c \qquad \text{(A2.5)}$$

Appendix 3. Raw measurement data for magnet force-displacement curve

The table below contains the raw data from the magnet force measurement process described in Section 4.2.7. The digital scale and calliper were initially zeroed, and the initial distance between the lower surface of the resonator and the upper surface of the fixed magnet was measured by aligning the camera lens with the underside of the resonator and photographing it beside a ruler, as shown in Figure A 3.2.

Table A 3.1 Raw measurement data and derived gap size/force pairs for the force between a single fixed magnet and a resonator as described in Section 4.2.7.

Raw height measurement (mm)	Raw scale measurement (g)	Gap between magnet surfaces (mm)	Force (N)
0	0	32.5	0
1.92	5	30.58	0.049035
2.86	6	29.64	0.058842
4.05	9	28.45	0.088263
5.4	11	27.1	0.107877
6.8	17	25.7	0.166719
7.94	20	24.56	0.19614
9.3	28	23.2	0.274596
10.46	34	22.04	0.333438
11.63	43	20.87	0.421701
12.52	48	19.98	0.470736
13.83	63	18.67	0.617841
14.79	75	17.71	0.735525
16.01	95	16.49	0.931665
17.27	120	15.23	1.17684
19.24	168	13.26	1.647576
21.15	240	11.35	2.35368
21.98	279	10.52	2.736153
22.74	326	9.76	3.197082
23.7	391	8.8	3.834537
25.04	521	7.46	5.109447
26.47	722	6.03	7.080654
27.78	1009	4.72	9.895263

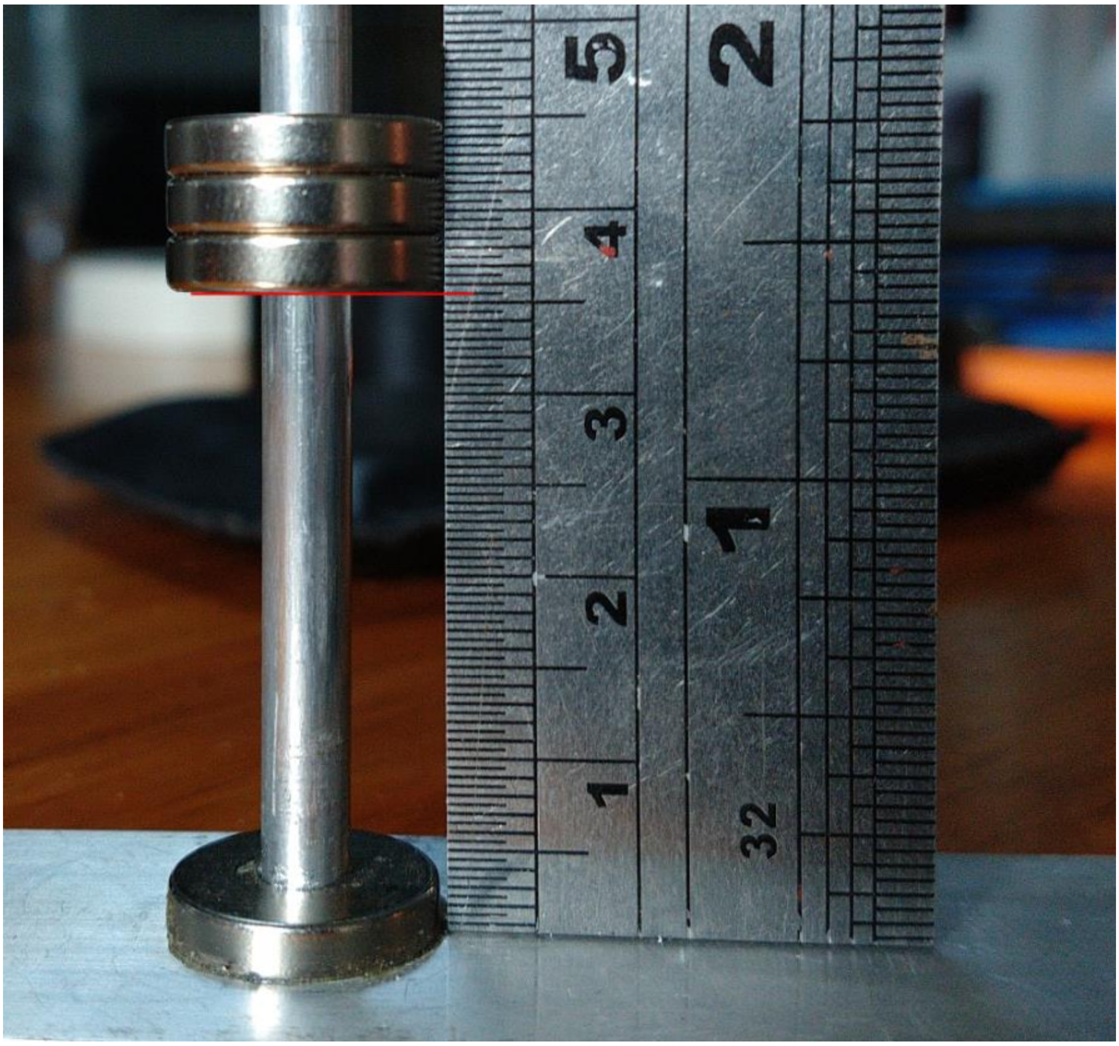

Figure A 3.2 Measurement of initial separation between resonator lower surface and fixed magnet upper surface